

BULGARIAN CHEMICAL COMMUNICATIONS

2022

Volume 54 / Number 4

*Journal of the Chemical Institutes
of the Bulgarian Academy of Sciences
and of the Union of Chemists in Bulgaria*

Polyphenol composition of wine from the variety Cabernet Sauvignon

A. Serafimovska, B. Korunoska*, G. Milanov, M. Taseska-Gjorgjijevski, D. Nedelkovski

University "Ss. Cyril and Methodius" in Skopje, Institute of Agriculture, Republic of Macedonia

Received: December 2, 2021; Revised November 14, 2022

Polyphenols and their derivatives are complex compounds that are responsible for the color and quality of red wines. The goal of the research was to determine the polyphenolic composition and its influence on the color and quality of the Cabernet Sauvignon variety. Wines obtained from Skopje, Ovce Pole and Gevgelija-Valandovo regions were investigated. In young wines, chemical analysis of total polyphenols, total anthocyanins, tint and color intensity was performed. The analyses were carried out by using spectrophotometric methods and standard chemical methods. With a higher content of total polyphenols (3385 mg/L EGA) and anthocyanins (978 mg/L), the wine from Skopje wine region was distinguished. The richest chemical composition has the wine from the Ovce Pole wine region with the highest content of alcohol (14.58 vol.%), dry extract (30.8 g/L) and total acids (5.8 g/L). The polyphenolic composition of the wines depends on a number of factors: the variety-clone, the substrate, the agro-technical and ampelotechnical measures, the yield, the degree of maturity, the health condition, the harvesting and transport and the terroir.

Keywords: vineyards, Cabernet Sauvignon, wine, polyphenols, anthocyanins.

INTRODUCTION

Polyphenols and their derivatives are a large complex of compounds that are responsible for the characteristics, color and quality of the wines, especially the red wines. They are a heterogeneous family composed of two main groups: flavonoids and non-flavonoids. Flavonoids in grapes and wine are mainly found as: anthocyanins, flavonols, flavan-3 ols (tannins or proanthocyanidins) [1, 2]. Non-flavonoids include phenolic acids and stilbenes. Polyphenols significantly affect the sensory characteristics of both, the grapes and the wine, since they are responsible for some organoleptic properties such as: aroma, color, bitterness and astringency. Thus, the anthocyanins are responsible for the color of red wines, while proanthocyanidins, which are still called condensed tannins, are responsible for the bitterness and astringency of the wines. The polyphenolic structure of the wines depends on a number of factors and can be divided into: unchangeable (constant) and variables. Invariable factors are: variety-clone, basis, soil and location. The group of variable factors includes: climatic conditions, agro-technical and ampelotechnical measures, yield, level of maturity, health condition, manner of harvesting and transport. Terroir has a major influence on the quality of grapes and wine [3, 4]. Defining the terroir conditions includes: soil, subsoil, microclimate, orography, exposure, level and composition of subsoil waters. The listed elements of the terroir give the specificity of the

wines originating from the existing conditions. The soil types influence the choice of the substrate, the variety and the quality of the grapes and the wine. Climate conditions (temperature, precipitation and insolation) during the year of production have the biggest impact on the quality of the grapes. The Skopje, Ovce Pole and Gevgelija-Valandovo wine areas, according to climatic characteristics, are in the continental-sub-mediterranean climate. The Skopje wine region is a typical area where the influence of the sub-mediterranean and eastern continental climate is combined [5].

Both the distance from the Aegean Sea and the proximity to the higher mountains contribute to the climate in this area, to be less homogeneous with pronounced variations of certain climatic elements. Ovce Pole and Gevgelija-Valandovo wine areas are characterized by a warmer climate and more sub-mediterranean influence. Climatic conditions have an impact on the variety and quality of the grapes (raw material) for wine production. Years of production in developed wine-growing countries on the basis of climatic conditions and quality of harvesting of the wines are declared as: good, very good and excellent. The warm climate conditions with an average annual air temperature of 11.5 °C-12.5°C, with vegetation temperature amount of 3800°C - 4000°C and precipitation up to 600 mm, are generally acceptable for the production of wine varieties such as Cabernet Sauvignon, Burgundy Black, Merlot and others. They provide a raw material for the production of red dry and intensively colored wines.

* To whom all correspondence should be sent:
E-mail: markovskabiljana@yahoo.com

MATERIAL AND METHODS

The tests were carried out with the variety Cabernet Sauvignon grown in three vineyards: Skopje, Ovce Pole and Gevgelija-Valandovo. The grape variety Cabernet Sauvignon was simultaneously taken up in full technological maturity from the three vineyards. Its processing was carried out in the experimental winery at the Agricultural Institute-Skopje. The grape pulp was treated with sulfides (with 50 mg/L). The maceration lasted 7 days and the fermentation was carried out at 25 ± 2 °C for a duration of 10 days. For more efficient extraction of the phenol components in the grape pulp, 3ml/HI enzyme and 25g/HI wine yeast were added. After fermentation, the wine was separated from the sediment and correction of SO₂ was made. So, the free SO₂ is not less than 25 mg/L and the total SO₂ is not higher than 100 mg/L. After that the wine was packed in bottles. Packaged wines were kept at 15 ± 2 °C temperature with adequate care. In the obtained young wines alcohol, total extract, sugar, total acids, volatile acids, free and total SO₂ and pH were measured at an accredited oenological laboratory of the Agricultural Institute-Skopje, according to the adopted methods of OIV. [5, 7, 11] Analysis of total polyphenols was performed according to the method of Folin-Ciocalteu, following the procedure below:

The wine sample was diluted 1/25. Then 5 mL of distilled water and 1 ml of the diluted wine were put in a 10 mL volumetric flask. 0.5 mL of Folin

Ciocalteu's reagent and 1.5 mL of Na₂CO₃ (20% solution) were added to the solution and after 3 min the volumetric flask was filled up to the mark with distilled water. Then the solution was left in a water bath for 16 min at 50°C. The colored samples were analyzed spectrophotometrically, at a wavelength of 765 nm. The obtained results are expressed in mg/L EGA (Equivalents galic acid) [6, 7]. For determination of anthocyanins, tint and intensity of the wine, it was necessary to centrifuge it, with 5000 revolutions per minute, with duration of 30 min. Centrifuged wine was diluted 1/100 with acidified ethanol (ethanol + concentrated HCl) [11, 12]. The diluted samples were analyzed spectrophotometrically, at a wavelength of 420, 520 and 550 nm. The values were obtained using the formulas for anthocyanins, nuance and intensity. Sensory assessment of guilt was performed by a five-member tasting committee.

RESULTS AND DISCUSSION

The chemical composition of the grape must is represented by: sugar content, total acidity content and pH. The lowest sugar content was registered in the sample of the Skopje wine area (215.0 g/L) and the highest value was obtained in the sample from the Ovce Pole region (245.0 g/L) [7, 10]. The Ovce Pole wine district was characterized by the highest total acid content (7.0 g/L). With the lowest content of total acid were the samples from Gevgelija-Valandovo wine region (5.7 g/L). The obtained results of the chemical composition of the must are shown in Table 1.

Table 1. Chemical composition of must

Parameter	Skopje region	Ovce Pole region	Gevgelija-Valandovo region
Sugar (g/L)	215.0	245.0	220.0
Total acids (g/L)	6.7	7.0	5.7
pH	3.43	3.35	3.61

Table 2. Chemical composition of wine

Parameter	Skopje region	Ovce Pole region	Gevgelija-Valandovo region
Alcohol (vol%)	12.68	14.58	13.00
Total extract (g/L)	29.70	30.8	28.9
Sugar (g/L)	1.0	1.0	1.0
Total acids (g/L)	5.7	5.8	4.9
Volatile acids (g/L)	0.56	0.34	0.42
Free SO ₂ (mg/L)	26.88	30.00	25.40
Total SO ₂ (mg/L)	70.40	64.00	52.04
pH	3.19	3.30	3.45

The following parameters were examined for the obtained wines from all three vintages: alcohol, total extract, sugar, total acids, volatile acids, free and total SO₂, pH, total phenols, anthocyanins, tint and intensity (Table 2). The highest content of alcohol (14.58 %) was obtained for the wine sample from Ovce Pole region. The content of total acids varied from 4.9 to 5.7 g/L which is within the permissible limit for quality red wine. The obtained results for volatile acids from 0.34 to 0.56 g/L indicated that they are microbiologically healthy wines [8, 9]. According to the content of the total extract (28.9 to 30.8 g/L) the wines are tasty and with high quality. The obtained values for total phenols, anthocyanins, tints and intensities in the young wine are shown in Table 3. The content of total phenols is variable. The result obtained for the wine sample from Skopje region is the highest (3385.00 mg/L EGA) and the lowest value (2342.00 mg/L EGA) is obtained for the sample from Gevgelija-Valandovo vineyard. The results for anthocyanins, from 422.77 to 978.84 mg/L EGA, for the samples from Gevgelija-Valandovo and Skopje, respectively, are shown in Table 3. The tint value (0.3265-0.3640) is within the permissible limits for young red wines. Its increase depends on storage and ripening period of the wine. The intensity (1.0155-1.3265) is within the allowed limits for young red wines, it has a variable character, decreases during maturing and aging of the wine.

Young wines from Cabernet Sauvignon varieties are of intense red color, with an odor that resembles to currant, blackberry, green pepper and other less pronounced spicy aromas. As a result of the higher content of tannins in the grapes, the young wine of taste is slightly coarse (mandatory longer maturation). Fully formed and ripened wine from the Cabernet Sauvignon variety is distinctive with a specific taste, intense color, light, harmonious.

Table 3. Phenolic compounds in wine

Parameter	Skopje region	Ovce Pole region	Gevgelija-Valandovo region
Total phenols mg/L (EGA)	3385.00	3020.00	2342.00
Anthocyanins mg/L (EGA)	978.84	732.42	422.77
Tint	0.3640	0.3265	0.3397
Intensity	1.2570	1.3265	1.0155

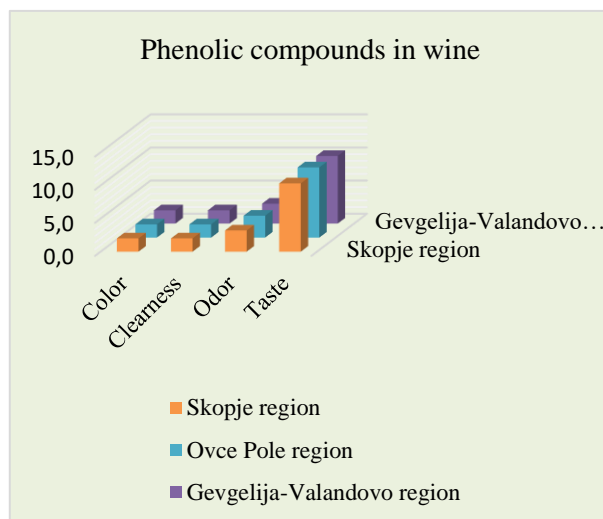


Chart 1.

Table 4. Sensory evaluation of the wine

Parameter	Skopje region	Ovce Pole region	Gevgelija-Valandovo region
Color	2.0	2.0	2.0
Cleanness	2.0	2.0	2.0
Odor	3.2	3.3	3.0
Taste	10.3	10.6	10.2
Total	17.5	17.9	17.2

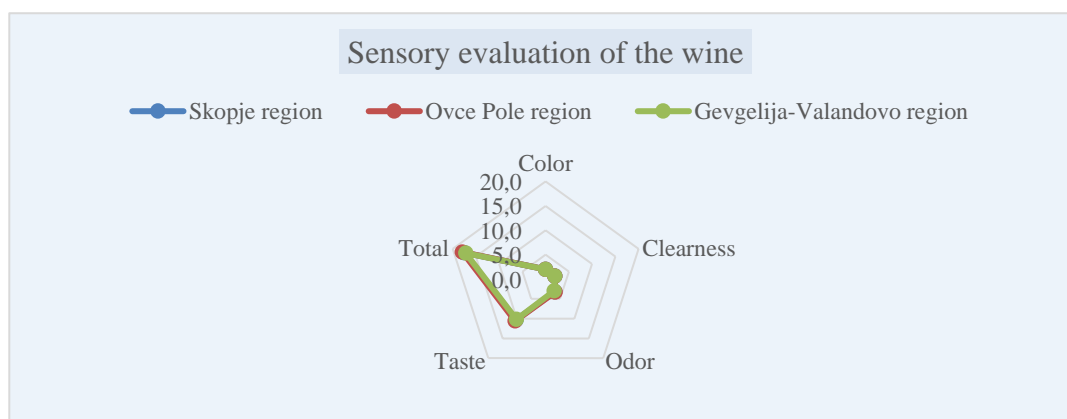


Chart 2.

In assessing the guilt, 4 parameters (color, clearness, odor and taste) were taken, which form the total tasting assessment. The maximum number of points is 20. The best quality and the highest sensory score (17.9) was evaluated for the wine from Ovce pole region. The lowest points had the wine from Gevgelija-Valandovo region (17.2 points). The results of the sensory evaluation of the guilt are presented in Table 4.

CONCLUSIONS

On the basis of the obtained results and performed tests on the Cabernet Sauvignon variety, the following conclusions can be made:

- Climatic and soil conditions in the Skopje, Ovce Pole and Gevgelija-Valandovo vineyards are very favorable for successful breeding of Cabernet Sauvignon. It provides a raw material for the production of quality and premium wines. It is recommended for growing in all the wineries of the Republic of Macedonia.

- The sugar content (215.0 - 245.0 g/L) and total acids (5.5-7.0 g/L) in the must are within the biological properties of the variety.

- The wine is characteristic for the variety Cabernet Sauvignon, it has a rich chemical composition: alcohol (12.68- 14.58%), total extract (28.9 to 30.8 g/L), total acids (4.9-5.8 g/L), anthocyanins 422.77-978.84 mg/L) and total phenols (2342.0-3385.0 mg/L EGA).

The best quality and highest sensory evaluation was established for the wine from Ovce Pole Vineyard.

*

REFERENCES

1. V. Artem, A.O. Antoce, I. Namolosanu, A. Ranca, A. Petrescu, *Scientific Papers. Series B, Horticulture*, **LIX**, 117 (2015).
2. A. Bertelli, M. Migliori, A. A. E. Bertelli, N. Orglia, C. Filippi, V. Panaichi, M. Falachi, L. Giovannini, *Drugs Under Experimental and Clinical Research Journal*, **28**, 11 (2002).
3. B. Korunoska, Ampelographic identification, study and collection of autochthonous varieties of vines in the Republic of Macedonia, Doctoral dissertation, Skopje, Macedonia, 2007.
4. Z. Božinović, Ampelografia, Agrinet DOO, Skopje, 2010.
5. B. A. O. Jiang, Z. W. E. N. Zhang, X. Z. Zhang, *Journal of the Chemical Society of Pakistan*, **33**(6), 900 (2011).
6. B. T. Mandžukov, XI Counseling wine growing and wine making, Prishtina, Serbia, 25-27. XI, 1996.
7. G. Milanov, M. Petkov, B. Vojnoski, V. K. Gelebeseva, Macedonian vine growing and wine making symposium with international participation, Skopje, September 26-28, 2001.
8. N. Stoyanov, S. Kemilev, Chr. Spasov, P. Mitev, First Enologic Conference with international participation "Enology of the Future", Plovdiv, September 26-28, 2004.
9. E. Obrique-Slier, A. Pena-Neira, R. Lopes-Solis, F. Zamora-Marin, J. M. Ricardo-da Silva, O. Laureano, *J. Agr. Food Chem.*, **58**, 3591 (2010).
10. R. B. Boulton, V. L. Singleton, L. F. Bisson, R. E. Kunkee, Macedonian language edn., Ars Lamina DOO, Macedonia, Copyright 2012, 1996.
11. N. Ružić, Lj. Jazić, G. Adžić, XI Counseling wine growing and wine making, Prishtina, Serbia, 25-27.XI. 1996.
12. B. W. Zoecklein, K. C. Fugelsang, B. H. Gump, F. S. Nury, Wine Analysis and Production, Macedonian language edn., Ad Verbum, Macedonia, Copyright 2009, 1995.

Reaction stoichiometry and mechanism of tetravalent cerium liquid-liquid extraction in the Ce(IV)-H₂SO₄-Cyanex 302-kerosene system

S. A. Milani, F. Zahakifar*, M. Faryadi

Nuclear Fuel Research School, Nuclear Science and Technology Research Institute, AEOL,
P.O.Box: 14155-1339, Tehran, Iran

Received: July 19, 2021; Revised: May 18, 2022

The single-stage extraction of cerium(IV) from sulfuric acid solutions with Cyanex 302 was scrutinized. The quantitative extraction of 0.002 mol L⁻¹ Ce(IV) at pH_(eq) ~ 4.0 was achieved by 0.1 mol L⁻¹ Cyanex 302 diluted in kerosene. The stoichiometry of the extracted species and the mechanism of extraction were elucidated on the basis of conventional slope analysis method. The distribution data were utilized to cover the determination of the conditions of feed solution pH, extractant concentration, organic-to-aqueous volume ratios, and reaction temperature for maximum extraction of cerium(IV). The temperature variation studies indicate that the overall extraction reaction is an exothermic process, which is confirmed from the negative value of ΔH. The positive value of ΔG suggests that the extraction process is non-spontaneous and the positive value of ΔS indicates that extraction of Ce(IV) is more efficient at high temperatures.

Keywords: Cerium(IV); Liquid-liquid extraction; Cyanex 302; Mechanism; Stoichiometry.

INTRODUCTION

Cerium compounds are widely used in magnets, polishing powders, phosphors, fluorescent powders, catalysts, and colorants [1-4]. This element is well found in minerals of monazite and bastnaesite groups. Generally, the easy oxidation of Ce(III) into Ce(IV) is used to separate Ce from other rare earth elements (REEs) [5]. Compared with REEs(III), Ce(IV) is more easily extracted [6, 7]. Liquid-liquid extraction is one of the common metal separation techniques from aqueous solutions [8-14]. This technique was utilized for the selective extraction of cerium from acidic leach liquors [8, 15-19]. The sulfuric acid leach liquors are among the cases from which Ce(IV) extraction is considered. 2-ethylhexyl phosphonic acid 2-ethylhexyl mono ester (EHEHPA, also known as PC88A, P-507 and Ionquest 801), di(2-ethylhexyl)phosphoric acid (D2EHPA or HDEHP also known as P204), Cyanex 923 as extractants for the Ce(IV) extraction have been scrutinized [16, 17, 20-25]. Cyanex 923 is considered as an effective extractant for Ce(IV). Wuping *et al.* [16, 24] investigated the extraction of Ce(IV) and F from simulated sulfuric acid liquor of bastnaesite with Cyanex 923. The latter can extract not only Ce(IV) as Ce(HSO₄)₂(SO₄). 2(Cyanex 923) but also F as HF(Cyanex 923). The extraction mechanism of Ce(IV) together with F can be related to the formation of Ce(HF)(HSO₄)₂(SO₄). 2(Cyanex 923).

However, the common organophosphorus esters, including di(1-methyl-heptyl) methyl phosphonate (P350), TBP, TOPO, Cyanex 925, and Cyanex 923 have their own downsides for the extraction of

Ce(IV). For instance, P350 cannot be utilized to extract Ce(IV) due to the difficulty of removing potential reducing impurities. For Cyanex 925 also the problem of reduction of Ce(IV) exists in sulfate medium [26]. TBP as an extractant for Ce(IV), requires high TBP concentrations and high acidities. Its ability to extract Ce(IV) is also low compared to other extractants. Cyanex 921 (TOPO) also has a high potential for the extraction of Ce(IV), but its solubility in aliphatic diluents is limited. A further disadvantage of TOPO is the slow kinetics of extraction. In the case of Cyanex 923, the impurities in Cyanex 923 reduce tetravalent cerium to the non-extractable trivalent state, and at high acidity, a third phase causing the decrease in extraction would appear. Cyanex 923 is more expensive than di(2-ethylhexyl) 2-ethylhexyl phosphonate (DEHEHP) and less utilized to Ce(IV) extraction [6, 23, 27]. D2EHPA requires higher acidity level in the stripping process which could affect the operational cost.

Despite the high extraction efficiency of D2EHPA for the REEs, the stripping difficulties in the loaded organic phase have limited its uses, especially for extraction of heavy REEs. Recently, particular attention has been paid to EHEHPA as an alternative extractant to D2EHPA for the separation of rare earth elements due to the high separation factors between any two adjacent rare earths [28]. In addition, REE-loaded extractants can be stripped at lower acidities in EHEHPA systems compared to D2EHPA systems [29-31], but the kinetics of

* To whom all correspondence should be sent:
E-mail: fzahakifar@aeoi.org.ir

extraction is slower and extraction efficiency is lower. Therefore, the development of new extraction systems for Ce(IV), especially in H₂SO₄ media, is a topic of great importance. In the field of solvent extraction, a recent development is the use of organophosphinic acid derivatives and their sulfur analogues (Cyanex reagents). Cyanex 302 and Cyanex 301 are mono- and disulfide analogues of Cyanex 272. The sulfur substitution decreases the pK_a values (6.4, 5.6 and 2.6 for Cyanex 272 [32], Cyanex 302 [33] and Cyanex 301 [34], respectively) allowing working at lower pH [35]. Cyanex reagents differ from other commercial organophosphorus reagents (e.g. D2EHPA, DDDPA, TBP, EHEHPA, etc.) in that the former reagents contain P-C bonding, whilst the latter contain P-O-C bonding. The presence of P-C bonding in Cyanex reagents makes them less susceptible to hydrolysis and less soluble in water [36]. Among organophosphorus extractants, dithio-substituted dialkylphosphinic acid, Cyanex 302, not yet used for cerium extraction, has received increasing regard due to its capability in the recovery of metal ions and for their separation from aqueous solutions [37-43]. Also there is no report on the extraction equilibrium and stoichiometry of Ce(IV) in the Ce(IV)-H₂SO₄-Cyanex 302-kerosene system.

The present study aims to optimize the extraction reaction of cerium(IV) in the Ce(IV)-H₂SO₄-Cyanex 302-kerosene system. The stoichiometry of the extracted cerium(IV) complex and a plausible extraction mechanism were proposed by using slope analysis and graphical methods. The influence of aqueous pH, extractant concentration, and temperature on the extraction of Ce(IV) was studied. The extraction thermodynamics by Cyanex 302 from sulfuric acid solution was obtained under the experimental conditions and thermodynamic functions ΔH, ΔG and ΔS of the investigated system were determined.

EXPERIMENTAL

Reagents and apparatus

The stock solution of Ce(IV) was prepared by dissolving Ce(SO₄)₂·4H₂O in sulfuric acid (H₂SO₄) (Merck) and diluting with distilled water. An amount of 1 mol L⁻¹ sodium hydroxide (Merck) was used for pH adjustment. The solution was standardized against 0.05 M EDTA solution [44] utilizing Eriochrome Black T as indicator. The commercial extractant, Cyanex 302 (bis-(2,4,4-trimethylpentyl) mono-thio-phosphinic acid) was supplied by Cytec Canada Inc. The organic phase was prepared by dissolving the extractant in kerosene (Sigma-Aldrich).

The concentration of Ce(IV) in the aqueous phase was measured with an inductively coupled plasma atomic emission spectrometer (ICP-AES) (Varian, Liberty 150AX Turbo, Australia). The aqueous pH adjustment was done using a digital pH meter (Metrohm 691 instrument). Also, extraction tests were conducted in a temperature-controlled circulating water bath 000-7126 (Haake A80).

Extraction procedure

Solvent extraction experiments were conducted in stoppered glass tubes immersed in a thermostated water bath (25.0 ± 0.5 °C) using equal volumes (10 mL) of the aqueous solution (0.5 ≤ pH_(ini) ≤ 6) containing 0.002 mol L⁻¹ Ce(IV) and organic phase containing the desired concentrations of extractant, Cyanex 302. Preliminary experiments demonstrated that equilibrium was achieved within 20 min. After phase disengagement, the aqueous phase was separated using a separating funnel, and the metal concentrations were determined by ICP-AES as mentioned above. The concentrations of the metal ions in the organic phase were calculated from the mass balance between the organic and aqueous solutions. The distribution coefficient (ratio), D, was calculated as the concentration of metal ion present in the organic to the aqueous solution at equilibrium. All the experiments were conducted at ambient temperature. The percentage extraction (%E) is defined as follows:

$$\%E = \frac{D}{D + \left(\frac{v_{aq}}{v_{org}}\right)} \times 100 \quad (1)$$

Stripping procedure

The stripping procedure was similar to the extraction one, with the exception that the aqueous phase was a prepared aqueous stripping phase and the organic one consisted of the metal-loaded organic phase obtained in the extraction process. The fully loaded organic solution with the highest extracted metal concentration was chosen for the further stripping studies. Cerium(IV) in this solution was stripped by (0.1, 0.5 or 1.0) mol L⁻¹ mineral acid (H₂SO₄, HCl or HNO₃) solution at 25±0.5 °C and at O:A of 1. The shaking time was 1 h. After equilibration and phase separation, the amount of the metal ions in the aqueous phase was measured by ICP-AES. The percentage stripping (%S) was calculated as follows:

$$\%S = \left(\frac{[Ce(IV)]_{(aq,eq)}}{[Ce(IV)]_{(o,ini)}} \right) \times 100 \quad (2)$$

RESULTS AND DISCUSSION

Effect of aqueous feed pH

The pH dependence of the extraction of Ce(IV) with Cyanex 302 was determined in the initial pH range 2.25–4.5 with 0.08 mol L⁻¹ extractant as shown in Fig. 1. The percentage extraction of cerium(IV) is near to zero for solutions with pH lower than 2. This indicates that for highly acidic media, hydronium ions strongly compete with metal ions to be extracted by the Cyanex 302. Extraction of cerium (IV) was achieved at lower pH, suggesting that Cyanex 302 has more acidity, thus allows the extraction at a lower pH [45]. Similar results have been observed regarding the impact of pH_(eq) on the extraction of various metal ions such as Cu²⁺, Co²⁺, Ni²⁺, Zn²⁺, and Fe²⁺ with Cyanex 272 and 302 [46]. The extraction increased with pH to almost 88% at pH_(ini) 4.0, pH_(eq) const. = 3.72. Results suggest that the optimal pH value of the aqueous feed solution should be fixed at 4, in order to obtain efficient extraction.

Effect of extractant concentration

The effect of the extractant concentration on the extraction of cerium(IV) was investigated by varying its concentration, as depicted in Fig. 2. Percentage extraction increased by augmenting the concentration of the extractant, due to the higher presence of extractant molecules. It was observed that the quantitative extraction of cerium(IV) was obtained by using 0.1 mol L⁻¹ Cyanex 302. Increased ion extraction with increasing Cyanex 302 concentrations has been reported in various studies [47-49].

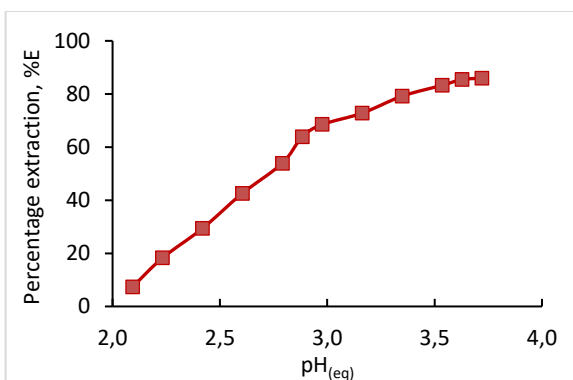


Fig. 1. Effect of pH_(eq) on the percentage extraction of Ce(IV) under conditions of 0.002 mol L⁻¹ Ce(IV), 0.08 mol L⁻¹ Cyanex 302 ($V_o/V_a = 1$), $T = (25.0 \pm 0.5)^\circ\text{C}$. Eq. time = 20 min.

Stoichiometry of the extraction reaction

R₂PSOH, the elemental constituent of Cyanex 302, is dimeric in non-polar diluents [46, 50]. In

aqueous solution, Ce(IV) virtually exists as Ce(OH)₂²⁺ and Ce(OH)₃⁺ [11, 51-53] which can form complexes with co-existing HSO₄⁻ and SO₄²⁻ (L⁻).

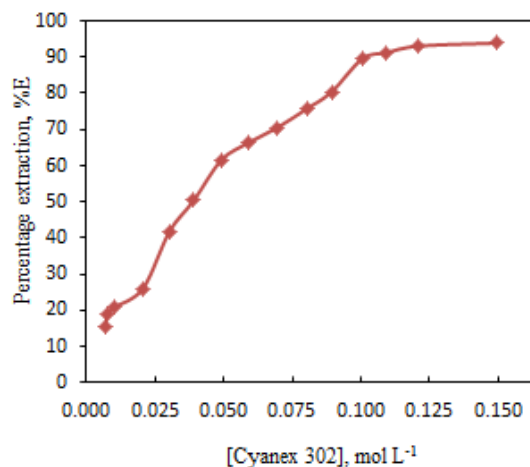
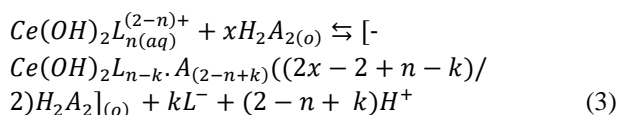


Fig. 2. Effect of extractant concentration on percentage extraction of Ce(IV) under conditions of 0.002 mol L⁻¹ Ce (IV); pH_(ini) = 4.0, pH_(eq) const. = 3.72; (V_o/V_a) = 1; $T = (25.0 \pm 0.5)^\circ\text{C}$, Eq. time = 20 min.

On considering the existence of $Ce(OH)_2L_n^{(2-n)+}$ in the aqueous phase, the equilibrium for its extraction by HA can be represented as (“x”, “2 - n + k” and “n/k” are experimental extractant, pH and co-existing ligand dependences, respectively):



On defining “D” as

$$D = \frac{[Ce(OH)_2L_{n-k} \cdot A_{(2-n+k)}((2x-2+n-k)/2)H_2A_2]_{(o,eq)}}{Ce(OH)_2L_n^{(2-n)+}} \quad (4)$$

the K_{ex} of equation (3) can be expressed as:

$$\log D = \log K_{ex} + mpH + x \log [H_2A_2]_{(o)} - k \log [L^-] \quad (5)$$

where “aq” and “o” represent the aqueous and organic phase, respectively; and $m = (2 - n + k)$.

The equation (5) illustrates the basic equation for a chelate-forming solvent extraction system by a dimeric acidic extractant. All concentrations and pH terms in equation (5) refer to the equilibrium values. Consequently, equation (5) represents that the value of log D should be independent of [Ce(IV)] at a set of constant equilibrium pH, [extractant] and [anion]. Corrected D-values (*i.e.* D_c) at a set of constant equilibrium pH and [extractant] can be calculated by mass-balance (equation (6)):

$$\log D_c = \log K_{ex} + mpH + x \log [H_2A_2]_{(o)} - k \log [L^-]$$

$$\log D_C = \log D + m(\text{pH}_{(ini)} - \text{pH}_{(eq)}) + x \log [H_2A_2]_{(o,ini)} - \log \{ [H_2A_2]_{(o,ini)} - x [Ce(IV)]_{(o,eq)} \} \quad (6)$$

At a constant $[H_2A_2]$, the plot of $\log D_C$ vs. $\text{pH}_{(eq)}$ should be a straight line with a slope of “m” (the number of protons liberated during chelation reaction). Fig. 3 represents the $\log D_C$ vs. $\text{pH}_{(eq)}$ plot at constant $[\text{extractant}]_{(o)}$ of 0.10 mol L^{-1} . Experimental points fall on a curve rather than on a straight line. Curve with limiting slope of almost 2 (1.8) is obtained at low pHs (l.pH) ($\text{pH}_{(eq)} < 2.3$), while the tangential slope is almost unity (1.26) at $\text{pH}_{(eq)} \sim 3.0$ and 0.40 at $\text{pH}_{(eq)}$ 3.7. It can be concluded from this result that the pH dependence is defined by the equilibrium pH range used: two hydrogen ions, 2 H^+ are liberated per Ce(IV) being complexed and extracted by Cyanex 302 when $\text{pH}_{(eq)}$ is kept below ~ 2.5 . With increasing $\text{pH}_{(eq)}$ value, the number of liberated H^+ ions decrease from 2 to 1 at $\text{pH}_{(eq)}$ of ~ 3.0 and 0.4 at $\text{pH}_{(eq)}$ of 3.7.

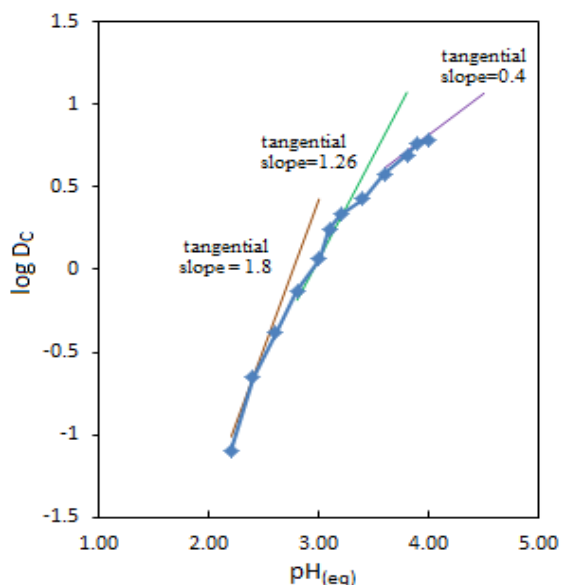


Fig. 3. Logarithmic plot of corrected distribution coefficient versus the equilibrium pH in batch extraction obtained under conditions of 0.002 mol L^{-1} Ce(IV), 0.1 mol L^{-1} Cyanex 302, $V_o/V_a = 1$ ($V_a = 10 \text{ mL}$), $T = (25 \pm 0.5) \text{ }^\circ\text{C}$. Eq. time = 20 min.

Based on equation (5), at a given constant pH, the $\log D$ vs. $\log [H_2A_2]_{(o)}$ plot should be a straight line with a slope indicating the mole ratio (x) of extractant/metal ion in the extracted species of Ce(IV) complex. The $\log D$ vs. $\log \{ [\text{Cyanex 302}]_{(o)} \}$ plot is depicted in Fig. 4. A straight line with a slope of ~ 2 (2.02) is obtained which shows the relationship between 2 moles of the extractant and 1 mole of metal in the extracted metal species.

The anion co-existing with the metal ion in the aqueous phase usually influences the extraction characteristics of the metal ion by an extractant.

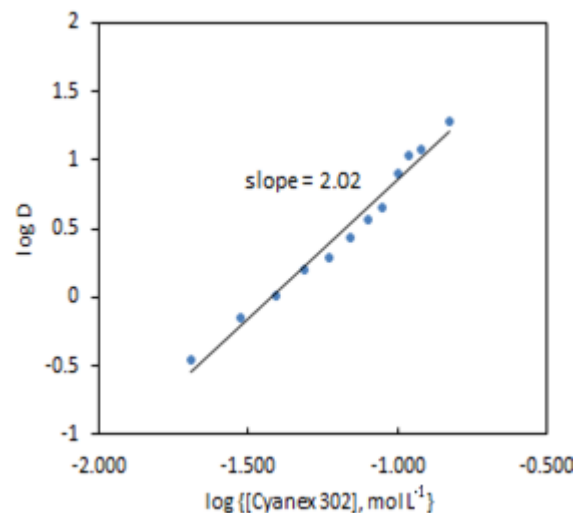


Fig. 4. Logarithmic plot of distribution coefficient vs the concentration of the extractant in batch extraction obtained under conditions of 0.002 mol L^{-1} Ce(IV), $V_o/V_a = 1$ ($V_a = 10 \text{ mL}$), $\text{pH}_{(eq)} 3.54$, $T = (25 \pm 0.5) \text{ }^\circ\text{C}$. Eq. time = 20 min.

This phenomenon is most often observed when extraction occurs by ion-pair formation and solvation mechanisms. In chelate-forming extraction systems, the co-existing anion may be involved in chelate formation. Also, the chelate formation may be impeded by the prior formation of metal-coexisting anion complex. Since the extraction is performed in sulfuric acid medium, the impact of $[\text{SO}_4^{2-}]/[\text{HSO}_4^-]$ on the extraction has to be studied. The 1st and 2nd ionization constants of H_2SO_4 are 10^3 [46] and 10^{-2} [50], respectively. These values suggest that SO_4^{2-} will be more available than $[\text{HSO}_4^-]$ in the working pH region. So, L in equation (3) represents SO_4^{2-} . The related plot is displayed in Fig. 5. Experimental points fall on a curved line rather than on a straight line. At low concentrations (l.c.r) of SO_4^{2-} , D is scarcely changed, whereas at high concentrations (h.c.r) of SO_4^{2-} , it significantly decreases with increasing $[\text{SO}_4^{2-}]$. Tangential slope at l.c.r of sulfate ion is almost 0 (-0.1), whilst the respective slope at h.c.r of sulfate ion is almost -1 (-0.9).

It is obvious from these studies that the value of “x” is 2 whatever the experimental parameters but the value of “k” is 0 at low $[\text{SO}_4^{2-}]$ and 1 at high $[\text{SO}_4^{2-}]$. The value of “m (= 2 - n + k)” is 2 at low pH (l.pH), 1 at middle pH (m.pH), and 0.4 at high pH (h.pH). At l.c.r of sulfate ion and at l.pH, $m = 2$ suggests that $n = 0$; but at intermediate pH, $m = 1$ involves that $n = 1$, and finally at h.pH, $m = 0.40$ implies that $n = 1.60$. On the other hand, at h.c.r of SO_4^{2-} and at l.pH, $m = 2$ implies $n = 1$; but at intermediate pH, $m = 1$ suggests $n = 2$ and at h.pH, $m = 0.40$ insinuates $n = 2.60$.

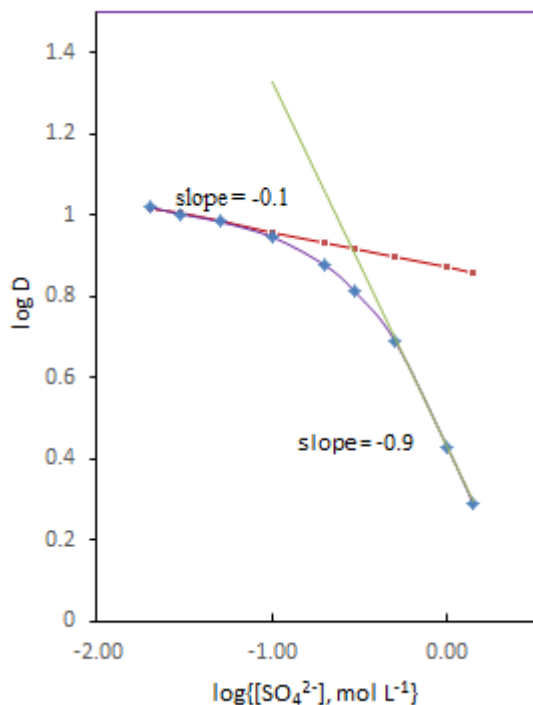


Fig. 5. Logarithmic plot of distribution coefficient versus the initial concentration of co-existing SO_4^{2-} on batch extraction obtained under conditions of 0.002 mol L^{-1} Ce(IV), 0.1 mol L^{-1} Cyanex 302, $V_o/V_a = 1$ ($V_a = 10 \text{ mL}$), $T = (25 \pm 0.5)^\circ\text{C}$. Eq. time = 20 min.

Extraction mechanism

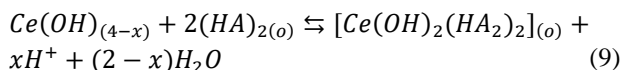
The afore-mentioned experimental results lead to the following expression relating the equilibrium constant with the distribution coefficient in the extraction of Ce(IV) in the Ce(IV)- H_2SO_4 -Cyanex 302-kerosene system:

$$K_{ex} = \frac{D[L]^{-k}[H^+]^x}{[(HA)_2]^2} \quad (7)$$

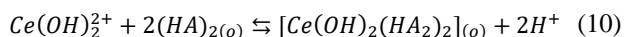
At l.c.r of SO_4^{2-} , $k = 0$, so that equation (7) becomes:

$$K_{ex} = \frac{D[H^+]^x}{[(HA)_2]^2} \quad (8)$$

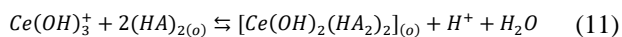
Equation (8) propounds the following general chemical reaction as the extraction equilibrium reaction:



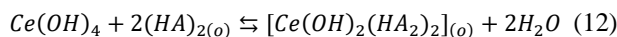
When $x = 2$, i.e. at $\text{pH} \leq 2.4$, equation (9) becomes:



and when $x = 1$, i.e. at $\text{pH} \approx 3.0$, equation (9) becomes:



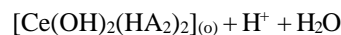
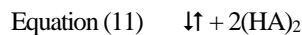
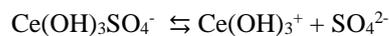
and when $x = 0$, i.e. at $\text{pH} \geq 3.9$, equation (9) becomes:



At h.c.r of SO_4^{2-} , equation (7) becomes:

$$K_{ex} = \frac{D[\text{SO}_4^{2-}][\text{H}^+]^x}{[(\text{HA})_2]^2} \quad (13)$$

Equation (13) implies the liberation of sulfate ion during the extraction reaction. But at a certain pH, the values of K_{ex} at l.c.r and h.c.r of sulfate are identical. It is inferred that at h.c.r of SO_4^{2-} , the general equation (9) also represents the extraction equilibrium reaction. But in this case, as the sulfate concentration increases, the free non-sulfated/bisulfated Ce(IV)-species concentration decreases during the extraction of the metal ion. This gradual depletion is probably compensated through dissociation of sulfated/bisulfated Ce(IV)-species. Moore and Anderson [54] made a spectrophotometric study of cerium perchlorate in perchloric acid sodium perchlorate-sodium sulfate solution. Up to 0.01 M sulfate, $\text{Ce}(\text{SO}_4)_2^{2+}$ and $\text{Ce}(\text{OH})(\text{SO}_4)^+$ ($\text{pH} 0.72-0.76$) were reported to predominate and evidence for higher complexes was obtained [54, 55]. It appears therefore that the equilibrium shift occurs between sulfated and non-sulfated species as suggested below:



The proposed structure of the oligomeric cerium complex with the R_2PSO^- ligand is shown in Fig. 6.

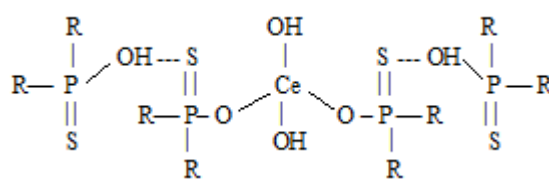


Fig. 6. Postulated structure of the oligomeric cerium complex with Cyanex 302.

Thermodynamic investigation of the extraction

Distribution coefficients were determined by shaking equal volumes of the aqueous feed solution and 0.1 mol L^{-1} Cyanex 302 solution in kerosene.

The experiments were performed at Cyanex 302 concentrations lower than the optimum concentration to better see the effect of temperature. Other parameters were as in Fig. 2. The Van't Hoff plots for the studied system are shown in Fig. 7. It is deemed that the extraction ratio increases with raising temperature but the straight line relationship does not hold over the entire temperature range.

Slopes of the lines in the high temperature region (h.t.r) and in the l.t.r are -1567.5 and -3928 , respectively. From the slope and intercept obtained from Fig. 7 and applying the Van't Hoff equations [56, 57], the thermodynamic parameters are calculated as:

$$\log D = -\frac{\Delta H}{2.303RT} + C \quad (14)$$

where R, T, and C are the universal gas constant, absolute temperature, and conditional constant, respectively. Activity coefficients for other components are considered to be constant under the experimental conditions [58].

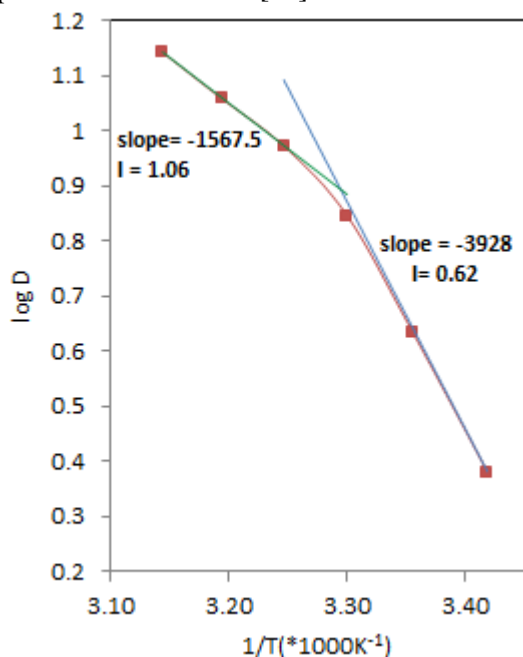


Fig. 7. Relationship between distribution coefficient (D) and reaction temperature under conditions of 0.002 mol L^{-1} Ce(IV), 0.08 mol L^{-1} Cyanex 302, $V_o/V_a = 1$ ($V_a = 10 \text{ mL}$), initial solution pH(eq) 3.54. Eq. time = 20 min.

The slopes equal $-\Delta H/2.303R$. On the basis of Eq. (14) and Fig. 7, the values of ΔH are calculated to be 30.00 at h.t.r and $75.21 \text{ kJ mol}^{-1}$ at l.t.r, indicating that the extraction reaction is endothermic. Therefore, the extraction efficiency increased by temperature raise. Also, the values of the change in the Gibbs free energy (ΔG) and the entropy (ΔS) were calculated from the following equations for extraction reaction at 298 K :

$$\Delta G = -2.303RT \log D \quad (15)$$

$$\Delta S = \frac{\Delta H - \Delta G}{T} \quad (16)$$

The values of ΔG and ΔS were calculated equal to $23.96 \text{ kJ mol}^{-1}$ and $20.26 \text{ J mol}^{-1} \text{ K}^{-1}$, and $71.76 \text{ kJ mol}^{-1}$ and $11.87 \text{ J mol}^{-1} \text{ K}^{-1}$, respectively. The positive ΔG specified that the extraction reaction by Cyanex 302 proceeded not spontaneously. The positive values of ΔS indicated that the extraction of Ce(IV) is more efficient at high temperatures.

In a similar research, the thermodynamic study of copper(II) extraction from sulfate, nitrate and chloride media using Cyanex 302 in kerosene has shown that the extraction reaction is endothermic and non-spontaneous [47].

Effect of diluent type

In order to ascertain the impact of diluent type on Ce(IV) distribution, %E-values were evaluated when 0.002 mol L^{-1} Ce(IV) was extracted separately from the same aqueous feed solution by 0.10 mol L^{-1} extractant in various diluents while keeping constant all other conditions ($\text{pH}_{\text{ini}} = 3.6$ and $[\text{SO}_4^{2-}] = 0.0002 \text{ mol L}^{-1}$) (Table 1). It was observed that the percent extraction increases in the following order with the variation of diluent used to prepare the organic solution: CHCl_3 ($D = 1.02$) < CCl_4 ($D = 4.73$) = cyclo- C_6H_{12} ($D = 4.73$) < kerosene ($D = 5.80$) < 1,2- $\text{C}_2\text{H}_4\text{Cl}_2$ ($D = 7.36$) = $\text{C}_6\text{H}_4-(\text{CH}_3)_2$ (xylene) ($D = 9.85$) < C_6H_6 ($D = 14.44$) = $\text{C}_6\text{H}_5-\text{CH}_3$ (toluene) ($D = 14.44$). The study allows concluding on the effect of diluent on the rate of extraction of cerium and on the best ones of the diluents for the cases studied. C_6H_6 and $\text{C}_6\text{H}_5-\text{CH}_3$ are very good diluents followed by $\text{C}_6\text{H}_4-(\text{CH}_3)_2$ for the extraction of Ce(IV) by Cyanex 302. Kerosene is a better diluent over CHCl_3 , CCl_4 and cyclo- C_6H_{12} .

Stripping of Ce(IV)-loaded organic phase

The maximum Ce(IV) loaded organic phase, after the extraction step, was submitted to a stripping step using various mineral acids such as H_2SO_4 , HNO_3 and HCl solutions at $25 \text{ }^\circ\text{C}$ and $V_o:V_a = 1$. The stripping results are presented in Table 2. It is deemed that stripping percentage is roughly acceptable in all three mineral acids used alone. In all cases, the percentage stripping increased by raising concentration of acid. Sulfuric acid (1 M) is sufficient to quantitatively strip off Ce(IV). HNO_3 and HCl can also be utilized in stripping if two-stage stripping is implemented.

Table 1. Effect of diluent type on extraction of Ce(IV). $[\text{Ce(IV)}]_{\text{(ini)}} = 0.002 \text{ mol L}^{-1}$, $\text{pH}_{\text{(ini)}} = 3.6$, $[\text{Cyanex 302}] = 0.1 \text{ mol L}^{-1}$, $[\text{SO}_4^{2-}] = 0.0002 \text{ mol L}^{-1}$, $T = (25 \pm 0.5) \text{ }^\circ\text{C}$. Eq. time = 1 h, $V_o/V_a = 1$, $V_a = 10 \text{ mL}$

Diluent	Ce(IV)] _{aq} eq, mol L ⁻¹	Ce(IV)] _o eq, mol L ⁻¹	%E	D
Carbon tetrachloride	0.00035	0.0017	82.54	4.73
Benzene	0.00013	0.0019	93.52	14.44
Toluene	0.00013	0.0019	93.52	14.44
Cyclohexane	0.00035	0.0017	82.54	4.73
1,2-Dichloroethane	0.00024	0.0018	88.03	7.36
Xylene	0.00018	0.0018	90.78	9.85
Chloroform	0.00099	0.0010	50.51	1.02
Kerosene	0.00029	0.0017	85.29	5.80

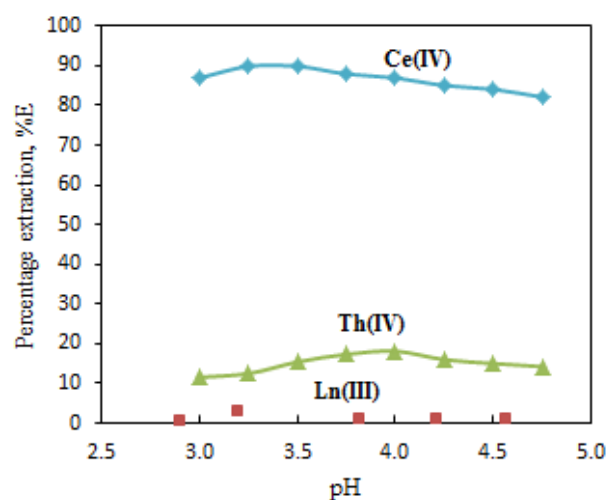
Table 2. Stripping of Ce(IV)-loaded organic phase using different mineral acid solutions. $[\text{Ce(IV)}]_{\text{o}} \approx 0.0018 \text{ mol L}^{-1}$, $[\text{Cyanex 301}] = 0.10 \text{ mol L}^{-1}$, Eq. time = 1 h, $T = (25 \pm 0.5) \text{ }^\circ\text{C}$, $V_o/V_a = 1$ ($V_a = 10 \text{ mL}$).

Stripping agent	Concentration, mol L	Percentage stripping, %S
	0.1	70.43
H ₂ SO ₄	0.5	94.50
	1.0	98.80
	0.1	85.12
HNO ₃	0.5	94.05
	1.0	98.50
	0.1	44.33
HCl	0.5	84.15
	1.0	92.59

Selectivity studies

The selective extraction of Ce(IV) considering the presence of many associated metal ions and impurities such as Th(IV), and REE(III) (REE = La³⁺, Ce³⁺, Nd³⁺, Gd³⁺ and Yb³⁺) using a solution containing 0.3 g L⁻¹ of the different metal ions in sulfuric acid solution (with $\text{pH}_{\text{(ini)}}$ range of approximately 3.0 – 4.5) with 0.1 M Cyanex 302 in kerosene at $V_o:V_a = 1$ and $(25 \pm 0.5) \text{ }^\circ\text{C}$ were investigated. The percent extraction data of the different metal ions shown in Fig. 8 indicate that a selective cerium separation can be done efficiently from H₂SO₄ solution in the pH range of 3-4 as rare earth ions (III) are almost not extracted under these experimental conditions. The

extraction of Th(IV) is low. Therefore, by selecting the appropriate acidity, cerium can be separated from REEs(III) and Th(IV).

**Fig. 8.** Selectivity of Cyanex 302 for Ce(IV), Th(IV), and RE(III) under conditions of aqueous feed solution: 0.3 g L⁻¹ of the different metal ions in H₂SO₄ solution ($\text{pH}_{\text{(ini)}}$ of approximately 3.0 to 4.5); organic phase: 0.1 M Cyanex 302 in kerosene; $V_o/V_a = 1$ ($V_a = 10 \text{ mL}$); $T = (25 \pm 0.5) \text{ }^\circ\text{C}$.

CONCLUSIONS

Cyanex 302 extracts Ce(IV) from sulfuric acid medium at pH above 3.0. The equilibration time is 20 min. The recovery of Ce(IV) can be regulated by controlling the extractant and pH of aqueous feed solutions. Cyanex 302 is a forward-looking extractant for the Ce(IV) extraction. At various concentration levels of the experimental parameters, extraction equilibrium reactions were proposed. It is seen that at all conditions, $[\text{Ce(OH)}_2(\text{HA}_2)_2]$ is the extractable species though reacting Ce(IV) species in the aqueous phase may vary with its concentration and pH levels. Aromatic diluents appear as better diluents over other categories; kerosene is a better

diluent than CHCl_3 , CCl_4 and cyclo- C_6H_{12} . The temperature-sensitive extraction process of this metal in the studied system is endothermic ($\Delta H < 0$). The positive value of ΔG reveals that the extraction reaction proceeds not spontaneously, and the positive value of ΔS indicates that extraction of Ce (IV) is more desirable at high temperatures.

REFERENCES

1. S. Kuang, Z. Zhang, Y. Li, G. Wu, H. Wei, W. Liao, *Hydrometallurgy*, **167**, 107 (2017).
2. Y. Chen, X. Wang, X. He, Q. An, Z. Zuo, *J. Amer. Chem. Soc.*, **143**, 4896 (2021).
3. M. Xu, V. Smolenski, Q. Liu, A. Novoselova, K. Jiang, J. Yu, J. Liu, R. Chen, H. Zhang, M. Zhang, *J. Chem. Therm.*, **152**, 106260 (2021).
4. Y. Shan, Y. Liu, Y. Li, W. Yang, *Sep. Pur. Tech.*, **250**, 117181 (2020).
5. J.-Y. Kim, U.-S. Kim, M.-S. Byeon, W.-K. Kang, K.-T. Hwang, W.-S. Cho, *J. Rare Earths*, **29**, 1075 (2011).
6. J. Zhao, S. Meng, D. Li, *Sol. Extr. Ion Exch.*, **22**, 813 (2004).
7. E. Allahkarami, B. Rezai, *J. Env. Chem. Eng.*, **9**, 104956 (2021).
8. S. Milani and F. Zahakifar, *Braz. J. Chem. Eng.*, **39**, 553 (2022).
9. E. M. Abu Elgoud, Z. Ismail, Y. El-Nadi, H. Aly, *Chem. Pap.*, **74**, 2461 (2020).
10. M. M. Khataei, S. B. H. Epi, R. Lood, P. Spégel, Y. Yamini, C. Turner, *J. Pharm. Bio. Anal.*, **209**, 114487 (2022).
11. C. Li, H. He, M. He, Y. Gao, M. Zhang, C. Jiao, *J. Rad. Nuc. Chem.*, **1** (2021).
12. K. Li, J. Chen, D. Zou, Y. Deng, D. Li, *Hydrometallurgy*, **190**, 105155 (2019).
13. S. Ilyas, H. Kim, R. R. Srivastava, *Rare Met. Tech.*, Springer, 2021, p. 303.
14. S. Alamdar Milani, M. Ashtianifar, F. Zahakifar, *J. Appl. Res. Chem. Pol. Eng.*, **5**, 87 (2021).
15. R. D. Abreu, C. A. Morais, *Min. Eng.*, **23**, 536 (2010).
16. W. Liao, G. Yu, D. Li, *Sol. Extr. Ion Exch.*, **19**, 243 (2001).
17. L. Wang, Y. Yu, X. Huang, Z. Long, D. Cui, *Chem. Eng. J.*, **215**, 162 (2013).
18. D. Xu, Z. Shah, Y. Cui, L. Jin, X. Peng, H. Zhang, G. Sun, *Hydrometallurgy*, **180**, 132 (2018).
19. R. Mu, J. Chen, D. Zou, K. Li, D. Li, *Sep. Pur. Tech.*, **209**, 351 (2019).
20. D. Li, Z. Wang, G. Zeng, Z. Xue, *J. Chin. Rare Earths Soc.*, **2**, 9 (1984).
21. L. Xinghua, X. HUANG, Z. Zhaowu, L. Zhiqi, L. Ying, *J. Rare Earths*, **27**, 119 (2009).
22. D. Li, Z. Wang, G. Zeng, Z. Xue, *J. Chin. Rare Earth Soc.*, **2**, 9 (1984).
23. L. Jun, W. Zhenggui, L. Deqian, M. Gengxiang, J. Zucheng, *Hydrometallurgy*, **50**, 77 (1998).
24. W. Liao, G. Yu, D. Li, *Acta Met. Sin.*, **14**, 21 (2001).
25. M. Ugajin, S. Ajuria, *IAEA-TEC DOC-337* (1985).
26. K. Soldenhoff, *Proc. Int. Sol. Ext. Conf.*, **1** (1996).
27. Z. Dan, C. Ji, L. Deqian, *J. Rare Earths*, **32**, 681, 2014.
28. D. Li, Y. Bai, X. Sun, S. Liu, 52nd Conf. of Met., (2013).
29. A. A. Abdeltawab, S. Nii, F. Kawaizumi, K. Takahashi, *Sep. Pur. Tech.*, **26**, 265 (2002).
30. C. Basualto, F. Valenzuela, L. Molina, J. Munoz, E. Fuentes, J. Sapag, *J. Chil. Chem. Soc.*, **58**, 1785 (2013).
31. N. Krishnamurthy, C. K. Gupta, *Extr. Met. Rare Earths*, CRC press, 2015.
32. J. Saji, M. Reddy, *Sep. Sci. Tech.*, **38**, 427 (2003).
33. J. Saji, K. S. John, M. Reddy, *Sol. Extr. Ion Exch.*, **18**, 877 (2000).
34. M. Ulewicz, W. Walkowiak, *Env. Pro. Eng.*, **31**, 73 (2005).
35. W. Rickelton, *JoM*, **44**, 52 (1992).
36. A. Saily, S. Tandon, *Fresenius' J. Anal. Chem.*, **360**, 266 (1998).
37. B. Gupta, Z. Begum, *Sep. Pur. Tech.*, **63**, 77 (2008).
38. T. Miaomiao, J. Qiong, L. Wuping, *J. Rare Earths*, **31**, 604 (2013).
39. S. Tong, X. Zhao, N. Song, Q. Jia, W. Zhou, W. Liao, *Hydrometallurgy*, **100**, 15 (2009).
40. B. K. Tait, *Hydrometallurgy*, **32**, 365 (1993).
41. N. El-Hefny, J. Daoud, *J. Rad. Nucl. Chem.*, **261**, 357 (2004).
42. R. K. Biswas, A. K. Karmakar, *Sep. Sci. Tech.*, **49**, 278 (2014).
43. Y. Zhu, J. Chen, R. Jiao, *Sol. Extr. Ion Exch.*, **14**, 61 (1996).
44. H. Khalifa, B. Barsoum, *Mic. J.*, **18**, 428 (1973).
45. T. H. Handley, *Talanta*, **12**, 893 (1965).
46. K. C. Sole, J. B. Hiskey, *Hydrometallurgy*, **30**, 345 (1992).
47. N. El-Hefny, J. Daoud, *Sol. Extr. Ion Exch.*, **25**, 831 (2007).
48. K. C. Sole, T. L. Ferguson, J. B. Hiskey, *Sol. Extr. Ion Exch.*, **12**, 1033 (1994).
49. A. Almela, M. Elizalde, *Hydrometallurgy*, **37**, 47 (1995).
50. E. Paatero, T. Lantto, P. Ernola, *Sol. Extr. Ion Exch.*, **8**, 371 (1990).
51. B. Bouchaud, J. Balmain, G. Bonnet, F. Pedraza, *J. Rare Earths*, **30**, 559 (2012).
52. R. Marsac, F. Réal, N. L. Banik, M. Pédrot, O. Pourret, V. Vallet, *Dalton Transactions*, **46**, 13553 (2017).
53. L. O. Tuazon, Iowa State University, 1959.
54. R. L. Moore, R. C. Anderson, *J. Amer. Chem. Soc.*, **67**, 167 (1945).
55. E.L. King, M.L. Pandow., *J. Am. Chem. Soc.*, **74**, 1966 (1952).
56. F. Islam, H. Rahman, M. Ali, *J. Inorg. Nucl. Chem.*, **41**, 217 (1979).
57. T. Wongsawa, W. Ampronpong, N. Traiwongsa, U. Pancharoen, W. Punyain, S. Phatanasri, *J. Tai, Inst. Chem. Eng.*, **122**, 40 (2021).
58. D. Mohapatra, K. Hong-In, C.-W. Nam, K.-H. Park, *Sep. Pur. Tech.*, **56**, 311 (2007).

Optimisation and validation of a method for determination of selenium in human plasma and blood by ETAAS and its clinical application

P. Sherovski*, N. Ristovska, J. Bogdanov, T. Stafilov

*Institute of Chemistry, Faculty of Natural Sciences and Mathematics,
Ss. Cyril and Methodius University, Arhimedova 5, 1000 Skopje, North Macedonia*

Received: January 17, 2022; Revised: August 27, 2022

Selenium is a part of the active center of glutathione peroxidase, thioredoxin reductase, and iodothyronine deiodinase which have antioxidant activity and play an important role in the metabolism of thyroid hormones. Therefore, blood selenium concentration is strongly correlated with immune function, thyroid disease, and tumorigenesis. In this work, a method for the determination of selenium in blood and plasma by electrothermal atomic absorption spectrometry (ETAAS) was optimized and validated. Samples were prepared by dilution in 0.2% detergent (Triton X-100, Tween 80, or SDS) in 0.1% HNO₃. The pyrolysis was performed at 1100°C for 30 s for plasma and 35 s for blood, while atomization at 2500°C for 3 s with a Pd matrix modifier. LOD and LOQ for plasma samples were 0.56-0.62 µg/L and 1.87-2.07 µg/L depending on the detergent used, while LOD and LOQ for blood samples were 0.64-0.72 µg/L and 2.12-2.41 µg/L, respectively. The validation results show a recovery of 98.25-102.65%. The precision of the method ranges from 1.55% to 2.63%. The method was applied for the determination of selenium in plasma and whole blood in healthy patients. The obtained selenium concentrations in plasma are in the range of 31.40–47.01 µg/L, while the concentrations in whole blood samples are higher by 23-25%.

Keywords: selenium; blood; plasma; electrothermal atomic absorption spectrometry

INTRODUCTION

Selenium in the form of selenocysteine is an essential component of the glutathione peroxidase enzymes (GPx) and thioredoxin reductase (TR). These enzymes protect tissues from oxidative damage by removing oxygen free radicals [1]. This micronutrient has been studied over the last two decades, and scientific reports have revealed its crucial role in biological processes, such as free radical catabolism, immune response, endocrine function and tumorigenesis [2].

Oxidative stress due to decreased glutathione peroxidase activity, as a result of low Se concentration or increased free radical damage has been proposed to be an important event in the pathogenesis of different diseases such as Alzheimer's disease, coronary heart disease, lung and prostate cancers [3]. Based on observational studies, several meta-analyses have summarized inverse associations between levels of selenium biomarkers and lung [4] and prostate [5] cancers. Also, there are several studies available in the literature which reported the associations between brain selenium levels and Alzheimer's disease [6]. A recent meta-analysis of 14 prospective studies found a modest but statistically significant inverse association between selenium levels and coronary heart disease [7].

On the other hand, being incorporated into iodothyronine deiodinases D1 and D2, selenium also plays an essential role in the metabolism of thyroid hormones [8]. Regarding thyroid pathology, selenium intake has been particularly associated with autoimmune disorders. The literature suggests that selenium supplementation of patients with autoimmune thyroiditis is associated with a reduction in antithyroperoxidase antibody levels, improved thyroid ultrasound features, and improved quality of life. Selenium supplementation in Graves' disease is associated with an improvement in quality of life and eye involvement, as well as a delayed progression of ocular disorders [9].

In plasma Se is incorporated in selenoprotein P which may serve as a transport protein for Se and facilitate whole body Se distribution [10]. Selenium levels in the body are dependent on the population's characteristics and its diet and geographical area [11]. Among all human tissues, the thyroid gland contains the largest concentrations of selenium. The main sources of selenium in the form of selenocysteine are mammalian meat, chicken, and fish. On the other hand, selenomethionine is found in vegetable sources such as pasta or rice, bread or cereals, garlic (*Allium sativum*), Indian mustard (*Brassica juncea*), canola (*Brassica napus*), and some mushrooms [12].

Understanding of selenium biochemistry and its importance resulted in rapid growth in the number

* To whom all correspondence should be sent:
E-mail: Sherovskip@pmf.ukim.mk

Consequently, there is a need for methods that are rapid, accurate, and require only a small amount of sample. Methods based on direct analysis by electrothermal atomic absorption spectrometry (ETAAS) [13], hydride generation atomic absorption spectroscopy (HG-AAS) [14], and inductively coupled plasma - mass spectrometry (ICP-MS) [15], are widely used. ETAAS is the most useful spectrometric method for mono-elemental analysis due to its high selectivity, low quantification limit, and acceptable costs [16]. Most of the matrix is destroyed during the ashing step and thus sample pre-treatment can be simplified (simple sample dilution), thereby minimizing contamination risk or analyte loss. Also, low injection volume (10-20 μL) is used, which is important for the analysis of biological samples, such as blood or blood plasma [17]. The analytical problems associated with the determination of selenium in the blood can be divided into three major classes: spectral interferences, chemical interferences, and thermal pre-atomisation losses. Spectral interferences are generally minimized if higher ashing temperatures can be achieved. Optimization of this step is crucial for the method's accuracy, because of the organic matrix complexity. Many modifiers have been tested to improve the thermal stabilization of selenium. The most commonly used modifiers are: copper [18], nickel [19], palladium [20], platinum [21], silver [22], iridium and mixtures of some of them [23]. Palladium is one of the most suitable and commonly used modifiers in the determination of selenium in the blood. It provides better sensitivity compared to other modifiers, does not cause contamination of the graphite tube, and palladium is not determined for clinical purposes, unlike copper and nickel.

Spectral interference in the determination of selenium can occur as a result of high concentrations of chromium, cobalt, iron, nickel, and phosphorus because of spectral lines around 196.0 nm, where the selenium signal is measured. However, the concentrations of chromium, cobalt, and nickel in the blood are very low and errors from them can be eliminated when Zeeman background correction is used [16].

Usually, the biological sample preparation involves treatment of the blood or serum with nitric acid and Triton X-100 as a detergent, which provides lysis of cell membranes. However, there are no reports in the scientific literature on sample preparation with different types of detergents and the influence of their concentration. The purpose of this study was to define optimal sample preparation procedures, instrument parameters, and calibration procedures for direct ETAAS determination of

selenium in plasma and whole blood. The proposed method was applied to the determination of selenium in the plasma and whole blood of healthy individuals to obtain blood test results that include complete blood count (CBC), biochemical parameters, and thyroid status.

METHODS

Instrumentation

A Varian SpectrAA 640Z Zeeman electrothermal atomic absorption spectrometer equipped with a GTA-100 graphite furnace (Varian, USA) and PSD-100 autosampler (Varian, USA) was used. Pyrolytically coated tubes were used as atomizers. A Varian selenium hollow cathode lamp was used and the measurements were performed at 196.0 nm. Argon was applied as a protective gas and 10 μL samples were injected into the graphite furnace (GF). The graphite furnace operating parameters are presented in Table 1.

Table 1. Optimal parameters for Se determination by Zeeman ETAAS.

Parameter	Se
Wavelength	196.0 nm
Lamp current	10.0 mA
Calibration mode	Absorbance, peak height
Background correction	Zeeman
Drying	
Temperature	85; 95; 120°C
Time	5; 40; 10 s
Pyrolysis	
<i>Plasma</i>	
Temperature	1100°C
Ramp time	5 s
Hold time	30 s
<i>Blood</i>	
Temperature	1100°C
Ramp time	5 s
Hold time	35 s
Atomization	
Temperature	2500°C
Ramp time	0 s
Hold time	3 s
Cleaning	
Temperature	2500°C
Time	2 s
Gas	Argon

Only integrated absorbance values (peak height) were used for quantification.

Reagents

All reagents and standards were of analytical grade. Stock standard solutions for selenium were 1000 $\mu\text{g/mL}$ Solution Plus Inc. (USA). The working

standard solutions were prepared weekly by appropriate dilution and kept refrigerated at 4°C. The palladium matrix modifier solution (500 ppm) was prepared by the dilution of 10 g/L Pd(NO₃)₂ (Merck, Darmstadt, Germany) in 20% HCl (V/V) (Merck, Darmstadt, Germany). Sample diluting agents (nitric acid with a concentration in the range of 0.005–0.2% (V/V) and corresponding detergent with concentrations from 0.05 to 0.3% (V/V) were prepared by dilution of pure concentrated nitric acid (65% V/V) (Merck, Darmstadt, Germany) and Triton X-100, Tween 80, sodium dodecyl sulphate, digitonin and tauroglycocholic acid (Merck, Darmstadt, Germany) were used. Doubly distilled water with a conductivity of 0.3 µS/cm was used in all operations. All disposable devices were rigorously cleaned before use by brief immersion in hot concentrated nitric acid, cleaned with tap water and detergent, and rinsed twice with doubly distilled water.

Study design

The study group consisted of 57 apparently healthy volunteers, 31 women, and 26 men, with an average age of 44 years. All study participants signed an agreement for selenium testing of their blood. Clinical experiments were approved and performed according to the Ethics Committee provisions of the Department of Nuclear Medicine at Clinical Hospital „Dr. Trifun Panovski“ in Bitola (North Macedonia).

All volunteers were asymptomatic, did not have a history of chronic disease, and had normal or only trivial clinical findings. Clinical findings were considered to be trivial if there were no associated symptoms, if they were not caused by a potentially important medical illness, and if they did not induce any diagnostic or therapeutic activity (an old surgical scar or mild obesity would qualify as such a finding).

Health status was also checked by a blood test which included a complete blood count (CBC), different biochemical parameters, and thyroid status. The CBC parameters included white blood cell count, leukocyte differential counts of neutrophil, lymphocyte, monocyte, eosinophil, basophil, red blood cell count, hemoglobin, hematocrit, mean corpuscular volume, mean corpuscular hemoglobin, platelets, and red blood cell distribution width. The biochemical parameters determined were glucose, aspartate aminotransferase, alanine aminotransferase, serum creatinine, blood urea nitrogen, low-density lipoproteins, high-density lipoproteins, and triglycerides. The thyroid parameters included free triiodothyronine, free thyroxine, thyroid-stimulating hormone, antithyroglobulin antibody, and thyroperoxidase antibody. The inclusion criteria

were values in the reference ranges for all examined parameters in the blood test.

The exclusion criteria were individuals with a personal history of chronic diseases or any disease, low or high values for some examined parameters in a blood test, and individuals treated with selenium as a supplement.

Procedures

The blood samples were collected with plastic i.v. cannula with an injection valve and sodium citrate as an anticoagulant. Whole blood samples (500 µL) were diluted 1+2 with a sample diluting agent in a centrifuge tube. The diluted sample was vortexed vigorously for 60 s to produce a lysis of the blood cells. The samples were then centrifuged at 3000 rpm for 5 min. For selenium determination, 10 µL of clear red supernatant were introduced into the graphite furnace with a 5 µL solution of palladium modifier.

Plasma samples were obtained by centrifugation of blood for at least 15 minutes at 2500 rpm. After centrifugation, 500 µL of the clear supernatant were diluted 1+2 with a sample diluting agent and 10 µL were introduced into the graphite furnace with a 5 µL solution of palladium modifier.

The selenium concentration was determined by triple injections from each cup (57 volunteers, n=171) into the graphite furnace, operated under the conditions given in Table 1.

RESULTS AND DISCUSSION

Sample pre-treatment

The ability to tune a particular detergent for complete lysis of cell membranes and isolation of selenium-containing proteins is a major goal in the determination of total selenium in the blood. In order to investigate the influence of the different types of detergent (anionic, cationic, and nonionic) and their concentration on the determination of the total selenium concentration in blood and plasma, a series of experiments (with 3 replicates from each of 57 blood samples) were performed applying the instrumental parameters given in Table 1. In this study Triton X-100, Tween 80, sodium dodecyl sulfate (SDS), digitonin, tauroglycocholic acid, and urea, were used (RSD from 2.6% to 9.1%). As can be seen (Figure 1) the best results are obtained by using Triton X-100, Tween 80, and sodium dodecyl sulfate (SDS). Although the highest values of absorbance are obtained by using SDS, the difference in the absorbance obtained with these three detergents is not significant. Therefore, it can be concluded that these three detergents give satisfactory results in determining of total selenium concentration in blood and plasma.

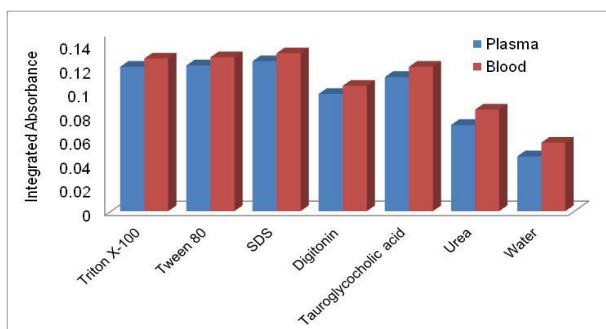


Figure 1. The influence of the different types of detergent on the determination of total selenium concentration in blood and plasma.

The efficiency of detergents is probably due to their structure. Digtonin and tauroglycocholic acid have hydrophobic tails with a steroidal structure, while Triton X-100, Tween 80, and SDS have a long alkyl chain. On the other hand, Triton X-100, Tween 80 and SDS have less hydrophilic heads compared to digtonin and tauroglycocholic acid. Specifically, the larger the detergent head, the lower is the detergent's propensity to break up lipid–lipid and protein–lipid interactions in biological membranes [24]. Also, it can be concluded that long alkyl chain detergents are more effective than detergents with steroid cores as hydrophobic tails [25].

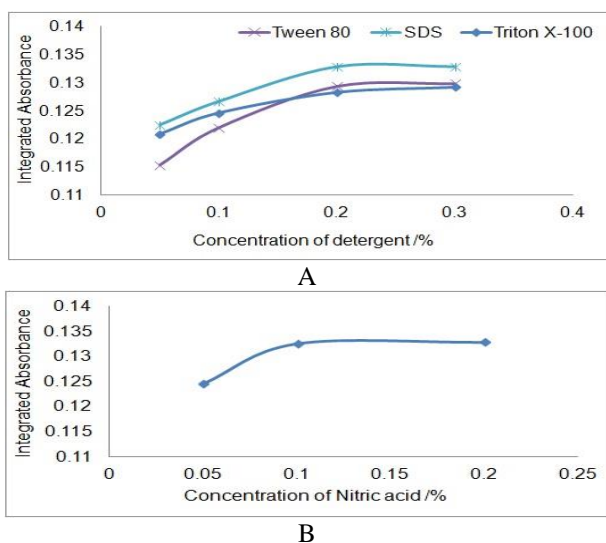


Figure 2. The influence of concentration of detergent (A) and nitric acid (B) on the integrated absorbance of selenium in the blood.

Furthermore, the influence of concentration of detergent and nitric acid on the measurement of selenium in blood was investigated ($n=3$). As can be seen from the results presented in Figure 2 the highest results were obtained by using 0.2% detergent solution and 0.1% nitric acid solution (RSD in the range of 1.9–6.8%).

Optimisation of instrumental parameters for ETAAS measurements

Optimization of the temperature program for Se determination by electrothermal atomic absorption spectrometry in human plasma and blood samples was performed. According to our previous results, parameters of the drying step were selected to allow the sample drop to dry slowly without sputtering [26]. Optimization of ashing temperatures was done by construction of pyrolysis–atomization curves from blood and plasma samples in the presence of palladium (500 ppm) modifier for thermal stabilization in ETAAS. The modifier was applied through the autosampler directly into the graphite furnace with a volume of 5 μL for 10 μL plasma or blood sample.

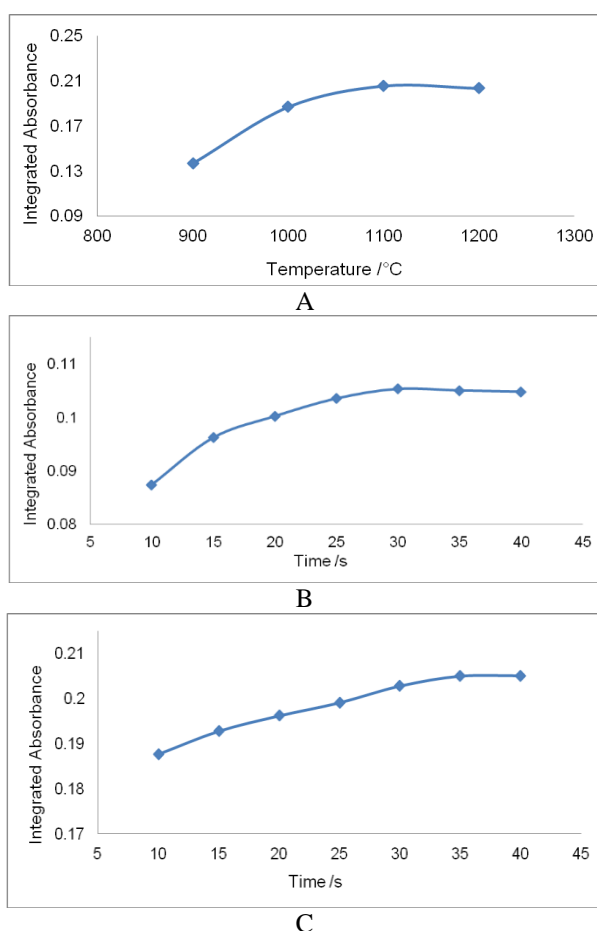


Figure 3. Effects of pyrolysis temperatures (A) and times on integrated absorbance for plasma (B) and blood (C) samples with Pd modifier.

Ashing temperatures (from 900°C to 1200°C) and ashing time (from 10 s to 40 s) were carefully optimized to ensure complete matrix decomposition and removal during this step by using wall atomization (pyrolytically graphite coated graphite tubes). Effects of pyrolysis temperatures and times on integrated absorbance for plasma and blood

samples with a Pd modifier are given in Figure 3 ($n=3$; RSD from 1.7% to 5.3%).

The optimal pyrolysis temperature was found to be 1100°C, while the optimal pyrolysis ramp time was established to be 5 s, and the hold time was 30 s for plasma and 35 s for blood samples. The complexity of the blood sample matrix affects the ashing time and the determination of total selenium. The atomization was performed at 2500°C by using a Pd modifier. The atomization ramp time was 1 s and hold time 3 s.

Calibration

Matrix interferences were evaluated according to the slopes of calibration curves obtained in the presence of the matrix (serum or blood), and for aqueous standard solutions. Results obtained are shown in Table 2 and clearly illustrate how strongly serum and blood matrices affected the degree of atomization of Se.

Table 2. Ratio of the slopes (b_m/b_o) for calibration curves in the presence of matrix (b_m) and aqueous standards (b_o), $n=3$.

Sample	b_m/b_o (mean \pm s)
Plasma	0.76 \pm 0.11
Plasma + Triton X-100	0.96 \pm 0.02
Plasma + Tween 80	0.97 \pm 0.01
Plasma + SDS	0.95 \pm 0.02
Blood	0.63 \pm 0.13
Blood + Triton X-100	0.95 \pm 0.02
Blood + Tween 80	0.94 \pm 0.03
Blood + SDS	0.94 \pm 0.02

The ratios of the slopes of the calibration graphs obtained in the presence of detergent (Triton X-100, Tween 80, or SDS) and Pd modifier are in the range of 0.94–0.97. These results confirm the capability of this detergent and modifier to reduce the spectral interferences and high background absorption values encountered with serum or blood matrices and at the same time to improve the degree of atomization of Se. Therefore, with detergent (Triton X-100, Tween 80, or SDS) and Pd modifier, calibration could be performed against a calibration curve prepared with an aqueous standard solution of Se.

Method validation

To test the accuracy of the proposed procedure for direct ETAAS determination of selenium in human plasma and blood, recovery experiments were performed. Plasma and blood samples were spiked with Se in the concentration range of 5–60 $\mu\text{g/L}$. Recovery experiments performed with human

plasma and blood samples in 0.1% nitric acid and 0.2% detergent (Triton X-100, Tween 80, or SDS) mixtures spiked with a known amount of selenium standard solution have shown 98.25–102.65 % yield, which is within the acceptable limits for the accuracy of the analytical methods (95-105%) [26]. The obtained results of recovery are presented in Table 3 ($n=3$, RSD 2.3-9.7%).

The limit of detection (LOD) and limit of quantification (LOQ) were evaluated based on three repeated analyses of blanks. LOD and LOQ were calculated as the average Se level in the blank plus 3 times and 10 times the standard deviation of the blank, respectively. For plasma samples the LOD was in the range of 0.56-0.62 $\mu\text{g/L}$ and LOQ was in the range of 1.87-2.07 $\mu\text{g/L}$ depending on the different detergents used. LOD and LOQ for blood samples were in the range of 0.64-0.72 $\mu\text{g/L}$ and 2.12-2.41 $\mu\text{g/L}$, respectively. The obtained results are shown in Table 4. The linearity range was 0.56–80 $\mu\text{g/L}$ Se. The precision of the methods was evaluated and the percent relative standard deviation (% RSD) was found to be from 1.55 % to 2.63 %. The obtained % RSD did not exceed 15% for all studied concentrations. These values for precision fell well within the criteria normally accepted in bioanalytical method validation.

Analytical application

The method was applied for the determination of Se in plasma and whole blood samples of 57 healthy volunteers (31 females and 26 male) with an average age of 44 years. The results obtained revealed that the selenium content varied in the range of 31.40–47.01 $\mu\text{g/L}$. No significant difference was revealed (below 11 %) between women 38.84 \pm 4.23 (31.40–47.01) $\mu\text{g/L}$ and men 40.43 \pm 3.62 (34.02–46.70) $\mu\text{g/L}$. The concentration of selenium in whole blood was higher by 23-25% in all cases (49.73–58.28 $\mu\text{g/L}$) compared to the determined concentration of selenium in plasma as a result of the distribution of selenoproteins in plasma and blood cells. In healthy humans, plasma Se is incorporated in two selenoproteins: selenoprotein P (SePP1) 40–70%, glutathione peroxidase (GPx3) 20–40%, while 6–10% of Se is bound to albumin in the form of selenomethionine, through the replacement of methionine. Free Se accounts for less than 1% of total plasma Se [27]. On the other hand, selenium in blood cells is incorporated in erythrocyte glutathione peroxidase. Plasma Se, very often used in various Se investigations, reflects rather short-term Se status, while platelet, leukocyte, and erythrocyte Se reflect its longer-term status. Our data reveal that the plasma selenium levels of healthy people in Macedonia are

among the lowest in Europe, but comparable with those in the Balkan region as shown in Table 5. These results are in agreement with previous reports for this biogeochemical region by Maksimović [28]: $35 \pm 7 \mu\text{g/L}$ and Čuparigova and Stafilov [26], $44.47 \pm 5.13 \mu\text{g/L}$ for selenium in blood plasma.

In this study, the obtained selenium plasma level was in a relatively narrow range of values compared to the results of previous reports. These differences are probably due to including criteria for chosen healthy individuals based on blood test results which include complete blood count (CBC), biochemical parameters and thyroid status

Table 3. Recovery results of plasma and blood samples.

Triton X-100					
Plasma			Blood		
Added ($\mu\text{g/L}$)	Found ($\mu\text{g/L}$)	Recovery (%)	Added ($\mu\text{g/L}$)	Found ($\mu\text{g/L}$)	Recovery (%)
0	31.51	-	0	39.09	-
10	41.48	99.70	10	49.16	100.7
20	51.67	100.80	20	59.62	102.65
30	60.92	98.03	30	68.85	99.20
Tween 80					
Plasma			Blood		
Added ($\mu\text{g/L}$)	Found ($\mu\text{g/L}$)	Recovery (%)	Added ($\mu\text{g/L}$)	Found ($\mu\text{g/L}$)	Recovery (%)
0	32.4	-	0	40.29	-
10	42.25	98.50	10	50.54	102.5
20	52.12	98.60	20	59.94	98.25
30	62.51	100.37	30	69.87	98.6
SDS					
Plasma			Blood		
Added ($\mu\text{g/L}$)	Found ($\mu\text{g/L}$)	Recovery (%)	Added ($\mu\text{g/L}$)	Found ($\mu\text{g/L}$)	Recovery (%)
0	33.38	-	0	41.46	-
10	43.64	102.6	10	51.39	99.3
20	53.44	100.3	20	61.51	100.25
30	63.23	99.5	30	71.85	101.30

Table 4. Statistical parameters of the calibration curve.

Detergent	Triton X-100		Tween 80		SDS	
	Plasma	Blood	Plasma	Blood	Plasma	Blood
Sample						
LOD $\mu\text{g/L}$	0.58	0.72	0.62	0.69	0.56	0.64
LOQ $\mu\text{g/L}$	1.92	2.41	2.07	2.30	1.87	2.12
Number of replicates	5	5	5	5	5	5
Calibration range $\mu\text{g/L}$	5–60	5–60	5–60	5–60	5–60	5–60

Table 5. Plasma selenium levels of healthy people in some countries in Europe.

Country	Plasma selenium level, $\mu\text{g/L}$	Reference
Croatia	69 ± 17	Becker et al. 1992 [29]
Bulgaria	66.5 ± 15.5	Tsalev et al. 2001 [30]
Bosnia-Herzegovina	64 ± 19	Maksimović et al. 1991 [28]
Greece	63 ± 14	Thorling et al. 1986 [31]
Montenegro	51 ± 26	Maksimović et al. 1991 [28]
Hungary	50 ± 11	Cser et al. 1996 [32]
Czech Republic	46 ± 14	Kvičala et al. 1995 [33]
Serbia	41 ± 20	Maksimović et al. 1991 [28]

CONCLUSION

The method for total selenium determination in human whole blood and plasma by ETAAS was optimized. The proposed method is simple, rapid, accurate and suitable for routine clinical analysis. The samples of blood and plasma were prepared by their dilution at a ratio of 1+2 with 0.2% detergent solution (Triton X-100, Tween 80, or SDS) and 0.1% nitric acid solution. It was found that the Pd modifier should be applied with the optimal pyrolysis temperature of 1100°C for 30 s for plasma and 35 s for blood and an optimal atomizing temperature of 2500°C. The method was applied for the determination of selenium in plasma and whole blood in healthy individuals. Health status was estimated by a blood test which includes complete blood count (CBC), biochemical parameters, and thyroid status. The obtained data for the selenium concentrations in plasma were in the range of 31.40–47.01 µg/L, which is a relatively narrow range of values compared to the results of previous reports. The concentrations of selenium in whole blood were higher by 23–25% in all samples due to the distribution of selenoproteins in plasma and blood cells.

REFERENCES

1. M. P. Rayman, *Lancet*, **379**, 1256 (2012), DOI: 10.1016/S0140-6736(11)61452-9.
2. L. H. Duntas, S. Benvenga, *Endocrine*, **48**, 756 (2015), DOI: 10.1007/s12020-014-0477-6.
3. J. Bleys, A. Navas-Acien, E. Guallar, *Arch. Intern. Med.*, **168**, 404 (2008), DOI:10.1001/archinternmed.2007.74.
4. H. Fritz, D. Kennedy, D. Fergusson, R. Fernandes, K. Cooley, A. Seely, S. Sagar, R. Wong, D. Seely, *PLoS One*, **6**, 26259 (2011), DOI:10.1371/journal.pone.0026259.
5. M. Etminan, J. M. Fitzgerald, M. Gleave, K. Chambers, *Cancer Causes Control.*, **16**, 1125 (2005), DOI:10.1007/s10552-005-0334-2.
6. S. R. Varikasuvu, V. S. Prasad, J. Kothapalli, M. Manne, *Biol. Trace Elem. Res.*, **189**, 361 (2019), DOI: 10.1007/s12011-018-1492-x.
7. C. Benstoem, A. Goetzenich, S. Kraemer, S. Borosch, W. Manzanares, G. Hardy, C. Stoppe, *Nutrients*, **7**, 3094 (2015), DOI:10.3390/nu7053094.
8. A. Drutel, F. Archambeaud, P. Caron, *Clin. Endocrinol.*, **78**, 155 (2013), DOI: 10.1111/cen.12066.
9. M. Ventura, M. Melo, F. Carrilho, *Int. J. Endocrinol.*, **2017** (2017), DOI: 10.1155/2017/1297658.
10. U. Schweizer, F. Streckfuss, P. Pelt, B. A. Carlson, D. L. Hatfield, J. Köhl, L. Schomburg, *Biochem. J.*, **386**, 221 (2005), DOI: 10.1042/BJ20041973.
11. K. Park, E. Rimm, D. Siscovick, D. Spiegelman, J. S. Morris, D. Mozaffarian, *Nutr Res Pract.*, **5**, 57 (2011), DOI:10.4162/nrp.2011.5.4.357.
12. M. Kieliszek, *Molecules*, **24**, 1298 (2019), DOI:10.3390/molecules24071298.
13. I. Hagarova, L. Nemcek-Korelkova, *Int. J. Exp. Spectrosc. Techniques.*, **5**, 1 (2020), DOI:10.35840/2631-505X/8525.
14. F. Li, E. Rossipal, D. Micetic-Turk, *Biol. Trace Elem. Res.*, **73**, 201 (2000), DOI:10.1385/BTER:73:3:201.
15. D. P. Bishop, D. J. Hare, F. Fryer, R. V. Taudte, B. R. Cardoso, N. Cole, P. A. Doble, *Analyst*, **140**, 2842 (2015), DOI:10.1039/c4an02283a.
16. P. H. Gardiner, D. Littlejohn, D. J. Halls, G. S. Fell, *J. Trace. Elem. Med. Biol.*, **9**, 74 (1995), DOI:10.1016/S0946-672X(11)80014-3.
17. T. H. Lin, W. C. Tseng, S. Y. Cheng, *Biol. Trace Elem. Res.*, **64**, 133 (1998), DOI:org/10.1007/BF02783330.
18. G. F. Kirkbright, S. Hsiao-Chuan, R. R. Snook, *At. Spectrosc.*, **1**, 85 (1980).
19. G. Alftan, J. Kumpulainen, *Anal. Chim. Acta.*, **140**, 221 (1982), DOI:org/10.1016/S0003-2670(01)95468-6.
20. X. Quan, H. Shau, H. Kai-Jin, *Talanta*, **32**, 23 (1985), DOI:10.1016/0039-9140(85)80008-4.
21. J. Bauslaugh, B. Radziuk, K. Saeed, Y. Thomassen, *Anal. Chim. Acta*, **165**, 149 (1984), DOI:org/10.1016/S0003-2670(00)85195-8.
22. J. Alexander, K. Saeed, Y. Thomassen, *Anal. Chim. Acta*, **120**, 337 (1989).
23. B. Welz, M. Melcher, G. Schlemmer, *Z. Anal. Chem.*, **316**, 271 (1983).
24. M. le Maire, P. Champeil, J. V. Möller, *Biochim. Biophys. Acta*, **1508**, 86 (2000), DOI:org/10.1016/S0304-4157(00)00010-1.
25. L. H. Urner, I. Liko, H. Y. Yen, K. K. Hoi, J. R. Bolla, J. Gault, F. G. Almeida, M. P. Schweder, D. Shutin, S. Ehrmann, R. Haag, C. V. Robinson, K. Pagel, *Nat. Commun.*, **11**, 564 (2020), DOI:10.1038/s41467-020-14424-8.
26. F. Čuparigova, T. Stafilov, *Chem. Sci. J.*, **9**, 1 (2011).
27. E. Reszka, E. Jablonska, J. Gromadzinska, W. Wasowicz, *Genes Nutr.*, **7**, 127 (2012), DOI:10.1007/s12263-011-0246-6.
28. Z. J. Maksimović, I. Djujić, V. Jović, M. Ršumović, *Biol. Trace Elem. Res.*, **33**, 187 (1991), DOI:10.1007/BF02784022.
29. D. Becker, Z. Romic, H. Kršnjavi, Z. Zima, *Biol. Trace Elem. Res.*, **33**, 43 (1992), DOI:10.1007/bf02783991.
30. D. L. Tsalev, L. Lampugnani, A. D'Ulivo, I. I. Petrov Jr, R. Georgieva, K. Marcucci, R. Zamboni, *Microchem. J.*, **70**, 103 (2001), DOI:org/10.1016/S0026-265X(01)00105-9.
31. E. B. Thorling, K. Overvald, J. Geboers, *Ann. Clin. Res.*, **18**, 3 (1986).
32. M. A. Cser, I. Sziklai-Laszlo, H. Menzel, I. Lombeck, *J. Trace Elem. Med. Biol.*, **10**, 167 (1996), DOI:10.1016/S0946-672X(96)80028-9.
33. V. Kvičala, J. Čerovska, J. Bednář, J. Janda, *Biol. Trace Elem. Res.*, **47**, 365 (1995), DOI:10.1007/BF02790139.

Minimization of free energy in dye removal from an aqueous solution by a biosorbent *Ricinus communis* using response surface technology

V. K. Sohpal

Department of Chemical Engineering & Bio Technology, SBS State University, Gurdaspur 143521, Punjab, India

Received: April 04, 2022; Accepted: September 22, 2022

The present work focuses on applying response surface methodology (RSM) for the minimization of Gibbs free energy for crystal violet dye (CVD) removal from a solution by a bioadsorbent *Ricinus communis*. Central composite design (CCD) and response surface methodology were used to conduct and analyze the experiments. The minimization of free energy was investigated as a function of three process variables, temperature (27-57 °C), absorbance (0.08-0.15 a.u.), and dye concentration (0.5-0.9 mg/l) with a fixed stirrer speed (120 rpm). The minimization of Gibbs free energy in the adsorption process was estimated by optimizing capacity of adsorption, percentage of dye removal, and temperature. The optimum values of percentage of removal of dye, adsorption capacity, and free energy were found to be 93.38 %, 0.965 mg/g, -8202.7 J/mol at temperature 55.9°C, respectively, having desirability > 95% for removal of crystal violet dye. The experimental observations were in good agreement with the predicted values.

Keywords: Response surface methodology; temperature; optimization; *Ricinus communis*; Gibbs free energy and minimization.

INTRODUCTION

The Asian textile industries consume large quantities of dyeing material and produce substantial amounts of colored wastewater. Different chemical techniques are used to remove various types of dyes to reduce water pollution. Adsorption is a prominent way to reduce water pollution with biomaterial and synthetic material. CuS nanoparticles loaded on activated carbon composite assist in removing indigo carmine and safranin-O [1]. RSM and ANN approach were used to optimize dye removal by adsorption, and results indicate 52.0% simulated behavior analogous to experimental work [2]. 3D graphene aerogel/ CaCO₃ nanocomposite adsorbent were used to remove acid red (88) dye from aqueous solutions and RSM showed the optimized process parameters to remove 100% dye in fixed criteria [3]. Protein-rich solution with aluminum-based nanosheets was synthesized to remove congo red and crystal violet, and RSM observed with the optimum adsorbent dosages was 0.16 g for 50 mg/L, and 0.12 g for 100 mg/L for CR and CV dye solutions, respectively [4]. RSM was used to maximize the percent gel fraction to the removal of rhodamine-B (70%) and auramine-O (63%) from a mixture with an adsorbent dose of 700 mg [5]. ANN and RSM were applied to analyze the fixed bed adsorption of FD&C red 40 dye on polyurethane/chitosan foam and found that ANN can predict the experimental data with more accuracy than the RSM [6]. Chitosan cross-linked with graphene oxide was used to

remove the dye safranin orange, and optimum parameters predicted using the RSM model are pH 6.82, initial SO concentration 425 mg/L [7]. Nanocomposite hydrogel from nano bismuth iron oxide synergistically coupled network of acrylic acid and RSM techniques was applied to optimize the kinetic variables [8]. Scrutinized were the different physicochemical processes using RSM in dye removal and some suggestions were made for future work on adsorption, advanced oxidation processes, coagulation/flocculation, and electro-coagulation [9]. Ni-doped ferric oxy-hydroxide FeO (OH) nanowires were synthesized for removal of safranin-O and indigo carmine and adsorption performance was analyzed using RSM, ANN, and linear algebra-based models [10]. Box–Behnken design was used to optimize the efficiency of amine-functionalized Fe₃O₄ magnetic nanoparticles for removing RB5 azo dye from an aqueous solution [11]. Coagulants were used to achieve the optimum conditions for the removal of color and turbidity using a biopolymer with the RSM design and it was observed that at optimum conditions the removal of color and turbidity was 76.20% and 90.14%, respectively [12].

The nanocomposite of MnFe₂O₄ synthesized for its application as an adsorbent for direct red 16 (D R16) removal and central composite rotatable design (CCRD) combined with RSM was used to optimize the adsorption capacity [13]. Graphene oxide nanoplatelets were used for simultaneous adsorption of acid yellow 36 (AY) and acid blue 74 (AB) and

* To whom all correspondence should be sent:
E-mail: vipan752002@gmail.com

process parameters were optimized for best results using RSM and ANN [14]. RSM has been applied to determine the optimal adsorbent composition and experimental conditions for the removal of basic violet and malachite green oxalate dyes using activated phosphorus slag-based cylindrical adsorbent [15]. RSM was utilized to simulate and determine the optimum conditions of RB19 removal by functionalized MWCNTs using adsorbent dose, initial dye concentration, and pH and R^2 -value of 89.11% and adjusted R^2 -value of 95.72% were obtained [16]. RSM-CCD techniques were used to optimize the synthesis scheme of semi-IPN nanocomposite adsorbent for removing bieberich scarlet and crystal violet. Results suggested the recyclability and reusability of the adsorbent materials for the textile industry [17]. RSM and ANN modeling were used to remove Pb (II) by thiosemicarbazide-modified chitosan, and the desirability degree for the RSM optimization predicted was 0.981 [18]. Iron zero-valent nanoparticles were synthesized for removal of methylene blue dye in water solution. CCD was applied to optimize the removal of dye and R^2 and adj. R^2 correlation coefficients for the model observed were 0.96 and 0.93, respectively [19]. RSM method was used to optimize the palm oil for caffeine adsorption and observed that removal efficiency (%) at the optimal conditions, 0.20 g of adsorbent, initial caffeine concentration of 20 mg/L, and acidic medium was about 95% [20]. RSM-BBD was employed to optimize the MO dye removal efficiency from aqueous solution by cross-linked Chi-TPP/NTC). The F-value for MO removal efficiency was 93.4 (corresponding p-value < 0.0001) [21]. Shoes waste adsorbents with CCD techniques were applied to investigate the removal of cadmium (Cd) from aqueous solution and wastewater. The result confirms CCD as the best statistical model to predict the response with good accuracy and reliability [22].

Adsorption isotherms and kinetic models investigated the use of *Ricinus communis* as a natural adsorbent for removing dyes from aqueous solution and the natural adsorbent was found viable at an economical cost [23]. The present study focused on *Ricinus communis* as a natural adsorbent for CV dye removal using RSM and CCD statistical techniques. The RSM with CCD was used to develop a mathematical model to predict the desirability parameter using an optimized correlation between maximum adsorption capacity, minimization of free energy, and a higher percentage of dye removal.

MATERIALS AND METHODS

In this study, CVD (IUPAC: Tris (4-(dimethylamino) phenyl) methylum chloride) was used to prepare synthetic dye wastewater. This dye was obtained from Loba Chemicals, Mumbai, India. Analytical grade (80% purity) CVD was used without purification to prepare the stock solution (1000 mg/l) by dissolving a precise quantity of dye in distilled water. *Ricinus communis* leaves were subjected to physical (washing, boiling, and soaking) and chemical (drying) treatment and finally the dried leaves were crushed to a particle size of about 53 μm . The maximum absorbance wavelength (λ_{max}) for CVD was found to be 585 nm.

Batch adsorption investigations were performed to evaluate the effect of various process variables on the dye removal percentage, adsorption capacity, and Gibbs free energy. All the batch adsorption experiments were conducted according to the CCD matrix at random to reduce the possibility of errors. In addition, minimum and maximum levels of each of the three input process variables [temperature (27-57°C), absorbance (0.08-0.15 a.u.), and dye concentration (0.5-0.9 mg/L) with a fixed stirrer speed (120 rpm)] were evaluated through pre-trial experiments [23].

RESULTS AND DISCUSSION

Effect of temperature on free energy

The temperature-dependent thermodynamic variable changes in the Gibbs free energy (ΔG°), enthalpy (ΔH°), and entropy (ΔS°) of the adsorption process were estimated using the correlation $\Delta G^\circ = \Delta H^\circ - T\Delta S^\circ$.

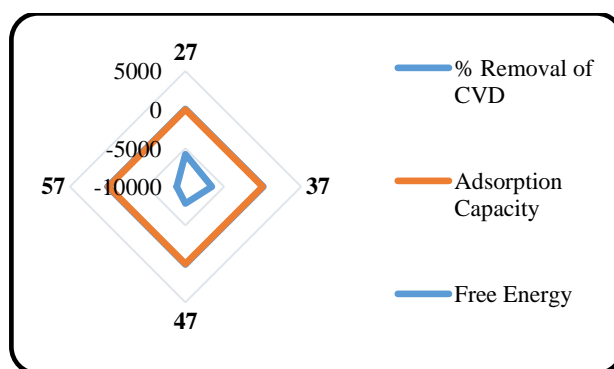


Fig. 1. Temperature vs. adsorption capacity, free energy and % removal of CVD

A plot of ΔG° versus T yields a straight line with the slope of $-\Delta S^\circ$ and intercept of ΔH° . The values of ΔG° obtained using different temperatures of the reaction are shown in Fig. 1. The ΔH° and ΔS° values during the adsorption process determined from the slope and intercept are 25670 J/mol and

104.2 J/mol, respectively, for CVD. The positive values indicate that the adsorption process is endothermic in nature, and forward reactions are favored.

Central composite design for experimental work

CCD was applied to assess the optimum operating parameters for CVD removal using Design

operating Expert software. In this study, the three independent variables investigated for the removal of CVD, adsorption capacity and free energy were t, temperature (27-57°C), a, absorbance (0.08-0.15 a.u.), and c, concentration of dye (0.5-0.9 mg/L). The responses of the percent removal of CVD, adsorption capacity (mg/g), and Gibbs free energy (J/mol) using CCD are represented in Table 1.

Table 1. Full factorial CCD matrix for CVD removal absorption process

Run order using CCD	Temperature (t, °C)	Absorbance (a)	Conc. of dye (c)	% Removal of dye	Adsorption Capacity	Free Energy		
19	2	Center	47	0.115	0.7	93.88	0.945	-7001.1
17	4	Center	47	0.115	0.7	93.87	0.945	-7001.1
15	5	Center	47	0.115	0.7	93.88	0.946	-7001.6
20	8	Center	47	0.115	0.7	93.89	0.945	-7001.8
16	11	Center	47	0.115	0.7	93.88	0.948	-7001.2
18	17	Center	47	0.115	0.7	93.88	0.945	-7001.1
14	6	Axial	47	0.115	0.9	90.04	0.918	-6992.01
10	7	Axial	57	0.115	0.7	93.04	0.963	7793.01
9	14	Axial	27	0.115	0.7	91.04	0.910	-5783.01
11	15	Axial	47	0.08	0.7	93.95	0.962	-7695.13
13	16	Axial	47	0.115	0.5	93.22	0.961	-7692.15
12	20	Axial	47	0.15	0.7	92.95	0.95	-7700.13
3	1	Fact	37	0.15	0.5	91.22	0.923	-6980.2
6	3	Fact	57	0.08	0.9	92.55	0.921	-8870
4	9	Fact	57	0.15	0.5	91.04	0.91	-8859
1	10	Fact	37	0.08	0.5	92.22	0.922	-6950
8	12	Fact	57	0.15	0.9	92.04	0.92	-8872
2	13	Fact	57	0.08	0.5	92.53	0.93	-8850
5	18	Fact	37	0.08	0.9	91.05	0.91	-6977
7	19	Fact	37	0.15	0.9	91.04	0.914	-6970

RSM modeling for percentage removal of dye

Statistically designed experiments using CCD were performed to study the effect of the independent variables on the percent removal of dye. The design matrix corresponding to predicted results is shown in Table 1. A 2nd order polynomial model was developed using the observed data in terms of coded factors (t, a, c) employing RSM as given in eq. (1):

$$\text{Percent removal of dye} = 62.66 + 0.76 \times t + 47.23 \times b + 30.24 \times c - 0.60t \times b + 0.096t \times c - 0.007 \times t^2 - 136.73 \times b^2 - 25.66 \times c^2 \quad (1)$$

ANOVA results presented in Table 2 were used to evaluate the model. Coefficients of the model were estimated using regression analysis, and the R-squared coefficient was evaluated for judgment of fitness of the model. As a result, the model was established to be significant and applicable to track the design domain. Fisher test (F) statistical technique significance on the model was also analyzed. A small p-value compared to F showed that the quadratic model developed was statistically significant and used to predict the percentage of dye removal.

Temperature, absorbance, and concentration of CVD are essential parameters for the adsorption

process. Fig. 2(a) shows a three-dimensional relationship between the temperature and absorbance concerning the percentage of CVD removal. The percentage of CVD removal increases from 91% to 96% as the solution temperature increases from 27 to 57°C. Because the adsorption increased as the temperature increased, the system is considered to be endothermic. On the same temperature trend, the absorbance declines up to 5% due to that CVD removal percentage.

From the RSM surface plot, it is clear that at 47°C with absorbance 0.115 a.u. 93.89% of CVD is removed which is close to the experimental result of 94.70%. Fig. 2(b) shows a three-dimensional relationship between the temperature and

concentration of CVD concerning the percentage of CVD removal. Due to the endothermic chemisorption process, the lower concentration of dye improves the CVD removal percentage. As the temperature rises, the bonding of dye and active sites of the adsorbent weakened. A virtue of that interaction between the solute and solvent becomes stronger. In addition, dye solubility also increased at elevated temperature. RSM surface plot obviously reflects that at 47°C with dye concentration 0.7 mg/L 93.89% of CVD is removed, close to the experimental result. The variation between experimental and ANOVA predicted result for % CVD removal is less than 1% due to $R^2 = 0.9891$, Adj. $R^2 = 0.9813$, Pred. $R^2 = 0.9585$.

Table 2. ANOVA for response surface reduced quadratic model for percentage removal of dye

Source	Sum of Squares	df	Mean Square	F Value	p-Value Prob. > F	Percent Contribution	Remarks
Model	27.317	8	3.415	125.32	< 0.0001		Significant
<i>t</i>	1.339	1	1.339	49.143	< 0.0001	5.11	
<i>b</i>	2.7197	1	2.72	99.815	< 0.0001	9.81	
<i>c</i>	0.7362	1	0.736	27.02	0.0003	2.64	
<i>t</i> × <i>b</i>	0.3612	1	0.361	13.258	0.0039	1.30	
<i>t</i> × <i>c</i>	0.2965	1	0.296	10.88	0.0071	1.05	
<i>t</i> ²	8.7486	1	8.749	321.08	< 0.0001	31.66	
<i>b</i> ²	0.4043	1	0.404	14.839	0.0027	1.44	
<i>c</i> ²	15.189	1	15.19	557.45	< 0.0001	54.98	
Residual	0.2997	11	0.027			1.08	
Lack of Fit	0.1722	6	0.029	1.1251	0.4583		Not significant
Pure Error	0.1275	5	0.026				
Cor Total	27.617	19					

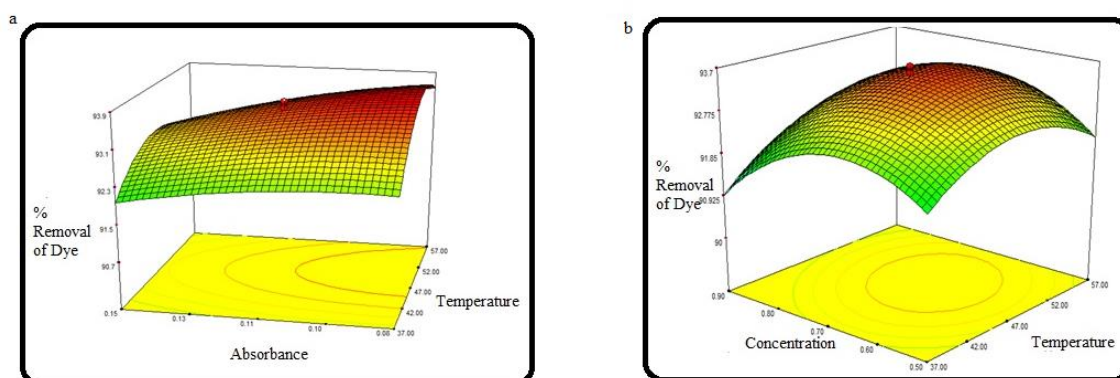


Fig. 2 (a) Surface plots of percent removal of dye with respect to temperature and absorbance; (b) Surface plots of percent removal of dye with respect to temperature and concentration of dye.

RSM modeling for adsorption capacity

CCD was performed to investigate the effect of the independent variables on adsorption capacity. Table 1 represents the design matrix and corresponding predicted results. A polynomial model was developed for adsorption capacity using RSM as given in eq. (2):

$$\text{Adsorption capacity} = 0.62 + 0.013 \times t - 0.88 \times b + 0.19 \times c - 0.00075 \times t \times c + 1.21 \times b \times c - 0.00013 t^2 - 0.314 b^2 - 0.257 c^2 \quad (2)$$

ANOVA results presented in Table 3 were used to evaluate the model. Fig. 3(a) shows a three-dimensional relationship between the temperature and concentration of dye for adsorption capacity. The adsorption capacity increases from 0.910 to 09.68 as temperature increases from 27 to 57°C. The

adsorption capacity of the adsorbate increased as the temperature increased due to endothermic effect. From RSM surface plot it is clear that at 57°C with a concentration of dye 0.7 mg/L the adsorption capacity is 0.962, close to the experimental result 0.953. Fig. 3 (b) shows a three-dimensional relationship between the absorbance and concentration of CVD for adsorption capacity. The adsorption capacity increases with the higher initial concentration of dye from 0.5 mg/L to 0.7 mg/L at maximum temperature 57°C, and the sorption capacity increased from 0.71 to 0.9 mg/L. In contrast, the removal percentage of dye decreased from 93% to 91%. The variation between experimental and ANOVA predicted result for adsorption capacity is lower than 1% due to R² 0.9881. Adj. R²= 0.9795, Pred. R²= 0.9574.

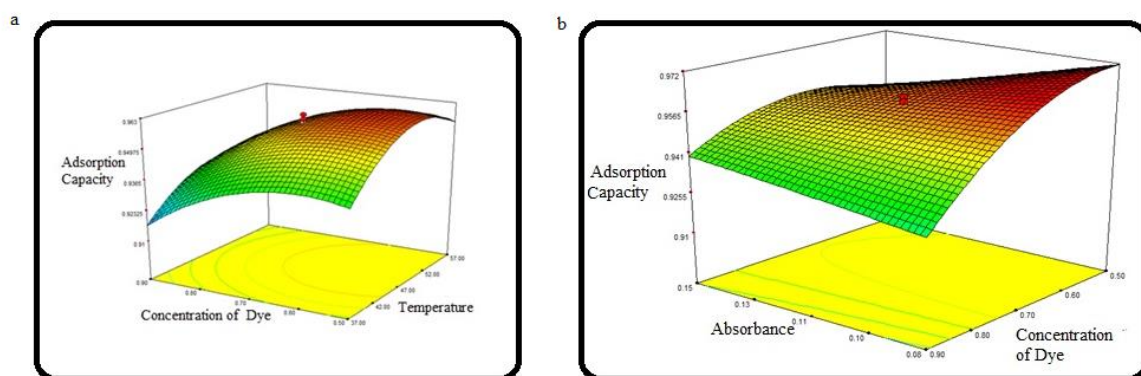


Fig. 3. (a) Surface plots of adsorption capacity with respect to temperature and concentration of dye; (b) Surface plots of adsorption capacity with respect to absorbance and concentration of dye.

Table 3. ANOVA for response surface reduced quadratic model adsorption capacity

Source	Sum of Squares	df	Mean Square	F Value	p-Value Prob. > F	Percent Contribution	Remarks
Model	0.0072	8	0.0009	114.31		< 0.0001	Significant
t	0.0006	1	0.0006	77.38	8.57	< 0.0001	
b	0.0001	1	0.0001	22.48	1.42	0.0006	
c	0.002	1	0.002	254.46	28.57	< 0.0001	
t×c	0.000017	1	0.000017	2.28	0.24	0.1591	
b×c	0.0005	1	0.0005	73.25	7.14	< 0.0001	
t ²	0.0026	1	0.0026	331.24	37.14	< 0.0001	
b ²	0.0000021	1	0.0000021	0.27	0.02	0.6128	
c ²	0.0015	1	0.0015	193.20	21.42	< 0.0001	
Residual	0.000086	11	0.0000078		1.22		
Lack of Fit	0.00005	6	0.0000084	1.17		0.4389	Not significant
Pure Error	0.00003	5	0.0000072				
Cor Total	0.00730295	19					

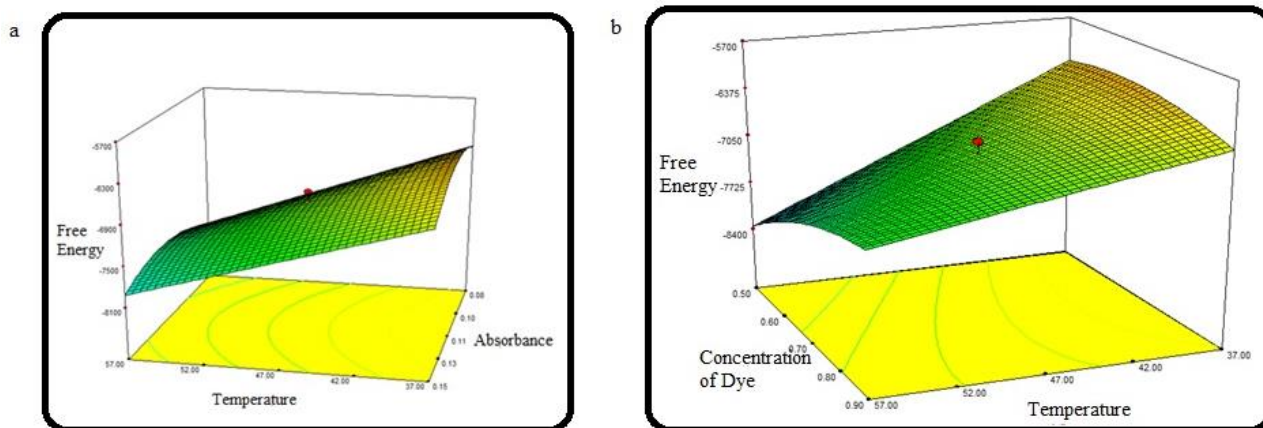


Fig. 4. (a) Surface plots of free energy with respect to temperature and absorbance; (b) Surface plots of free energy with respect to temperature and concentration of dye.

Table 4. ANOVA for response surface reduced quadratic model free energy

	Sum of Squares	df	Mean Square	F Value	Percent Contribution	p-Value Prob > F	Remarks
Model	9665926.6	9	1073992	54.49635		< 0.0001	Significant
t	6666539.9	1	6666540	338.2727	67.59	< 0.0001	
b	7064.4328	1	7064.433	0.358463	0.07	0.5627	
c	471109.56	1	471109.6	23.90498	4.77	0.0006	
t×b	56146.005	1	56146	2.848953	0.56	0.1223	
t×c	799986	1	799986	40.59279	8.11	< 0.0001	
b×c	42369.605	1	42369.6	2.149913	0.42	0.1733	
t ²	675.29679	1	675.2968	0.034266	0.006	0.8568	
b ²	1272503.4	1	1272503	64.5692	12.90	< 0.0001	
c ²	468403.01	1	468403	23.76764	4.74	0.0006	
Residual	197075.91	10	19707.59		1.9		
Lack of Fit	159903.77	5	31980.75	4.301711		0.0676	Not significant
Pure Error	37172.135	5	7434.427				
Cor Total	9863002.5	19					

Table 5. Optimization of process parameters for desirability

Temperature	Absorbance	Conc.	% Removal of dye	Ads. Capacity	Free energy	Desirability	Selection
55.9	0.08	0.6	93.38667	0.965	-8202.7	0.95082	Selected
56.1	0.08	0.59	93.33397	0.965	-8240.9	0.94917	
55.5	0.08	0.61	93.4876	0.965	-8123.6	0.93274	
55.9	0.08	0.6	93.38955	0.965	-8191.5	0.92983	
55.6	0.08	0.59	93.37901	0.965863	-8194.5	0.92396	
56.7	0.08	0.59	93.28879	0.963948	-8286.1	0.899312	

RSM modeling for free energy

Free energy modeling was performed using CCD to investigate the effect of the independent variables on free energy. Table 4 represents the design matrix and corresponding predicted results for free energy. A polynomial model was developed for free use employing RSM as given in eq. (3):

$$\text{Free energy} = -2495.98 - 201.638 \times t + 36614.52 \times b - 1388.26 \times c + 239.35 \times t \times b + 158.11 \times t \times c + 10396.43 \times b \times c - 0.06845 t^2 - 242573 b^2 - 4507.11 c^2 \quad (3)$$

ANOVA results presented in Table 4 were used to evaluate the model. Fig. 4(a) shows a three-dimensional relationship between the temperature, absorbance, and concentration of dye with respect to free energy. Gibbs free energy increased with increase in temperature as reflected in Table 1 and RSM because the reaction is spontaneous and exergonic. Adsorption of dye is accompanied by decrease in the ΔG because the molecules of the adsorbate are held on surface of the solid adsorbent and as a result the entropy decreases. The experimental results and RSM prediction overlap quantitatively. On increasing the temperature from 27°C to 67°C dye mobility increases to a maximum value at corresponding temperature 55°C and dye concentration of 0.65 mg/L.

The variation between experimental and ANOVA predicted free energy is 0.99% and other statistic parameters of the ANOVA response surface reduced the quadratic model for free energy. The $R^2 = 0.9800$ of the free energy variable is well explained by the variance of the independent variable of the process. Similarly, Adj. $R^2 = 0.9620$ satisfies the experimental curve, and Pred. $R^2 = 0.8686$ gives a satisfactory regression model under current constraints.

Optimization of process variables

The consistency and optimization of developed models was tested by performing confirmation experiments. The condition for the confirmation runs was set within the range of process parameters. The predicted value of performance variables was calculated from eqs. 1-3. Finally, the optimal values of the process, which maximize the process parameters of adsorption, were estimated from the desirability function of the RSM.

The calculated response was converted into desirability scale ranging from 0-1. The outcomes are represented in Table 5. It shows a maximum desirability 0.94 for a temperature range of 55.9-60.0 °C, concentration of dye 0.6 mg/L and percent removal of dye around 93.4 with constant absorbance of 0.08 a.u. The consistency and

optimization of developed models was tested by performing confirmation experiments.

CONCLUSIONS

Response surface methodology - Central composite design (RSM-CCD) was successfully utilized as a statistical tool for optimizing free energy in dye removal from an aqueous solution by a bioadsorbent *Ricinus communis*. The highest percentage of CVD removal for experimental runs was 96 %, using 10 mg/L of adsorbent and a contact time of 2 hours. The correlation coefficient, R^2 for CVD removal in all ANOVA models, was found to be 0.9878. The optimum conditions for CVD removal, which were predicted by RSM, were found to be: temperature 55.9 °C, absorbance 0.08 a.u., initial concentration 0.6 mg/L, which resulted in maximum CVD removal of 93.38 % and minimized free energy 8202.7 J/mol at the desirability of 0.95.

REFERENCES

1. M. Dastkhooon, M. Ghaedi, A. Asfaram, H. Javadian, *Applied Organometallic Chemistry*, **32**(5), e4350 (2018).
2. M. R. Gadekar, M. M. Ahammed, *Journal of Environmental Management*, **231**, 241 (2019).
3. N. Arsalani, R. Nasiri, M. Zarei, *Chemical Engineering Research and Design*, **136**, 795 (2018).
4. A. M. Ealias, M. P. Saravanakumar, *Journal of Environmental Management*, **206**, 215 (2018).
5. J. Sharma, A. S. Chadha, V. Pruthi, P. Anand, J. Bhatia, B. S. Kaith, *Journal of Environmental Management*, **190**, 176 (2017).
6. R. R. Schio, N. P. G. Salau, E. S. Mallmann, G. L. Dotto, *Chemical Engineering Communications*, **1** (2020).
7. S. Debnath, K. Parashar, K. Pillay, *Carbohydrate polymers*, **175**, 509 (2017).
8. B. S. Kaith, U. Shanker, B. Gupta, J. K. Bhatia, *Reactive and Functional Polymers*, **131**, 107 (2018).
9. S. Karimifard, M. R. A. Moghaddam, *Science of the Total Environment*, **640**, 772 (2018).
10. M. Dastkhooon, M. Ghaedi, A. Asfaram, M. H. A. Azqhandi, M. K. Purkait, *Chemical Engineering Research and Design*, **124**, 222 (2017).
11. S. M. Pormazar, A. Dalvand, *International Journal of Environmental Analytical Chemistry*, **1** (2020).
12. M. M. Momeni, D. Kahfroushan, F. Abbasi, S. Ghanbarian, *Journal of Environmental Management*, **211**, 347 (2018).
13. L. A. Kafshgari, M. Ghorbani, A. Azizi, S. Agarwal, V. K. Gupta, *Journal of Molecular Liquids*, **233**, 370 (2017).
14. P. Banerjee, S. R. Barman, A. Mukhopadhyay, P. Das, *Chemical Engineering Research and Design*, **117**, 43 (2017).
15. A. Salehi, E. N. Kani, *Adsorption*, **4-7**, 647 (2018).
16. S., Karimifard, M. R. A. Moghaddam, *Process Safety and Environmental Protection*, **99**, 20 (2016).

17. A. K. Sharma, B. S. Kaith, V. Tanwar, J. K. Bhatia, N. Sharma, S. Bajaj, S. Panchal, *International Journal of Biological Macromolecules*, **129**, 214 (2019).
18. S. P. G. Zaferani, M. R. S. Emami, M. K. Amiri, E. Binaeian, *International Journal of Biological Macromolecules*, **139**, 307 (2019).
19. M. Khosravi, S. Arabi, *Water Science and Technology*, **74**(2), 343 (2016).
20. L. L. Melo, A. H. Ide, J. L. S. Duarte, C. L. P. Zanta, L. M. Oliveira, W. R. Pimentel Meili, *Environmental Science and Pollution Research International*, **27**(21), 27048 (2020).
21. A. Jawad, *Science Letters*, **14**(2), 1 (2020).
22. M. Iqbal, N. Iqbal, I. A. Bhatti, N. Ahmad, M. Zahid, *Ecological Engineering*, **88**, 265 (2016).
23. A. Mahajan, V. K. Sohpal, V. K. Bulasara, *Journal of Chemical Technology & Metallurgy*, **54**(1), 111 (2019).

Polyphenols in Bulgarian medicinal fruits

S. P. Tsanova-Savova*, S. S. Paneva, P. N. Koleva, M. L. Vizeva

Medical University – Sofia, Medical College Yordanka Filaretova, 3, Yordanka Filaretova Str., Sofia 1606, Bulgaria

Received: May 04, 2022; Revised: August 08, 2022

The aim of the study is to determine the total phenols, total flavonoids and individual representatives of flavonoids – catechin, epicatechin and rutin in decoctions of widely used fruits of medicinal plants in Bulgaria. This would allow to gather new analytical data for their polyphenol content and correspondingly, for their antioxidant potential. In the present study various fruits of medicinal plants were studied: elderberry (*Sambucus nigra*), cranberry (*Vaccinium vitis-idaea*), hawthorn (*Crataegus monogyna*), rosehip (*Rosa canina*), dogwood (*Cornus mas*), blackthorn (*Prunus spinosa*), and black chokeberry (*Aronia melanocarpa*). For the analytical determination of the content of total phenols the Folin-Ciocalteu method was used; for total flavonoids – the method with aluminium trichloride and individual flavonoids - catechin, epicatechin and rutin, were determined by HPLC with PDA detection. The results show that decoctions of rosehip have higher contents of total phenols and total flavonoids but no catechin, epicatechin or rutin. The highest amount of rutin was detected in elderberry (10700 µg/100 ml) along with very high contents of total phenols and total flavonoids, suggesting the promotion of *Sambucus nigra* to be used in antioxidant phytochemical formulations.

Keywords: Polyphenols, Medicinal plants, Total phenols, Total flavonoids, Fruit decoctions

INTRODUCTION

Around the world, there is traditional knowledge about the beneficial health effects of a traditionally used variety of medicinal plants. The flora in Bulgaria offers a great variety of plants - over 4000 higher plants are identified, and about 800 of them are known to have healing properties [1]. The presence of such a large variety of plants and a large number of compounds of plant origin predetermines that the phytotherapeutic potential of natural plants is vast and still insufficiently studied. A significant part of the existing studies is related to the antioxidant effect of the compounds contained in medicinal plants.

Due to the free radical metabolism of oxygen, the existence of aerobic organisms in an oxygen environment is possible only due to the functioning of appropriate defense systems. Under physiological conditions, most of the damaging effects of free radicals are prevented by the action of substances with antioxidant properties, which form the body's antioxidant defenses [2-4].

Medicinal plants and fruits that are widely used in folk medicine are a rich source of antioxidant polyphenols and in particular flavonoids [5, 6]. Polyphenols, including the flavonoids group, are secondary metabolites in higher plants, and more than 8,000 compounds are currently known [7]. They are present in various parts of plants used for food, as well as in a number of medicinal plants. It

is interesting to note that half of the polyphenol compounds belong to the group of flavonoids and are found as aglycones, glycosylated forms and methylated derivatives [8].

Pharmacological studies of flavonoids have shown that they have antioxidant, cardioprotective, antispasmodic, antihypertensive, antimicrobial, antiviral, antiulcer, antidiabetic, antitumor and other effects [9-13].

According to the WHO, today 80% of the world's population relies on the healing properties of plants in various forms [14]. Even today, 11% of the 252 drugs considered as basic and essential by the WHO were exclusively of flowering plant origin and up to 50% of the approved drugs during the last 30 years are directly or indirectly from natural products [15]. In Bulgarian folk medicine a wide variety of infusions and decoctions is used, reflected not only in the seasonal collection of herbs, but in the presence of a wide net of herbal pharmacies in the country. However, no sufficient data for their polyphenol profile are available.

The aim of the present study is to determine the total phenols, total flavonoids and individual representatives of flavonoids – catechin, epicatechin and rutin in decoctions of fruits of medicinal plants widespread in Bulgaria in order to provide new analytical data for their polyphenol content and, correspondingly, to their antioxidant potential.

* To whom all correspondence should be sent:
E-mail: s.tsanova-savova@mc.mu-sofia.bg

EXPERIMENTAL

Sample preparation

In the present study the following fruits of medicinal plants were studied: elderberry (*Sambucus nigra*), cranberry (*Vaccinium vitis-idaea*), hawthorn (*Crataegus monogyna*); rosehip (*Rosa canina*), dogwood (*Cornus mas*), blackthorn (*Prunus spinosa*), black chokeberry (*Aronia melanocarpa*). For analytical determination of the content of total phenols, total flavonoids and individual flavonoids - catechin, epicatechin and rutin, an average fruit sample was prepared from three individual samples (100 g), with a dissipation degree, according to the pharmacopoeia requirements, purchased from the pharmacy net in Sofia.

Preparation of water decoctions

In order to obtain a quality aqueous extract, the decoctions preparation followed a pharmacopoeia technological regime, accordingly – the contact time was not less than 40 min and the ratio plant material/water was 5 g of dry fruit/100 g of distilled water. The fruit material was boiled in distilled water for 5-10 minutes, according to the manufacturer's instructions. Soak for 30-35 minutes, cool and strain. The samples obtained were stored at 4 °C without the addition of preservatives. The samples were analyzed no later than 24 hours.

Chemicals

Certified reference materials - catechin and gallic acid were purchased from Sigma (St. Louis, MO), epicatechin and rutin trihydrate from Alfa Aesar (Thermo Fisher Scientifics, Kandel, Germany). Folin-Ciocalteu reagent was purchased from Alfa Aesar. Solvents - acetonitrile, methanol and water are of HPLC purity (Macron Fine Chemicals, Avantor, Gliwice, Poland). All other chemicals and reagents used have a degree of purity p.a. and were purchased from Alfa Aesar.

Determination of total phenols

Folin-Ciocalteu reagent is used to determine total phenols due to its ability to oxidize polyphenols and form a blue complex with them, which is determined spectrophotometrically at a wavelength $\lambda = 750$ nm. The determination was performed according to Marinova *et al.* [16]. Briefly, an aliquot of 1 ml of a suitably diluted aqueous extract or standard gallic acid (GA) solution was added to a 25 ml volumetric flask containing 9 ml of distilled water. 1 ml of Folin-Ciocalteu reagent was added to the solution and after 5 min 10 ml of 7% Na_2CO_3 was added. The solution was brought to the mark with distilled

water, stirred and allowed to stay for 90 min at room temperature. The absorbance was measured against a reagent blank at $\lambda = 750$ nm. The method of external standard with gallic acid was used to calculate the amount of total phenols. Results are expressed as gallic acid equivalent (mg GAE/100 ml). The parameters of the method were as follows: LOQ 0.10 μg GAE/ml; LOD 0.21 μg GAE/ml; RSD = 3.8 %, no systematic error was found [17].

Determination of total flavonoids

Total flavonoids were determined according to Marinova *et al.* [16]. An aliquot of 1 ml of aqueous decoction or standard solution of rutin was placed in a 10 ml volumetric flask containing 4 ml of distilled water. 0.3 ml of 5% NaNO_2 was added to the solution and after 5 min 0.3 ml of 10% aqueous AlCl_3 was added. After 6 min, 2 ml of 1 M NaOH was added and the solution was made up to the mark with distilled water, stirred and allowed to stay for 30 min. The absorbance of the formed pink complex was compared to a reagent blank at a wavelength $\lambda = 510$ nm. The total flavonoids content was calculated by the external standard method and the results were expressed as rutin equivalent (mg RE/100 ml) for aqueous extract (decoction). The parameters of the method were as follows: LOQ = 0.25 μg RE/ml; LOD = 0.47 μg RE/ml; RSD = 4.1 %; no systematic error was found [17].

Spectrophotometric measurement of the absorption of total phenolic compounds and total flavonoids was performed with a Lambda 25 spectrophotometer, Perkin-Elmer.

Determination of catechin, epicatechin and rutin by HPLC method

The HPLC system consisted of a Perkin-Elmer (Norwalk CT) Flexar LC pump, Flexar Photo Diode Array Plus detector (PDA), autosampler, thermostat and built-in degasser. Chromatographic data were processed with Chromera HPLC PDA data software, version 4.1.1.6396.

Chromatographic separation of phenolic compounds - catechin, epicatechin and rutin was performed on a Luna C18 column (3 μm , 150 mm \times 4.6 mm, Phenomenex, USA), equipped with a precolumn with the same stationary phase [17]. Elution was performed at a flow rate of 0.9 ml/min at a temperature of 30 °C. Mobile phase: 0.1% formic acid in water (solvent A) and 0.1% formic acid in acetonitrile (solvent B) were used. A program with linear gradient elution was applied as follows: 0-2 min, 15% B; 2-4 min, 20% B; 4-6 min, 25% B; 6-8 min, 30% B; 8-10 min, 35% B; 10-12 min, 35% B; 5 min recalibration of the column by 15% B. The

injection volume of the sample solution and standard solutions was 20 μ l. The following wavelengths were used for detection of catechin, epicatechin and rutin: channel 1 - 275 nm for catechin and epicatechin and channel 2 - 355 nm for rutin, with the reference wavelength set to 620 nm at a fixed bandwidth of 19 nm.

The identification of the chromatographic peaks was performed by comparing the retention times of the eluted peaks and comparing the peak shape in the two channels with different wavelengths (275 and 355 nm). For the quantification of catechin, epicatechin and rutin, the external standard method was used to construct a calibration curve by injecting a series of standard solutions. The parameters of the method were as follows: LOQ (catechin and epicatechin) = 0.40 μ g/ml; LOQ (rutin) = 0.40 μ g/ml; LOD = 0.02 μ g/ml – 0.07 μ g/ml; The repeatability and reproducibility of determination of catechin was – RSD = 4.8 %, of epicatechin – RSD = 3.5 %; of rutin – RSD = 2.3 %. All measurements were performed in triplicate and no systematic error was found [17].

RESULTS AND DISCUSSION

The results for total phenols and total flavonoids content of the studied fruit samples are presented in Table 1. The results are expressed as average value of triplicate analysis, along with confidence interval (CI) estimate at 95% confidence level, calculated with use of t-distribution. The basis of the action of biologically active substances from herbal drugs is the process of solid/liquid extraction with a suitable extraction solvent. Water is often used as an extraction agent due to its unique dissolving properties, which can change with temperature. The preparation of aqueous extracts of medicinal plants at home has a long tradition and is widespread in our country. For this reason, in the present study, water was selected as an extracting agent for the

preparation of various plant decoctions, in compliance with the prescriptions provided by herbal pharmacies. The results show that the content of total phenols exceeds that of total flavonoids in all tested samples with exception of blackthorn, where equal amounts were found. The contents of total phenolic compounds among the fruits decoctions ranged from 2.45 to 167 mg GAE/100 ml. The highest content of total phenols was found in rosehip – 167 mg GAE/100 ml, which is about twice as high as the amount in the second- richest source of total polyphenols – elderberry (83 mg GAE/100 ml). The total flavonoids are highest again in rosehip (85 mg RE/100 ml), followed by elderberry (71 mg GAE/100 ml) and dogwood (12.7 mg/100 ml). The amount of total flavonoids in decoctions of cranberry, hawthorn, blackthorn and black chokeberry is low, ranging between 2.45 - 8.0 mg GAE/100 ml.

The results emphasize that the major sources of total phenols and total flavonoids in traditional teas used in Bulgarian traditional medicine are rosehip and elderberry.

Rosehip (*Rosa canina*) is a species of wild rose. The fruit is characterized by a rich content of vitamin C, carotene, lycopene, pectin, vitamins B₁ and B₂, as well as vitamins PP and K. Usually fresh ripe fruits contain up to 600 mg (per 100 grams of fruit) of vitamin C, according to some sources - up to 2 grams (for certain varieties) [18, 19]. The seeds contain vitamin E as well. Rosehip is often mentioned in traditional folklore and was used in ritual practices with a medicinal focus. The unique combination of vitamin C and other ingredients in rosehip (β -carotene, flavonoids, minerals) stimulates the formation of red blood cells, increases efficiency and strengthens the body's resistance. Therefore, it is recommended for patients with diabetes, anemia, mental and physical fatigue, colds due to its antioxidant polyphenols content as well [19-21].

Table 1. Total phenols and total flavonoids contents in decoctions of Bulgarian medicinal fruits

Latin name	Common name	Total phenols \pm CI*, mg GAE/100 ml	Total flavonoids \pm CI*, mg RE/100 ml
<i>Sambucus nigra</i>	Elderberry	83 \pm 5	71 \pm 5
<i>Vaccinium vitis-idaea</i>	Cranberry	5.4 \pm 0.2	3.9 \pm 0.2
<i>Crataegus monogyna</i>	Hawthorn	36 \pm 2	8.0 \pm 0.7
<i>Rosa canina</i>	Rosehip	167 \pm 12	86 \pm 7.44
<i>Cornus mas</i>	Dogwood	44 \pm 2	12.7 \pm 1.7
<i>Prunus spinosa</i>	Blackthorn	2.45 \pm 0.2	2.45 \pm 0.25
<i>Aronia melanocarpa</i>	Black chokeberry	35 \pm 2	3.25 \pm 0.12

*CI – confidence interval at 95% confidence level.

Elderberry (*Sambucus nigra*) contains useful micronutrients including iron, potassium, phosphorus, copper, as well as vitamins A, B and C, organic compounds with anti-inflammatory and antioxidant activity [19-21]. Both the flowers and the fruits of the black elderberry are important for pharmaceutical practice. They are applied in the form of teas, juices, extracts and syrups. Fruits have a strong healing effect, whose pronounced antioxidant activity is due to their high polyphenols content, namely anthocyanins and flavonols. Our results emphasize the high level of polyphenols in rosehip and elderberry, supporting their phytotherapeutic use as natural antioxidant sources.

The HPLC separation of catechin, epicatechin and rutin of standard solution and elderberry decoction is presented in Figures 1 and 2. The results of the HPLC method show that the elution of catechin, epicatechin and rutin takes place within 11 minutes. The identification of the chromatographic peaks was performed by comparing the retention times of the eluted peaks and comparing the peak shapes in detection at two different wavelengths (275 nm and 355 nm). The chromatograms given in Figures 1 and 2 show a very good baseline separation of the analytes. The use of formic acid in the mobile phase suppresses the strong specific interactions between the sorbent (residual silicol groups) and the sorbate (phenolic groups in the analyte) caused by orientational interactions between molecules with constant

dipoles. In the present study, detection with a PDA photodiode detector was used, the analytical signal being measured at the wavelength of the highest sensitivity as follows - 275 nm for catechin and epicatechin, and 355 nm for rutin. Our results show that the HPLC method has a very good sensitivity and, correspondingly, a low limit of quantification (LOQ). The values of the limit of detection (LOD) and the limit of quantification (LOQ) were determined from the signal-to-noise ratio S/N, using a progressively lower concentration of analytes for the ratio S/N - 3 for LOD and 10 for LOQ. The limits of quantification were determined as follows: 0.40 µg/ml for catechin and epicatechin (275 nm) and 0.07 µg/ml for rutin (355 nm) [17].

The results for catechin, epicatechin and rutin contents of decoctions from the medicinal fruits are presented in Table 2. The results are expressed as mean values of triplicate analysis in µg/100 ml, along with their confidence intervals.

The present results show for the first time original analytical data not only for the integral parameters for polyphenols contents such as total phenols and total flavonoids, but for individual flavonoids as well, obtained by HPLC analysis. It could be noted that in contrast to the results obtained by spectrophotometric methods, the HPLC analysis shows presence of catechin, epicatechin or rutin in aqueous decoctions only in 3 out of 7 samples studied.

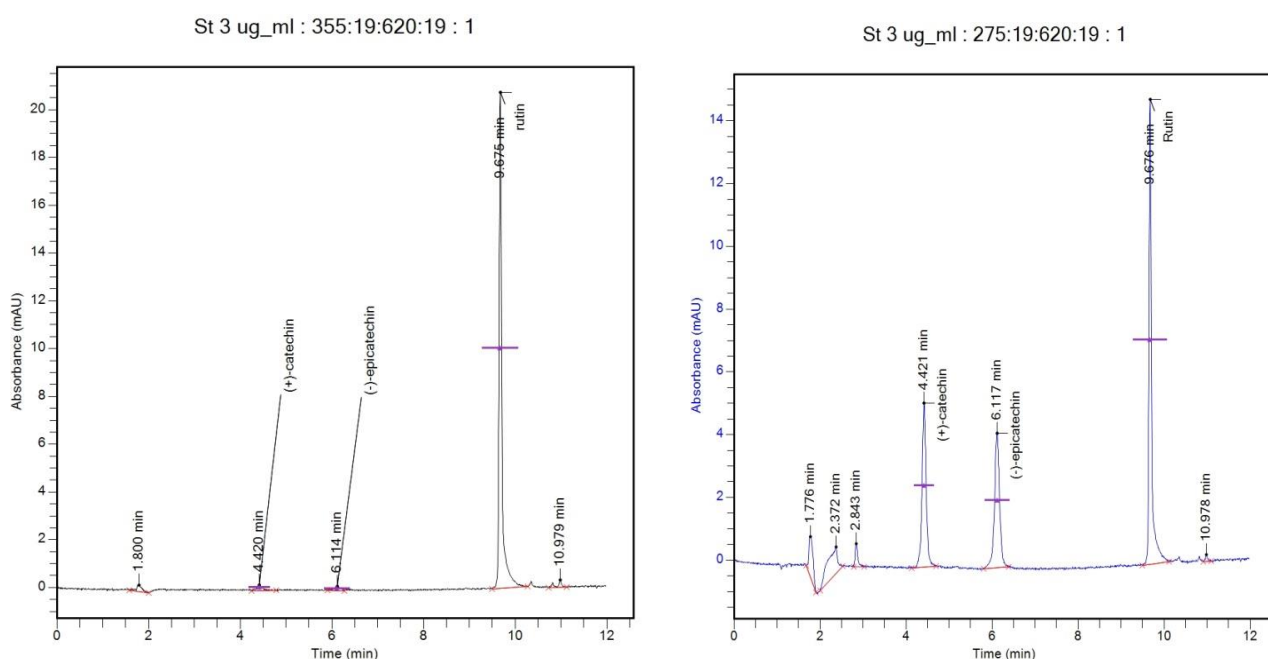


Figure 1. Chromatograms of a standard solution of catechin, epicatechin and rutin at 355 nm and 275 nm.

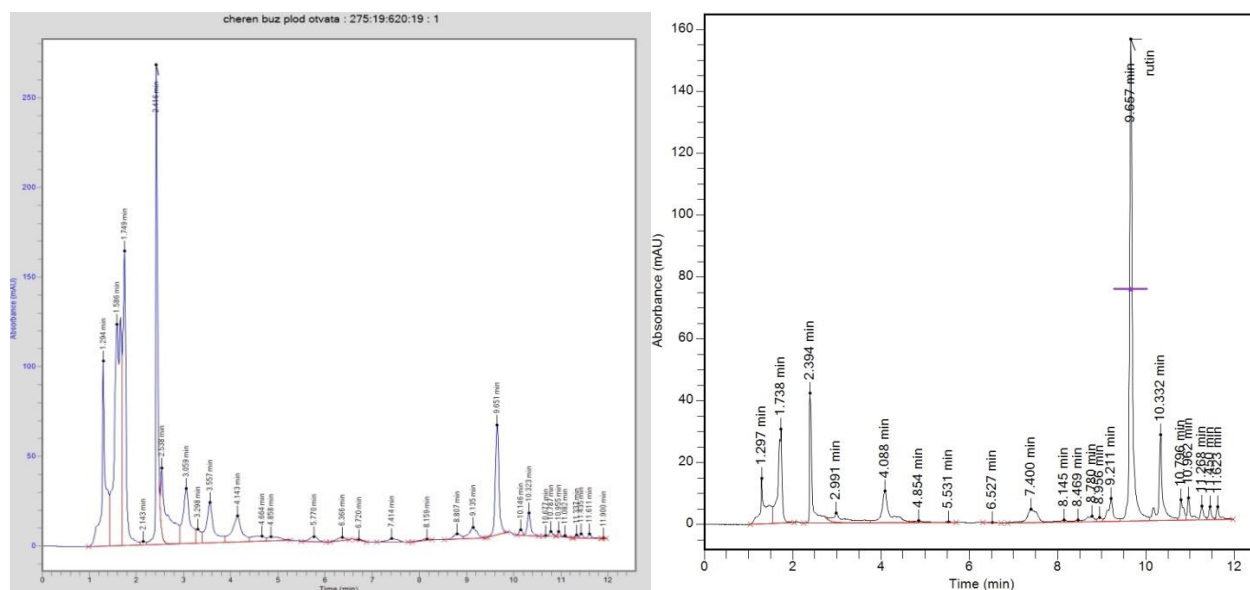


Figure 2. Chromatograms of catechin, epicatechin and rutin in elderberry fruits decoction at 275 nm and 355 nm.

Table 2. Catechin, epicatechin and rutin content in decoctions of Bulgarian medicinal fruits

Latin name	Common name	Catechin \pm CI*	Epicatechin \pm CI*	Rutin \pm CI*
		$\mu\text{g}/100 \text{ ml}$	$\mu\text{g}/100 \text{ ml}$	$\mu\text{g}/100 \text{ ml}$
<i>Sambucus nigra</i>	Elderberry	<LOD	<LOD	10700 \pm 695
<i>Vaccinium vitis-ideae</i>	Cranberry	<LOD	<LOD	<LOD
<i>Crataegus monogyna</i>	Hawthorn	<LOD	153 \pm 7	174 \pm 15
<i>Rosa canina</i>	Rosehip	<LOD	<LOD	<LOD
<i>Cornus mas</i>	Dogwood	<LOD	<LOD	<LOD
<i>Prunus spinosa</i>	Blackthorn	<LOD	<LOD	<LOD
<i>Aronia melanocarpa</i>	Black chokeberry	448 \pm 12	<LOD	80 \pm 2

*CI – confidence interval at 95% confidence level.

Catechin is found only in black chokeberry decoctions, and epicatechin only in hawthorn. With the exception of black elderberries, in other fruit samples the level of rutin is low or undetectable (cranberry, rosehip, dogwood, and blackthorn). In black chokeberry and hawthorn decoctions, the rutin content is 80 and 174 $\mu\text{g}/100 \text{ ml}$, respectively. A comparison of these results with literature data and our previous studies shows that aqueous decoctions are not the most efficient extraction solvent for flavonoids compared to extraction systems with higher lipophilicity such as methanol/water [22]. For example, when 80% methanol/water solvent was applied, rutin was found in all tested fruits, and catechin in samples of elderberry and cranberry, and epicatechin in cranberry as well [23]. However, the present study aims to determine the values of the polyphenols in aqueous formulations according to the instruction of preparation and designed for direct consumption. We could note that the amount of rutin in black elderberry decoctions is extremely high and

reaches 10.7 mg/100 ml. This is reflected in the widespread home-made formulas of syrups, infusions and others made from *Sambucus nigra* fruits in recent years.

CONCLUSION

In the present study seven traditional for Bulgarian folk medicine fruits were studied for their polyphenols content. The results show that decoctions of rosehip have higher contents of total phenols and total flavonoids but no catechin, epicatechin or rutin. The highest amount of rutin was detected in elderberry along with very high content of total phenols and total flavonoids, suggesting the promotion of *Sambucus nigra* to be used in antioxidant phytochemical formulations.

REFERENCES

1. A. N. Tashev, E. I. Tsavkov, *Phytol. Balc.*, **14**(2), 275 (2008).

2. E. Birben, U. M. Sahiner, C. Sackesen, S. Erzurum, O. Kalaycin, *World Allergy Organ. J.*, **5**(1), 9 (2012). DOI:10.1097/WOX.0b013e3182439613.
3. E. B. Kururtas, *Nutr. J.*, **15**, 71 (2016). DOI 10.1186/s12937-016-0186-5
4. J. A. Thomas, in: *Modern Nutrition in Health and Disease*, 8th edn., Lea & Febiger, Philadelphia, 1994, p. 501.
5. D. Ivanova, D. Gerova, T. Chervenkov, T. Yankova. *J. Ethnopharmacol.*, **96**(1-2), 145 (2005).
6. K. M. Yoo, I. K. Hwang, B. Moon, *J. Food Sci.*, **74**(6), C419 (2009).
7. S. Kumar, A. K. Pandey, *Sci. World J.*, **2013**, 29 (2013). DOI: 10.1155/2013/162750.
8. N. C. Veitch, R. J. Grayer, *Nat. Prod. Rep.*, **20**(10), 1625 (2011).
9. D. Ravishankar, A. K. Rajora, F. Greco, H. Osorn, *Int. J. Biochem. Cell Biol.*, **45**(12), 2821 (2013).
10. S. Rautiainen, S. Larsson, J. Virtamo, A. Wolk, *Stroke*. **43**(2), 335 (2012).
11. A. Perez, S. G. Munzano, R. Jimenez, R. Perez-Abdul, J. M. Haro, A. Osuna, C. Santos-Buelga, J. Duarte, F. Perez-Vizcanio, *The Pharmacol. Res.*, **89**, 11 (2014).
12. E. Nicolle, F. Souard, P. Faure, A. Boumendjel, *Curr. Med. Chem.*, **18**(17), 2661 (2011).
13. M. G. L. Hertog, E. J. M. Fekens, P. C. H. Hollman, M. B. Katan, D. Kromhout, *Nutr. Cancer*, **22**(2), 175 (1994).
14. A. Gurib-Facum, *Mol. Aspects Med.*, **24**, 1 (2006).
15. C. Veeresham, *J. Adv. Pharm. Technol. Res.*, **3**(4), 200 (2012).
16. D. Marinov, F. Ribarova, M. Atanasova, *J. Univ. Chem. Technol. Metall.*, **40**(3), 255 (2005).
17. P. Koleva, S. Tsanova-Savova, S. Paneva, S. Velikov, Z. Savova, *Pharmacia*, **68**(4), 819 (2021).
18. P. Dimkov, *Bulgarian folk medicine*, vol. 1, Bulg. Acad. Sci. Publ., Sofia, 1979 (in Bulgarian).
19. S. Nikolov, *Special encyclopedia of medicinal plants in Bulgaria*, Trud Publ., Sofia, 2010 (in Bulgarian).
20. D. Staneva, D. Panova, L. Rainova, I. Asenov, *Herbs in every home*, Medicina i fizkultura Publ., Sofia, 1986, p. 337 (in Bulgarian).
21. I. Landzhev, *Encyclopedia of medicinal plants in Bulgaria*, Trud Publ., Sofia, 2010 (in Bulgarian).
22. S. Tsanova-Savova, F. Ribarova, M. Gerova, *J. Food Compos. Anal.*, **18**, 691 (2005).
23. S. Tsanova-Savova, S. Velikov, S. Paneva, P. Koleva, P. Nikolchova, D. Etugov, Z. Savova, *Acta Med. Bulg.*, **49**(1), 26 (2022).

Experimental investigation of the effect of nanomaterial reinforcement on the mechanical properties of rubber structures used in crank pulleys

K. Gündoğan*, M. Gitmiş

Department of Material Science and Nanotechnology Engineering, Faculty of Engineering, University of Uşak, Uşak, Turkey

Received: April 19, 2022; Revised: September 27, 2022

Automotive technology is constantly evolving with the desire to make engines light and to reach strong torques. The viscoelastic rubber material is seen as the most damaged material in crank pulleys structure used to dampen torsional vibrations. For this reason, the manufacturers' efforts to increase this structure's strength without departing from the design parameters of the rubber material are continuing today. In this study, nanosized alumina and zeolite reinforcements were introduced into natural and EPDM rubbers, which are non-linear materials, using spraying and homogeneous mixing methods. Tensile tests were carried out on reinforced and non-reinforced rubber samples. A graph was created with torque data corresponding to four different samples. The torsional stiffness was found from the slope of the graph. Experimental modal analysis results using a hammer were compared with torsional stiffness. A deviation close to 10% was observed between these two methods. Motor simulation and noise tests were performed on the sample pulleys and it was found that the most suitable pulley is the nanozeolite-reinforced crank pulley with the homogeneous mixing method (HMM).

Keywords: Rubber, nanoalumina, nanozeolite, torsional vibration damper, vibration, noise.

INTRODUCTION

Crank pulleys are front parts of the engine that are attached to the crankshaft on the engine assembly. The movement from the crank is integrated with the other pulleys (alternator, air conditioner, water pump, oil pump, idler) on the engine with the help of the v-belt.

Crankshafts are subjected to torsional vibrations in a regular regime. The tensile strengths and fatigue strengths in critical regions of the crankshaft must be determined precisely by modern calculation methods for these vibrations. Today, due to technical, commercial, and environmental requirements, internal combustion engines must operate with high cylinder pressures, and components must be optimized for best performance. Therefore, the crank pulley plays an important role.

Elements that make up the crank pulley are:

1. *Pulley:* It is responsible for moving the engine elements such as the water pump, alternator, and air conditioner through the Poly V belt with the movement taken from the crank.

2. *Hub:* This is where the crank pulley is mounted on the crankshaft. A crank speed and position sensor is connected between the crankshaft and the hub joint. This sensor is responsible for

reporting the angular position of the crankshaft and the engine speed to the ECU.

3. *Vibration rubber:* It is responsible for damping torsional vibration amplitudes.

Ramzan *et al.*, in their study, obtained a material whose elastomers are composite with nanomaterials. The damping capabilities of natural rubber by adding nanoparticles into it were investigated, and as a result, design parameters in different variations were determined [1]. In another study, Ramzan and Kumar prepared a test setup and demonstrated that this test method increased the damping ability of nanomaterials [2].

Ziraki *et al.* added silica nanoparticles and polypropylene fibers to the silicone rubber matrix. The viscoelastic behavior and mechanical properties of the samples of this nanoparticle reinforced rubber were investigated. The results proved that silica particles increase the elastic modulus of rubber and impart high hardness [3].

Huang and Tsai characterized the vibration damping response of composite layers containing silica nanoparticles and rubber particles. The experimental results were compared with the finite element method. From these results it was concluded that the bending stiffness of fiber composites decreased, and the damping properties of the layers improved, especially for (90/10) layers [4].

* To whom all correspondence should be sent:
E-mail: kadir.gundogan@usak.edu.tr

Muhammad *et al.* have designed a new nanocomposite vibration damper. They used NR and alumina zirconium as test samples. In addition, they made a comparison with the analytical and finite element method with the modal analysis [5].

Nagar *et al.* designed a damper for a multi-cylinder engine and compared two different rubbers such as EPDM and AEM, and found that it provides better damping, oil resistance, and durability. The currently produced EPDM rubber sample has proven that it absorbs torsional vibrations better by 50% at critical speeds in a multi-cylinder diesel engine by measuring torsional vibrations in the engine test device and then subjecting it to the same tests on AEM rubber [6].

Qiu *et al.* have prepared a series of maleic anhydride-grafted ethylene-propylene-diene rubbers (EPDM-g-MAHs) with different inoculation grades by rotary evaporation assisted melt grafting, which can achieve a higher inoculation rate and smaller gel content. Morphological observation, thermal analysis, and rheological measurements confirmed that the interfacial compatibility of core-shell dispersed phases is enhanced by increasing the inoculation degree. In this study, a new understanding of the hardening mechanism of core-shell particles was presented [7].

Enew *et al.* investigated the effect of aramid fiber in the form of vlar (KP), carbon mono fiber (CMF), and nanocarbon black (NCB) pulp as filler for Trilene liquid polymers on the mechanical properties of the EPDM rubber. They found that EPDM rubber improved its mechanical properties such as thermal insulation, tensile strength, elongation, and hardness [8].

Ravindran *et al.* investigated the mechanical properties and solvent absorption properties of the nanocomposites they produced by TEM analysis. They found 243% as the maximum increase in tensile strength of nanocomposites. The value and percent elongation of the pure mixture increased by 67%. They observed significant differences in mechanical and absorption properties as the filler content changed [9].

Fig. 1 shows the failure of the damping ability of the crankshaft to resonate and its rupture from the elastomer area. In this case, nanoparticle reinforcement improves the mechanical properties of the elastomer part and increases the damping ability, thus eliminating these problems.

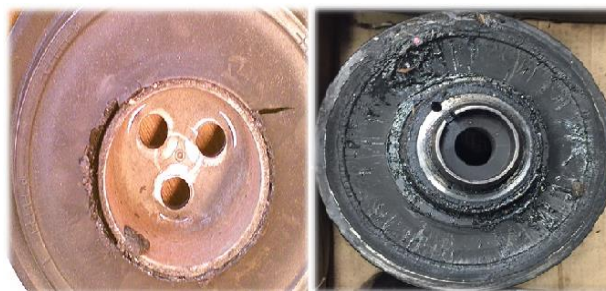


Fig. 1. Defects in the crank pulley

MATERIAL AND METHODS

Nanoalumina (0.5%) and nanozeolite (1.1%) reinforcement particles were added to NR and EPDM rubbers as matrix elements of the test samples using homogeneous mixing (HM) and spraying method. Sample crank pulleys were vulcanized in a hot press at 150 °C for 15 minutes. For the uniaxial tensile test, samples conforming to ASTM D412 – C standards were cured at the same temperature and time.

In the homogeneous mixing method, the raw materials in Table 1 were mixed. A 100% pure polymer NR and EPDM rubber was used. Nanoalumina 0.5% and nanozeolite 1.1% were reinforced in the mixture. Carbon black was used to increase the hardness of the sample and other raw materials to increase the efficient workability of the mixture. It was applied to natural rubber and EPDM rubber by spraying alumina and zeolite particles on rubber with a spray gun at 3 – 4 bar air pressure. In this method, a special solution (methyl ethyl ketone + nanomaterial) was made and absorbed into the rubber. A physical mixture was provided with 40 mg of nanomaterial and 20 ccs of MEK into the mixture.

According to Hooke's law, both tensile and compressive behaviors of metals show the same properties in the elastic region. Features such as Poisson's ratio and modulus of elasticity can be found easily. However, the same statements are not true for elastic materials such as rubber [10]. Due to the different behavior of rubber in the tensile and compression regions, it is insufficient to determine only the mechanical properties. Due to the accumulation of knowledge on this subject, standards such as ASTM D412, DIN 53 504, and ISO 37 have emerged [11-13].

Test samples were made according to ASTM D412 – C sample and subjected to the uniaxial tensile test under a constant load of 45 kN without preload. (LLOYD LR50KPlus).

Table 1. Ratios of nanoalumina and nanozeolite-reinforced rubbers produced by HMM

Raw Materials	%	phr	Raw Materials	%	phr
NR Rubber/ EPDM Rubber	100	51.7	NR Rubber/ EPDM Rubber	100	33.82
Nanoalumina	0.5	0.25	Nanozeolite	1.1	0.37
N330	76	39.29	N550	120	40.5
Oil	4	2.06	Oil	45	15.22
Other	14.6	7.53	Other	29.5	9.95
Total	193.39	100	Total	295.6	100

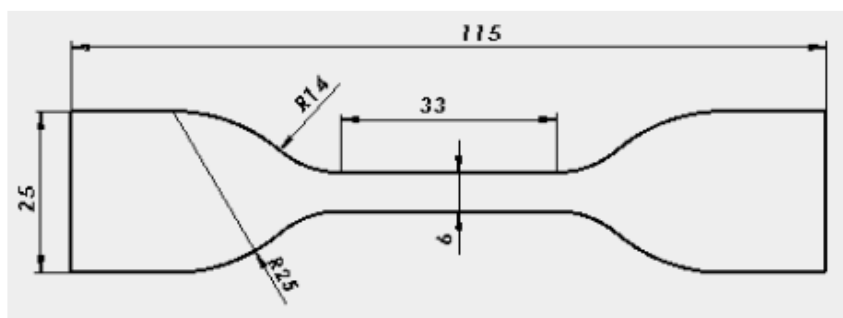


Fig. 2. ASTM D412 – C sample type

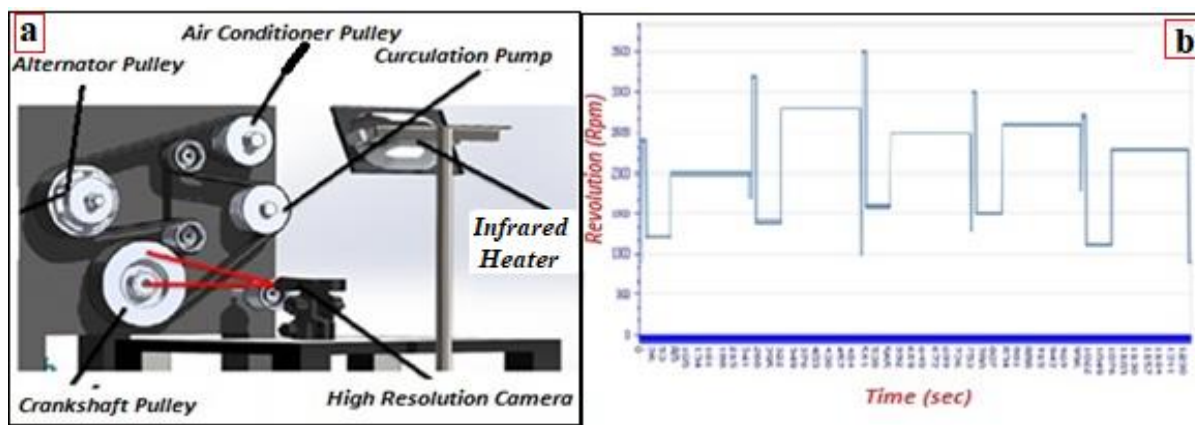


Fig. 3. Engine simulation test setup (a) and cycle-time graph (b).

Elastomer materials such as rubber have similar characteristic properties as a metal spring and a viscous liquid. This visco-elastic behavior is defined as deformation and energy-absorbing. Rubber consists of an infinite number of patterns with a wide spectrum of spring constants and viscosities. Torsional stiffness test specimens were made in the DEVOTRANS Torque Life Test device at room temperature, providing angles of $1^\circ - 30^\circ$.

Many researchers have developed test methods for natural frequency and vibration measurements. For crank pulleys, the natural frequency of torsion is an important design parameter. Natural frequency measurements are generally performed with the hammer method because it is cheap and easy. The vibration frequency distribution of the force is found in the hammer test in the modal test setup [14]. For the natural frequency test, the frequency values and amplitudes of the pulley were measured by

performing FFT (Fast Fourier Transform) analysis with the DEWESoft Sirius program for the vibrations against the force coming from the accelerometer, which was attached to the damper on the test samples, and the hammer.

Vibration data were found in terms of mm/s by applying a radial load of 700 N. Torsional vibration data were obtained using a sampling time of 1 second at a constant temperature of 90°C in the test setup given in Fig. 3 (a) and variable revolutions between 900 rpm and 3000 rpm given in Fig. 3 (b).

RESULTS AND DISCUSSION

Tensile test result graphs of sample rubbers extracted in ASTM D412 – C dimensions are given in Fig. 4. Maximum strengths were examined by giving the graphs in Load (N) – Time (seconds).

The maximum torsional strength of 30° (0.6 rad) of the sample pulley, which is produced with

nanoalumina-reinforced NR rubber (a) angle-torque graph, produced by the spraying method given in Fig. 5, was found to be 290.172 Nm, and the torsional stiffness from the inclination was found to be 561.37 Nm/rad. In the angle-torque graph (b) of

nanozeolite-reinforced NR rubber produced by the spraying method, the torsional stiffness is 584.55 Nm/rad.

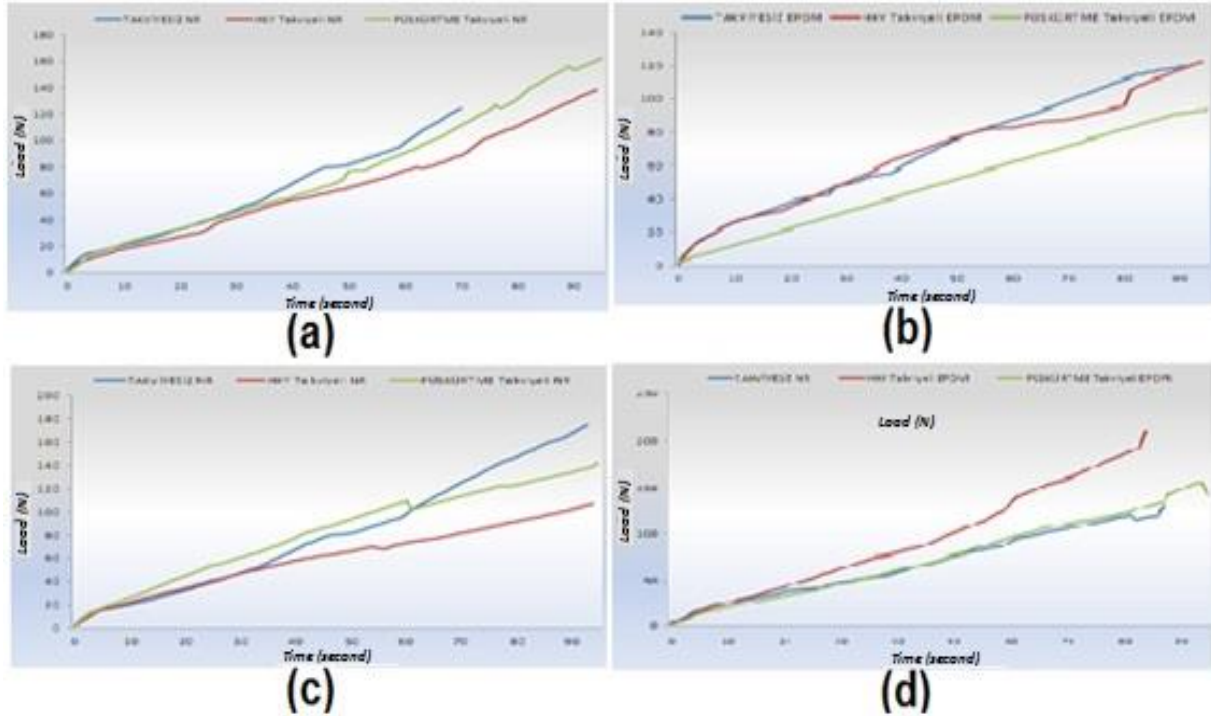


Fig. 4. Uniaxial tensile test results of sample rubbers

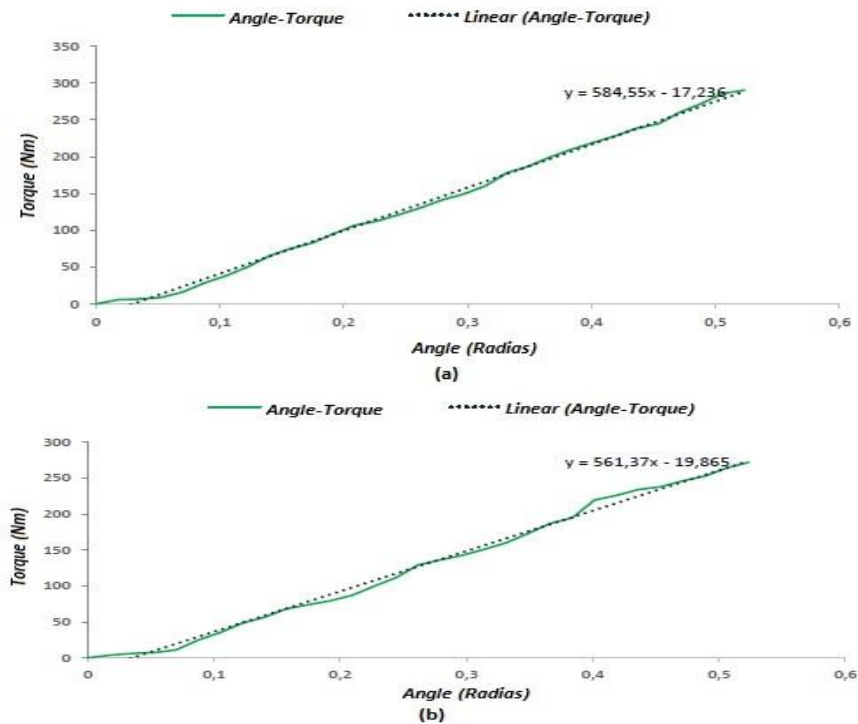


Fig. 5. Angle-torque graph of a) nanoalumina-reinforced b) nanozeolite-reinforced NR rubber crank pulley by spraying method

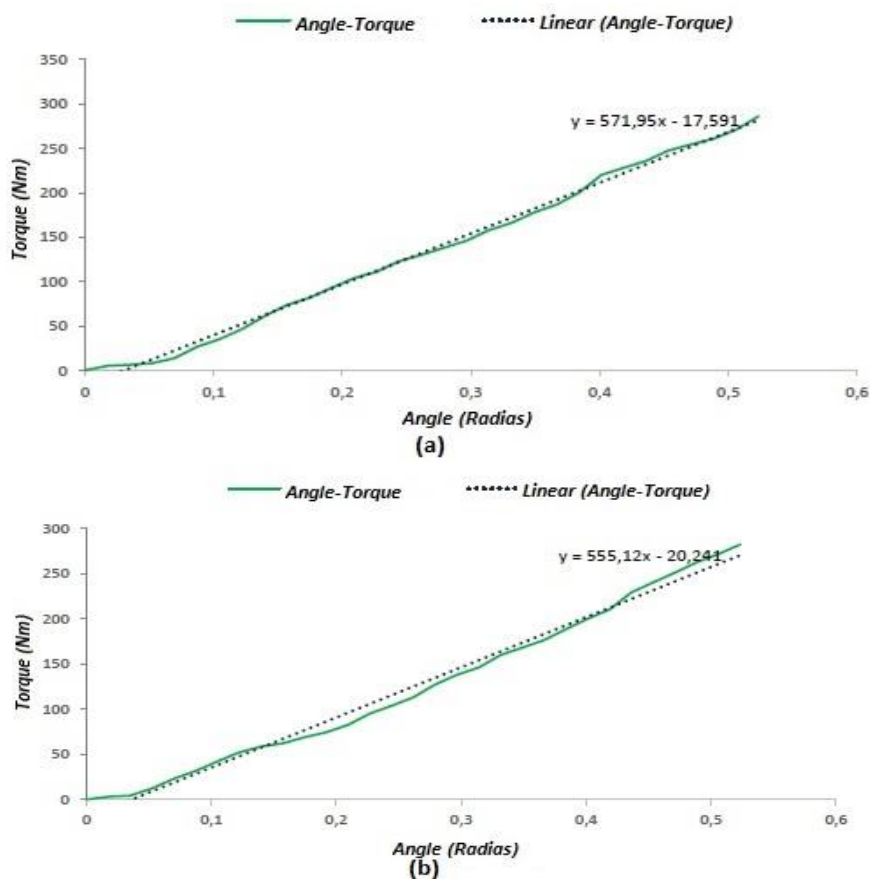


Fig. 6. HMM of EPDM rubber a) reinforced with nanozeolite and b) reinforced with nanoalumina by spraying method. Angle-torque graph of the crank pulley

Table 2. Hardness values and % changes of sample rubbers

Sample Type	Hardness (Shore A)	
Non-reinforced NR	54	
NR + Nanoalumina	<i>Homogeneous</i>	51
	<i>Mixing</i>	54
	<i>Spraying</i>	54
NR + Nanozeolite	<i>Homogeneous</i>	62
	<i>Mixing</i>	65
Non-reinforced EPDM		54
	<i>Homogeneous</i>	51
	<i>Mixing</i>	54
EPDM + Nanoalumina	<i>Spraying</i>	54
	<i>Homogeneous</i>	62
EPDM + Nanozeolite	<i>Mixing</i>	65
	<i>Spraying</i>	65

The torsional stiffness (a) of the crank pulley sample with nanozeolite-reinforced EPDM rubber produced by HMM is shown in Fig. 6 as 1000.05 Nm/rad. The maximum torsion of the crank pulley is 282.097 Nm. Again, the maximum torsion of the nanoalumina-reinforced EPDM rubber pulley (b) produced by the spraying method given in Fig. 6 is

286.01 Nm, while the torsional stiffness is 900.12 Nm/rad.

The changes in the hardness value of nanomaterial reinforcements to NR rubber and EPDM rubber are given in Table 2. As can be seen in the table, the hardness of NR rubber decreased when it was produced with HMM in nanoalumina reinforcement. In nanozeolite reinforcement, a direct effect on the hardness of NR rubber is seen, especially in the spraying method, with an effect of 16.09%. To examine the effect of hardness on torsional stiffness, torsional stiffness graphs of nanoalumina- and nanozeolite-reinforced NR rubber, zeolite-reinforced EPDM rubber produced with HMM, and alumina-reinforced EPDM rubber produced by spraying method were obtained for the samples.

In the experimental modal analysis test performed on the sample pulleys, natural frequencies were found using a hammer. These values are based on the peak of the pulley, and the frequency amplitudes of the crankshaft and pulleys are given in Fig. 7.

While the natural frequency value for nanoalumina-reinforced NR by spraying method was 333.5 Hz, it was 339.4 Hz for nanozeolite-

reinforced NR. Although EPDM reinforced with nanoalumina by spraying method was in the maximum frequency range of 465.8 Hz, the closest natural frequency result to the crankshaft with 418.9 Hz was nanozeolite reinforcement with HMM.

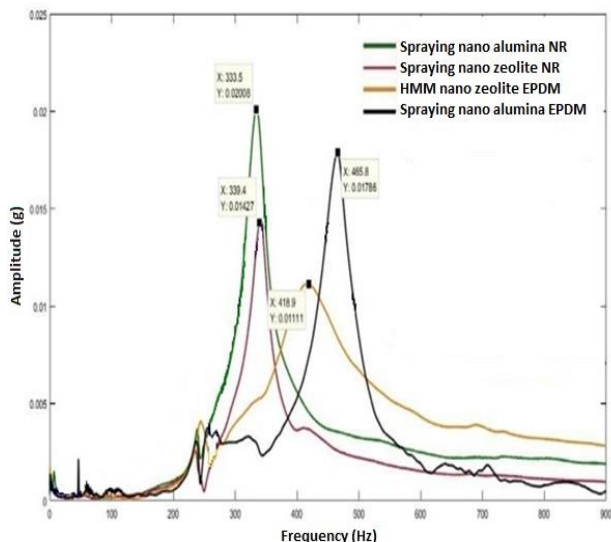


Fig. 7. Natural frequency test results of sample pulleys

In this case, the results from the torsional stiffness and the natural frequency results comparison are given in Table 3. As seen in the table, the analytical modal analysis and experimental modal analysis error rates resulting from torsional stiffness are around 10%. The closest result was for the crank pulley with nanozeolite reinforced EPDM rubber produced with HMM. Engine simulation tests on sample pulleys performed at a constant temperature with the cycles given in Fig. 3(b) are given in Fig. 8 below.

According to the engine simulation test results, the most vibrating pulley was the nanozeolite-reinforced NR rubber pulley produced with the spraying method, while the least vibrating pulley

was the nanozeolite-reinforced EPDM rubber pulley produced with HMM.

Acoustic control tests were carried out on the crank pulleys at certain speeds with the help of a microphone. These test results are shown in Fig. 9, and the sound intensities of the pulleys are given in dB (A).

According to the test results given in Fig. 9, the same results were obtained as the vibration data. The crank pulley that made the most noise was the nanoalumina-reinforced NR rubber produced by the spraying method, while the nanozeolite-reinforced EPDM rubber crank pulley produced with HMM made the least noise.

CONCLUSION

Crank pulleys are some of the front parts of the engine that absorb the torsional vibrations coming from the crankshaft and transmit the movement from the crank to other parts. Light and powerful engine technology is constantly developing, and the importance of the type of material used is growing day by day. Especially the field of nanotechnology shows continuous development.

In this study, a nanocomposite material was formed by adding nanoalumina and nanozeolite to natural and EPDM rubber, which is a non-linear material used in crank pulleys, using homogeneous and spraying methods. Nanocomposite specimens were subjected to a uniaxial tensile test, and a positive effect on tensile strength and elongation was observed in the homogeneous mixing method of nanoalumina reinforcement of natural rubber. It was found that zeolite supplementation has negative results in both production methods. It was observed, however, that the zeolite reinforcement made to EPDM rubber increased the breaking strength by 61% compared to the unreinforced rubber.

Table 3. Analytical and experimental modal analysis % error rates of sample pulleys

Rubber Type	Reinforcement Material	Mixing Method	Analytical Modal Analysis (Hz)	Experimental Modal Analysis (Hz)	% Error
NR	Nanoalumina	Spraying	307.74	339.4	9.33%
	Nanozeolite	Spraying	301.58	333.5	9.57%
EPDM	Nanoalumina	Spraying	402.52	465.8	13.59%
	Nanozeolite	Homogeneous Mixing	381.88	418.9	8.84%

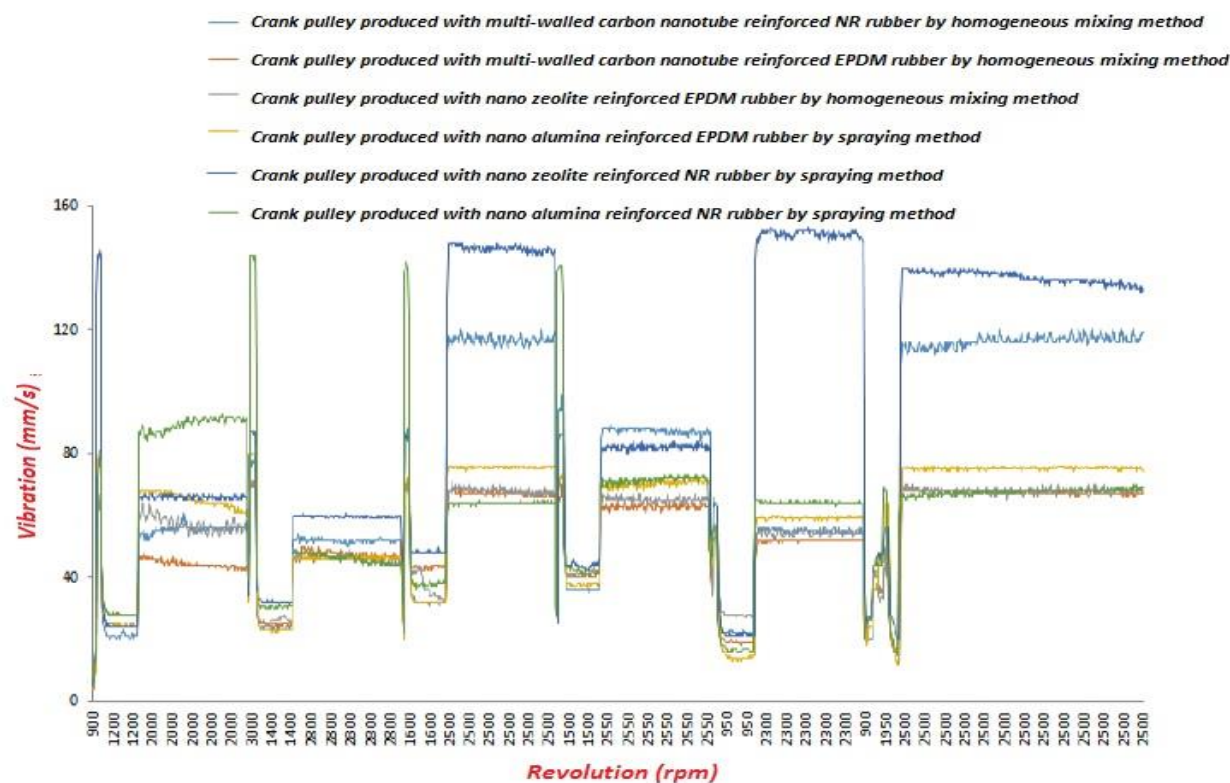


Fig. 8. Speed – vibration test results of sample pulleys

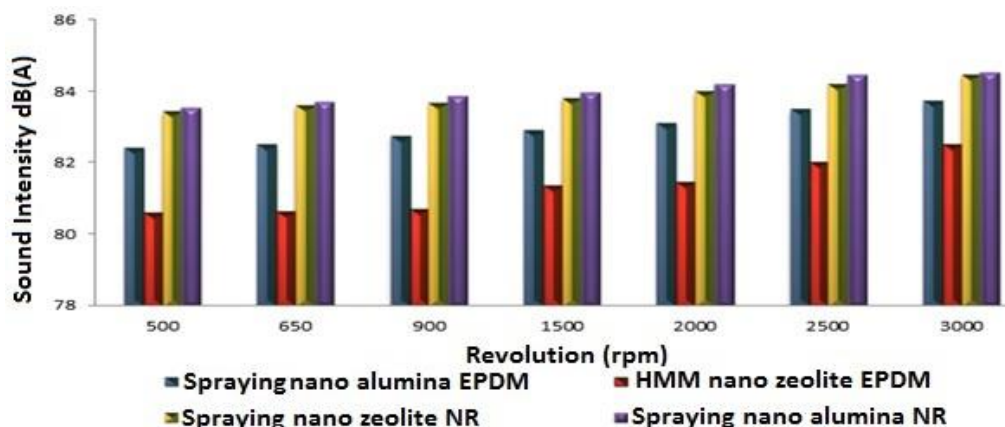


Fig. 9. Sound intensities of sample pulleys

It was found that the nanoalumina reinforcement of NR rubber did not change the hardness value, while the nanozeolite reinforcement increased the hardness. Especially in the spraying method, it was observed that the hardness changes at a rate of 16%. When the effect of the hardness value on the torsional stiffness was examined, it was found that the hard material had a lower torsional stiffness. Since the ratio of torsional stiffness and inertial mass gives the square of the natural frequency, it is compared with the modal analysis results.

Modal analysis was performed using the hammer method, and the natural frequency of the sample pulleys and crankshaft was found. In this

experiment, it was seen that the nanozeolite-reinforced EPDM rubber crank pulley produced with HMM has the closest resonance frequency to the crankshaft. This situation is interpreted as a contribution to the durability of the crankshaft as the pulley is at the same resonance frequency without the shaft resonating during the torsional vibrations coming from the crankshaft. In the natural frequency results calculated by the analytical method and found by the experimental method, it was found that the results of the HMM and nanozeolite-reinforced EPDM rubber pulley with an error rate of 8.84% approach the experimental results, therefore the

natural frequency can be found from the torsional stiffness and torsional inertia mass.

As regards the vibration and noise data, it was concluded that the noise intensity of the pulley that vibrates the most is higher than that of the other samples. Due to this situation, it was determined that a correlation can be established with the acoustic control test instead of the engine simulation test in terms of time and cost. As it is known that the noise levels of the crank pulleys will be at the engine idling speed (900 rpm), it was seen that the crank pulley with nanozeolite-reinforced EPDM rubber produced with HMM had the least noise level of 80.07 dB (A). In the light of these data, it was found by the test results that the nanozeolite-reinforced EPDM rubber crank pulley produced with HMM, taking into account the parameters that dampen the vibrations coming from the crankshaft and the rubber structure, shows the best strength.

Acknowledgement: We thank the Uşak University BAP Commission for the project support on "Experimental and Finite Element Method Experimental Investigation of the Mechanical Behaviors of the Elastomer Structure Used to Dampen Vibrations Affecting the Crank Pulley, by Improving it with Nano-Materials".

REFERENCES

1. M. Ramzan, A. Abdurraheman, B. Kumar, *International Journal of Innovative Research in Science, Engineering and Technology*, **6**, 1 (2017).
2. M. Ramzan, B. Kumar, *Int. Journal of Innovations in Mechanical & Automobile Engineering*, ISSN: 2249-2968, **2** (1), 53 (2011).
3. S. Ziraki, S. M. Zebarjad, M. J. Hadianfard, *Polymer-Plastics Technology and Engineering*, **55**(16), 1693 (2016).
4. C. Y. Huang, J. L. Tsai, *SAGE*, **49** (5), 545 (2015).
5. M. Ramzan, B. Kumar, A. Chaskar, *Journal of Mechanical and Civil Engineering (IOSR-JMCE)*, **11** (3), 45 (2014).
6. A. Nagar, V. Chokkalingam, N. Umashankar, S. R. Shankar, *SAE Technical Paper*, **1**, 2777 (2013).
7. B. Qiuab, P. Qia, Z. Qiana, W. Fanga, H. Zoua, Huang, *Composites, Part C: Open Access*, **3**, 100065 (2020).
8. A. M. Enew, M. A. Elfattah, S. R. Fouda, S. A. Hawasha, *Polymer Testing*, **103**, 107341 (2021).
9. A. Ravindran, M. Kamaraj, N. Vasanthmurali, V. Meghavarshini, M. Balachandran, *Materials Today Proceedings*, **46** (10), 4381 (2021).
10. V. Vahapoğlu, Doctoral Thesis, Karadeniz Technical University, Graduate School of Natural and Applied Science, Trabzon, 2006.
11. ASTM D 412, Standard Test Method for Vulcanization Rubber and Thermoplastic Rubber and Thermoplastic Elastomer – Tension, ASTM, Philadelphia, 1992.
12. DIN 53 504, Bestimmung von Reißfestigkeit, Zugfestigkeit, Reißdehnung und Spannungswerten im Zugversuch, D.I.N.
13. ISO 37:205, Rubber, Vulcanized or Thermoplastic. Determination of Tensile Stress-Strain Properties, International Organization for Standardization, Geneva, 2005.
14. B. J. Schwarz, M. H. Richardson, CSI Reliability Week, Orlando, FL, 1, 1993.

Design, preparation and antibacterial activity of light-activated polymer coatings

N. Philipova¹, D. Ganchev², I. Lalov³, R. Bryaskova^{1*}

¹Department of Polymer Engineering, University of Chemical Technology and Metallurgy, Sofia, Bulgaria

²Department of Machine Elements and Non-Metal Constructions, Technical University, Sofia, Bulgaria

³Department of Biotechnology, University of Chemical Technology and Metallurgy, Sofia, Bulgaria

Received: September 14, 2022; Revised: November 23, 2022

Here, we report on the preparation of light-activated polymer coatings obtained *via* a simple dip-coating procedure on a stainless steel (SS) substrate by using the following components: 1) P(mDOPA)-co-P(DMAEMA⁺) polycationic copolymer; 2) Pox(mDOPA)/PAH nanogel which possesses quinone groups and 3) a photosensitizing agent on the base of porphyrin IX (PPIX - ED). Energy dispersive X-ray analysis with SEM (EDX-SEM) was used to analyse the chemical composition and distribution of elements of the coatings. The antibacterial activity against *G. negative E. coli* and *G. positive B. subtilis* was established by a modified disc diffusion method.

Keywords: light-activated coatings; photosensitizers; antibacterial activity

INTRODUCTION

Several research groups, as well as healthcare industry are oriented toward the design and preparation of effective and long-lasting antibacterial coatings. This is a requirement to prevent the initial bacterial attachment to different surfaces in the hospital, which are responsible for a number of nosocomial infections. The common methods for disinfection in the practice include physical or chemical disinfection treatment [1, 2]. However, these procedures are not effective enough and recontamination of the surfaces occurs very rapidly. Therefore, other more effective technologies have been developed in order to prevent the spread of infections. Most of them are based on the release of active biocidal agents from the coating as silver, copper, or zinc, which are able to kill microorganisms on the top of the coated surfaces [3, 4]. The anti-adhesive coatings are other antibacterial products which reduce bacterial attachment to surfaces [5]. Among them, super-hydrophobic surfaces attract interest since they may delay or even prevent microbial attachment to a surface [6, 7]. The other technology includes the preparation of contact-active surfaces that exhibit antimicrobial activity without releasing biocidal substances [8]. Presently, attention is paid to so-called light-activated surfaces. They require special molecules known as photosensitizers, which absorb light in the visible part of the spectrum and transfer the absorbed energy *via* its triplet state to adjacent molecules, in particular, molecular oxygen, thus leading to the generation of reactive oxygen species (ROS) [9]. Two types of antimicrobial coatings can produce

reactive oxygen species: i) a coating consisting of an embedded or grafted photosensitizer [10-13], and ii) a titanium dioxide based photocatalyst coating [14, 15]. The main advantage of these light-activated coatings is the lack of developing microbe resistance with time [10]. Recently, we reported on the preparation of bio-inspired photoactivated antibacterial coatings on stainless steel (SS) with covalently attached photosensitizer of the 9-aminoacridine-3 type, which possess good photobactericidal activity against *G. negative E. coli* [13]. Therefore, here we report on the preparation and antibacterial activity of light-activated coatings based on protoporphyrin IX and bio-inspired nanogel based on Pox(mDOPA).

EXPERIMENTAL

Materials

Protoporphyrin IX (PPIX) (Sigma-Aldrich), N-hydroxysuccinimide (NHS), 1-(3-dimethylamino-propyl)-3-ethyl carbodiimide hydrochloride, 98+% (EDC) and poly (allylamine hydrochloride) (PAH) (Alfa Aesar) were used without further purification. Stainless steel 1.2 (SS) was used as a substrate. Poly (N-methacryloyl 3,4-dihydroxy-L-phenylalanine methyl ester)-b-poly (2-methacryloxyethyltrimethyl ammonium chloride) (P(mDOPA)-co-P(DMAEMA⁺) copolymer [16], poly (N-methacryloyl 3,4-dihydroxy-L-phenylalanine methyl ester) (P(mDOPA)) [17], oxidized poly (N-methacryloyl 3,4-dihydroxy-L-phenylalanine methyl ester)-/poly(allylamine) (Pox(mDOPA)/PAH)) cross-linked nanogel [18] were prepared as reported in [16-18].

* To whom all correspondence should be sent:

E-mail: rbryaskova@uctm.edu

Synthesis of (Pox(mDOPA)/PAH) cross-linked nanogel

Pox(mDOPA)/PAH-based nanogels were prepared according to a procedure reported in [17]. In brief, P(mDOPA) (10 mg) was dissolved in distilled water (10 mL) and NaOH (0.1 M) was slowly added in order to increase the pH of the medium to oxidize the catechol groups of P(mDOPA) and the solution was stirred for 12 h at room temperature. Then, an aqueous PAH solution (3 mL; 1 g L⁻¹) at pH 10 was slowly added to the Pox(mDOPA) solution and stirred for one hour at room temperature.

Synthesis of amino-modified protoporphyrin IX (PPIX-ED)

Amino-modified protoporphyrin IX (PPIX-ED) was prepared according to the procedure reported in [19]. In brief, PPIX (200 mg, 0.355 mmol) was dissolved in 20 ml DMF (pre-purged with N₂) at room temperature. To this solution, ethylene diamine (40 mg, 0.666 mmol), NHS (40 mg, 0.348 mmol), and EDC (190 mg, 0.991 mmol) were added under stirring at room temperature. After 30 minutes, a fine precipitate was obtained. The resulting mixture was stirred for 24 h at room temperature and after that, the precipitate was collected, washed with 50 mL of diethyl ether, and left to dry.

Preparation of the light-activated polymer coatings on SS substrate

Stainless steel samples with different sizes were cut out from the as-received 1 mm thick SS, 1.0 × 1.0 cm. They were cleaned and degreased by washing for 2 minutes with ethanol and acetone, respectively and purged by nitrogen. The substrate was first dipped in an aqueous solution of P(DOPA)-co-P(DMAEMA⁺) (2 g L⁻¹, pH 7) for 15 min, then rinsed with deionized water for 5 min, followed by dipping into an aqueous solution of Pox(mDOPA)/PAH nanogel (1 g L⁻¹) for 15 min and rinsed with deionized water for 5 min. The substrate was dipped in a solution of amino-modified PPIX (1

g L⁻¹, pH 10) for 15 min followed by rinsing with deionized water for 5 min.

Characterizations

ATR FT-IR spectra were recorded using Agilent Cary 600 equipment. Transmission electron microscopy (TEM) observations were carried out with a HR STEM JEOL JEM 2100 instrument. Dynamic light scattering (DLS) measurements were performed using a Brookhaven instrument (NanoBrook 90Plus) with ZetaPlus particle sizing software Version 5.23. SEM-EDX spectra were recorded on SEM Lyra, Tescan with Quantax EDS detector – Bruker. The inhibition zones of the antibacterial test were measured using Image-Pro Plus software.

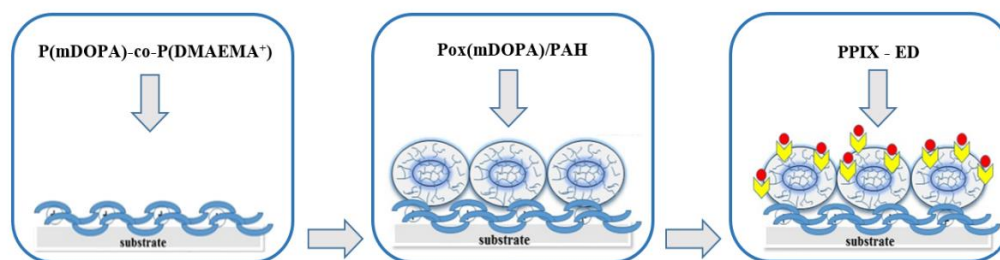
Antibacterial activity

The antibacterial activity of P(mDOPA)-co-P(DMAEMA⁺)/ Pox(mDOPA)/ PAH/ PPIX-ED coatings on SS substrate was tested against Gram-negative bacterium *Escherichia coli* (*E. coli*) and Gram-positive bacterium *Bacillus subtilis* (*B. subtilis*) using a modified agar disk-diffusion method (DDM). In this procedure, agar plates were inoculated with 0.2 ml of standardized inoculum (10⁷ cells.ml⁻¹) of the test microorganism. Then, films (previously sterilized by UV irradiation) deposited onto 1×1 cm SS substrate were placed on the agar surface. The Petri dishes were illuminated using a 300 W spotlight and incubated under suitable conditions (30°C for *B. subtilis* and 37°C for *E. coli*) for 24 hours. Then the diameters of inhibition growth zones were measured using Image-Pro Plus software.

RESULTS AND DISCUSSION

Preparation and surface characteristics of the light-activated antibacterial polymer coating on stainless steel

Light-activated antibacterial coatings were prepared by a simple dip-coating procedure, according to Scheme 1.



Scheme 1. Strategy for preparation of light-activated antibacterial coatings on stainless steel.

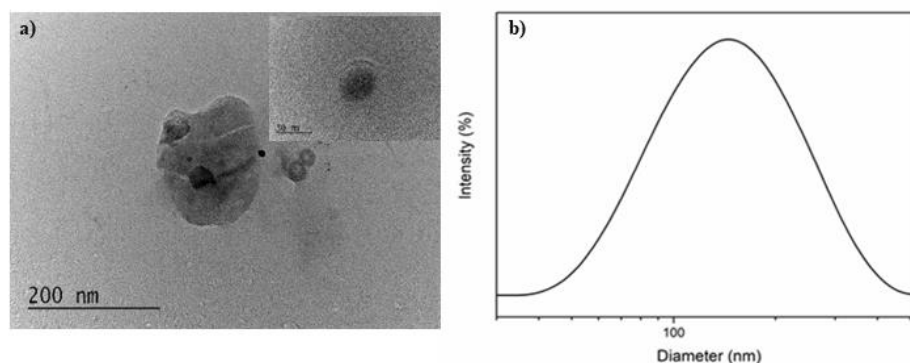
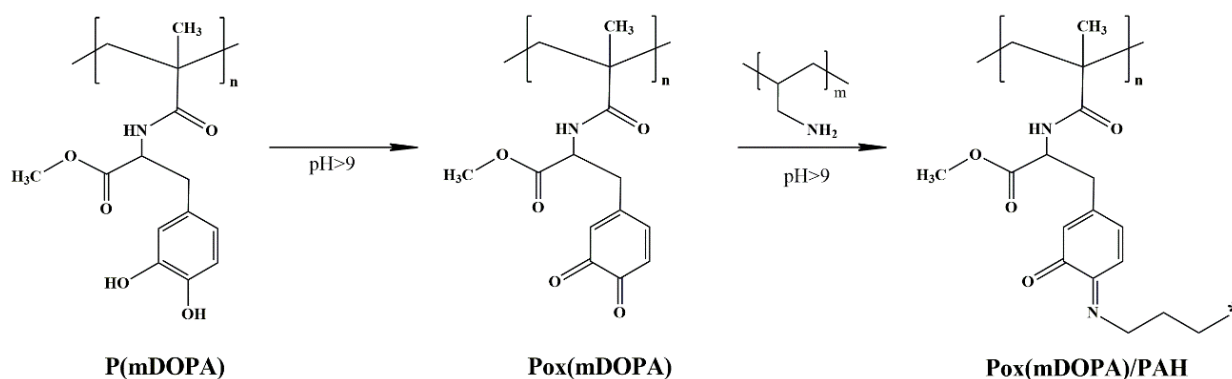
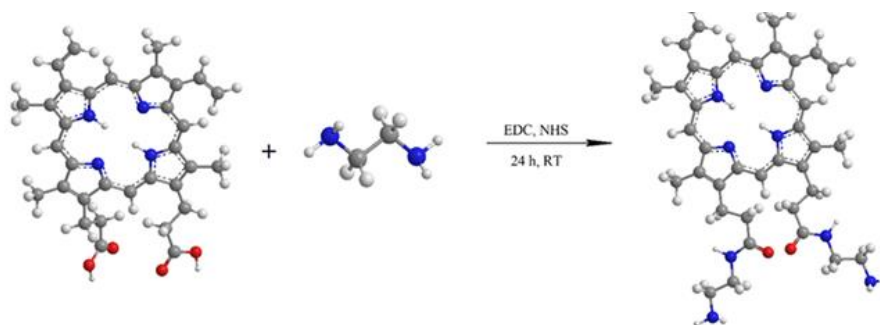


Figure 1. a) TEM of Pox(mDOPA)/PAH nanogels, b) DLS analysis of Pox(mDOPA)/PAH nanogels



Scheme 2. Preparation of Pox(mDOPA)/PAH nanogels



Scheme 3. Synthesis of amino-modified protoporphyrin IX

Initially, the substrate is immersed into an aqueous solution of polycationic P(mDOPA)-*co*-P(DMAEMA⁺) copolymer (2 g L⁻¹, pH 7) at room temperature. It is well known that DOPA-functionalized polycation copolymers can strongly anchor to the surface by DOPA/metal interactions [20]. The next layer is then built by dipping the substrate into an aqueous solution of Pox(mDOPA)/PAH nanogel (1 g L⁻¹, pH > 9), which can be further modified with an appropriate amino-modified photosensitizer by the well-known amino/quinone reaction. For this purpose, Pox(mDOPA)/PAH nanogels were prepared according to the procedure reported by Detrembleur *et al.* [17] by the addition of a PAH solution (1 g L⁻¹) to Pox(mDOPA) aqueous solution (Scheme 2) which results in the formation of nanogel particles.

The preparation of Pox(mDOPA)/PAH nanogel was proven by TEM and DLS analysis. The TEM images demonstrated the formation of spherical Pox(mDOPA)/PAH nanogel particles with an average size of 50 nm (Figure 1a). DLS analysis showed that the nanogel particles have an average hydrodynamic diameter of 120 ± 10 nm at an index of polydispersity of 0.25 (Figure 1b). The last step consists of deposition of an amino-modified protoporphyrin IX (PPIX-ED) (1 g L⁻¹), which is known for its high photoactivity and antibacterial properties [21]. The synthesis of PPIX-ED was performed according to Scheme 3.

The modification of protoporphyrin IX was proven by ATR-FTIR spectroscopy. The ATR-FTIR spectrum confirms the chemical modification of PPIX by displaying all characteristic peaks at 3300

cm^{-1} (νNH); 2911 cm^{-1} ($\nu\text{(s)CH}_2$); 2855 cm^{-1} ($\nu\text{(as)CH}_2$); 1628 cm^{-1} (amide I band) and 1533 cm^{-1} (amide II band) for $\nu\text{C=O}$ of $-\text{CONH}-$ groups.

The energy dispersive X-ray analysis with SEM (EDX-SEM) was used to analyze the chemical composition of the coatings, as well as the distribution and concentration of the elements at the surface and in the vicinity of the surface (Figure 2). The overall elemental mapping of the P(mDOPA)-co-P(DMAEMA⁺)/Pox(mDOPA)/PAH/PPIX-ED coatings on SS demonstrated uniform distribution of

the main elements which was derived from the obtained coating as follows: carbon (53.9 at. %), oxygen (2.79 at. %) and nitrogen (4.2 at. %) (Figure 2a). In comparison, in the overall elemental mapping of the pristine SS substrate, all elements characteristic for the SS substrate as iron (67.2 at. %), chromium (16.08 at. %), and nickel (9.15 at. %) were detected (Figure 2b). These results demonstrated the successful preparation of the light-activated polymer coatings.

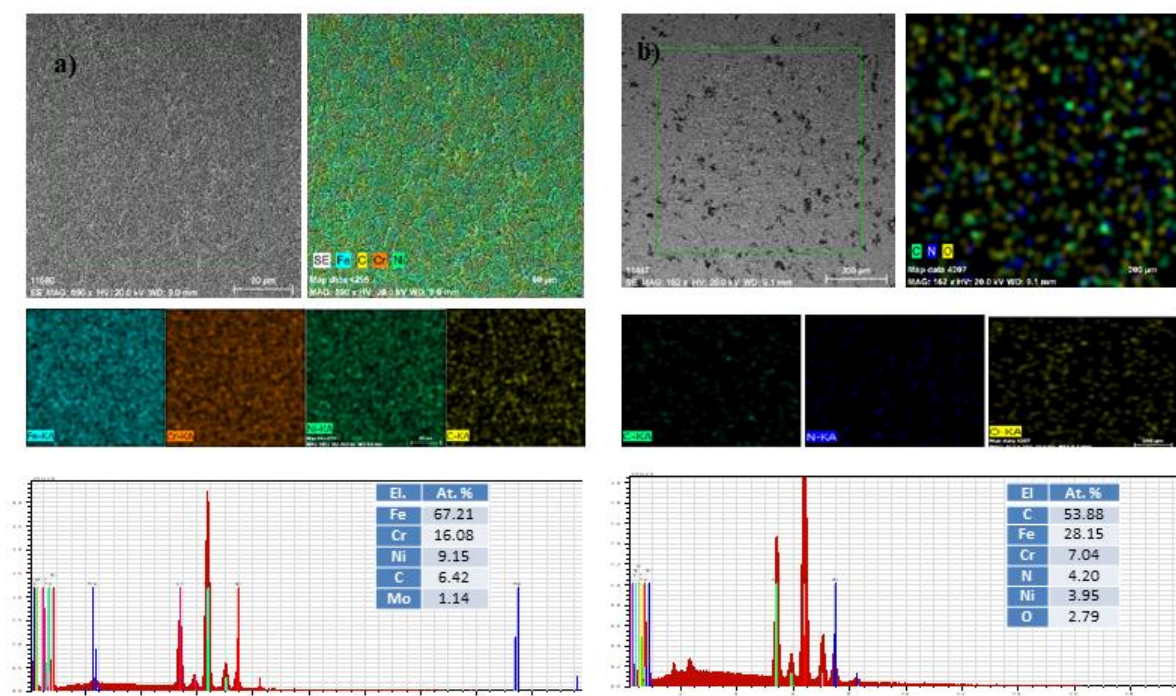


Figure 2. SEM-EDX mapping of a) neat SS substrate and b) P(mDOPA)-co-P(DMAEMA⁺)/Pox(mDOPA)/PAH/PPIX-ED coating on SS substrate.

Table 2. Antibacterial activity of the light-activated coatings on SS steel

Sample	<i>B. subtilis</i> Inhibition zone (mm)	<i>E. coli</i> Inhibition zone (mm)
P(mDOPA)-co- P(DMAEMA ⁺) /Pox(mDOPA)/PAH/PPIX-ED	12.6	16.5

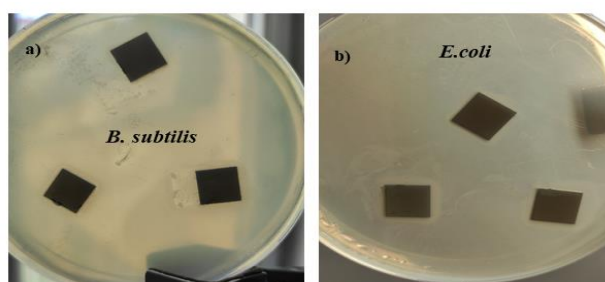


Figure 3. Antibacterial activity of P(mDOPA)-co-P(DMAEMA⁺) /Pox(mDOPA)/PAH/PPIX-ED against a) *B. subtilis* and b) *E. coli* by DDM.

Antibacterial activity of light-activated antibacterial coating

The antibacterial activity of the obtained light-activated coatings was demonstrated against Gram-negative *E. coli* and Gram-positive *B. subtilis* strains using DDM. It was found in both cases that the light-activated coatings possess strong bactericidal activity demonstrated by an inhibition zone in the range of 12-16 mm (Table 2, Figure 3 a, b). However, the bactericidal activity against G. negative *E. coli* was higher in comparison to G. positive *B. subtilis*, which is probably due to the difference in the membrane structures of the G. negative *E. coli* and G. positive *B. subtilis* strains, the peptidoglycan layer in the former being thicker.

CONCLUSION

In this study, light-activated antibacterial coatings were successfully prepared on a SS substrate using an amino-modified photosensitizing agent on the base of porphyrins. The EDX-SEM analysis indicates the deposition of the coatings on the SS substrate by the presence of all chemical elements arising from the components used. The established strong antibacterial activity of the coatings against G. negative *E. coli* and G. positive *B. subtilis* under light irradiation demonstrated their potential use in medical and biomedical fields.

Acknowledgements: The authors gratefully acknowledge the financial support from the National Science Fund of Bulgaria (project no. KP-06-H29/5).

REFERENCES

1. W. A. Rutala, D. J. Weber, *Am. J. Infect. Control.*, **47S**, A3 (2019).
2. W. A. Rutala, D. J. Weber, *Am. J. Infect. Control.*, **41S**, 2 (2013).
3. M. Ahonen, A. Kahru, A. Ivask, K. Kasemets, S. Kõljalg, P. Mantecca, I. Vinković Vrček, M. M. Keinänen-Toivola, F. Crijns, *Int. J. Environ. Res. Public Health*, **14**, 366 (2017).
4. K. Vasilev, *Coatings*, **9**, 654 (2019).
5. C. Adlhart, J. Verran, N.F. Azevedo, H. Olmez, M. M. Keinänen-Toivola, I. Gouveia, L. F. Melo, F. Crijns, *J. Hosp. Infect.*, **99**, 239 (2018).
6. X. Zhang, L. Wang, E. Levänen, *RSC Adv.*, **3**, 12003 (2013).
7. H. Zhu, Z. Guo, W. Liu, *Chem Commun (Camb)*, **50**, 3900 (2014).
8. C. Krumm, J. C. Tiller, *Nachrichten aus der Chemie*, **62**, 984e7 (2014).
9. R. Bonnett, *Chem. Soc. Rev.*, **24**, 19 (1995).
10. K. Page, M. Wilson, I. P. Parkin, *Mater. Chem.*, **19**, 3819 (2009).
11. A. J. T. Naik, S. Ismail, Ch. Kay, M. Wilson, I. P. Parkin, *Materials Chemistry and Physics*, **129**, 446 (2011).
12. M. J. Bovis, S. Noimark, J. H. Woodhams, C. W. M. Kay, J. Weiner, W. J. Peveler, A. Correia, M. Wilson, E. Allan, I. P. Parkin, *RSC Adv.*, **5**, 54830 (2015).
13. R. Bryaskova, N. Philipova, N. Georgiev, I. Lalov, V. Bojinov, C. Detrembleur, *Journal of Applied Polymer Science*, **138**, 50769 (2021).
14. G. W. Park, M. Cho, E. L. Cates, D. Lee, B. T. Oh, J. Vinje, et al. *J. Photochem. Photobiol. B*, **140**, 315 (2014).
15. J. Bogdan, J. Zarzynska, J. Plawinska-Czarnak. *Nanoscale Res. Lett.*, **10**, 1023 (2015).
16. E. Faure, P. Lecomte, S. Lenoir, C. Vreuls, C. Van De Weerd, C. Archambeau, J. Martial, C. Jerome, A.-S. Duwez, C. Detrembleur, *J. Mater. Chem.*, **21**, 7917 (2011).
17. E. Faure, C. Falentin, T. S. Lanero, C. Vreuls, G. Zocchi, C. Van de Weerd, J. Martial, C. Jérôme, A.-S. Duwez, C. Detrembleur, *Adv. Funct. Mater.*, **22**, 5271 (2012).
18. E. Faure, C. Falentin-Daudré, C. Jérôme, J. Lyskawa, D. Fournier, P. Woisel, C. Detrembleur, *Prog. Polym. Sci.*, **38**, 236 (2013).
19. J. Sherrill, S. Michielsen, I. Stojiljkovic, *Journal of Polymer Science: Part A: Polymer Chemistry*, **41**, 41(2003).
20. H. Lee, N. F. Scherer, P. B. Messersmith, *Proc. Natl. Acad. Sci. U.S.A.*, **103**, 12999 (2006).
21. E. R. Reis, K. Metze, E. M. D. Nicola, J. H. Nicola, I. E. Borissevitch, *Journal of Luminescence*, **137**, 32 (2013).

Direct mechanochemical synthesis and characterization of SrWO₄ nanoparticles

M. Gancheva^{1*}, R. Iordanova¹, L. Mihailov²

¹*Institute of General and Inorganic Chemistry, Bulgarian Academy of Sciences, Acad. G. Bonchev str., bl.11, 1113 Sofia, Bulgaria*

²*Faculty of Chemistry and Pharmacy, Sofia University "St. Kliment Ohridski", J. Bourchier blvd 1, 1164 Sofia, Bulgaria*

Received: September 14, 2022; Revised: November 16, 2022

Single-phase nanocrystalline SrWO₄ was successfully synthesized by direct mechanochemical reaction at room temperature. A stoichiometric mixture of SrCO₃ and WO₃ in a 1:1 molar ratio was subjected to intense mechanical treatment in air using a planetary ball mill at different ball-to-powder weight ratios (BPR). The phases and structural transformations were monitored by X-ray diffraction (XRD) and infrared (IR) spectroscopy. Morphology of the obtained products was determined by transmission electron microscopy (TEM). The synthesis of SrWO₄ occurred after 1 h milling time at a high ball-to-powder weight ratio (20:1) and a milling speed of 500 rpm. On the other hand, the SrWO₄ formation was completed after 4 h milling time at a lower ball-to-powder weight ratio (10:1) and the same milling speed. The average particle size of the as-prepared SrWO₄ powders was found to be 21 nm which decreased to 16 nm on increasing the ball-to-powder weight ratio (20:1). The UV-Vis absorption spectra of both materials showed a strong peak at 210 nm and the calculated optical band gaps were in the range of 4.72-4.92 eV.

Keywords: high energy milling, ball-to-powder weight ratio, XRD, TEM, UV-Vis

INTRODUCTION

SrWO₄ is an important member of alkaline-earth metal tungstate family with scheelite type structure where Sr ions are coordinated with eight oxygen atoms and W ions are connected to four oxygen atoms forming WO₄ groups [1]. This compound finds applications as: microwave dielectric material [2], host matrix for doping with rare earth active ions [3] anode material for lithium ion batteries [4], catalysts [5, 6], etc. Conventionally, SrWO₄ is prepared by the solid-state reaction of SrCO₃ and WO₃ between 700-1000 °C for several hours [7-9]. The sol-gel [4], hydrothermal synthesis [10], sonochemical method [11], co-precipitation [12], microwave-assisted route [13, 14], spark plasma sintering-reactive synthesis [15], electrochemical-assisted precipitation process [16] and mechanochemical synthesis [17] have been used for the preparation of this phase. The advantages of the mechanochemical method are: direct synthesis without additional heat treatment; decrease in synthesis time or temperature needed to obtain the final products; control of particle size and ability to prepare high purity materials like MOFs [18], inorganic mixed oxides [19, 20], etc. Many parameters as type of mill, milling speed, time, atmosphere or ball-to-powder weight ratio (BPR) affect the phase composition, microstructure, morphology and properties of the final products.

The major parameter during mechanochemical treatment is the milling speed which is a decisive factor for the rapid synthesis [19-23]. The high milling speed enables a faster synthesis while the low milling speed is not sufficient for completing the synthesis. The longer milling time may lead to the formation of undesirable phases [22, 24]. Types, size and number of balls used also play an important role in particle size of synthesized powders [25]. The BPR is another crucial parameter. The ratio has a significant effect on the time required to produce the desired phase or reduce the particle size. Generally, a higher value of this ratio will result in a shorter time required for phase formation [19]. The aim of the present work was to check the possibility for facile synthesis of SrWO₄ by mechanochemical activation using different ball-to-powder weight ratios (10:1 and 20:1). The formation of the desired phase, the morphology and optical properties of the obtained materials were discussed.

EXPERIMENTAL

A mixture of SrCO₃ (Merck, purity 99.9%) and WO₃ (Merck, purity 99.9%) in a molar ratio of 1:1 was subjected to intense mechanical treatment in a planetary ball mill (Fritsch–Premium line–Pulverisette No 7). Both vials and balls were made of stainless steel; the milling speed was 500 rpm.

* To whom all correspondence should be sent:
E-mail: m.gancheva@svr.igic.bas.bg

The ball-to-powder weight ratio (BPR) was 10:1 and 20:1. To minimize the temperature raise during the milling, the process was carried out for periods of 15 min, with rest periods of 5 min [26]. The milling process and the labels of samples are given in Table 1.

Table 1. The milling parameters of the mechanochemical process for preparation of SrWO₄

Sample	Milling speed	Ball-to-powder weight ratio (BPR)	Milling time
A	500 rpm	10:1	1-5h
B	500 rpm	20:1	1-3h

The phase and structural transformation of the milling samples were investigated by X-ray powder diffraction analysis (XRD) and infrared spectroscopy (IR). The powder X-ray diffraction study was performed on a Bruker D8 Advance instrument equipped with a copper tube (CuK α). The average crystallite sizes of SrWO₄ powders resulting from X-ray diffraction broadening were determined by the Scherrer's formula at the diffraction peak $2\theta = 33.10^\circ$. Infrared spectra were registered in the range of 1600–400 cm⁻¹ on a Nicolet-320 FTIR spectrometer using the KBr pellet technique. TEM observation was performed by a JEOL JEM-2100 microscope at an accelerating voltage of 200 kV. The preparation procedure of the specimen consisted of dispersing them in ethanol by ultrasonic treatment and dripping on standard Cu grids. UV-Vis spectra were recorded on an Evolution 300 spectrophotometer in the range from 200 to 1000 nm. The optical absorption band was calculated based on Tauc's equation $ah\nu = A(h\nu - E_g)^n$, where α is the absorption coefficient, A is the absorption constant, h is Planck's constant, ν is the photon frequency. In the mentioned relation, n represents the type of semiconductor charge transition [27]. The value of n is related to the characteristics of the electronic transition type in the semiconductors and $n = 0.5$ for a direct allowed transition; $n = 2$ for an indirect allowed transition; $n = 3$ for an indirect forbidden transition and $n = 3/2$ for a direct forbidden transition. SrWO₄ is known as a direct transition metal oxide, and therefore the value of $n = 0.5$ was selected to be used in Tauc's equation.

RESULTS AND DISCUSSION

The effect of the ball-to-powder weight ratio (BPR) on the formation of SrWO₄ powders was monitored by X-ray diffraction analysis (Figs. 1 and 2). Before ball milling the principal peaks of monoclinic WO₃ (PDF-01-043-1035) and orthorhombic SrCO₃ (PDF-00-005-0418) were observed.

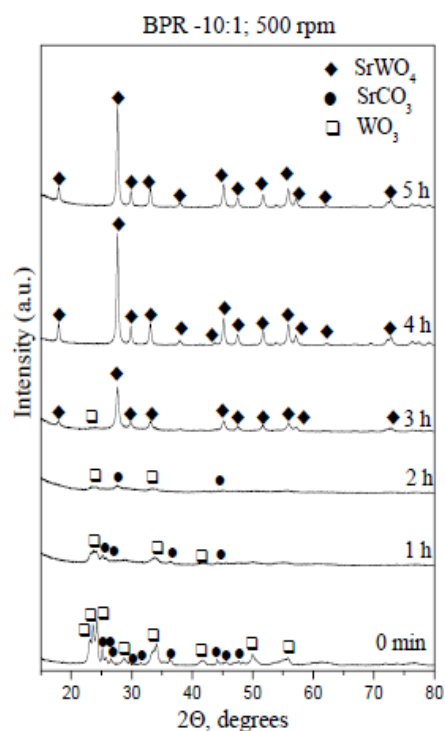


Fig. 1. XRD patterns of sample A mechanically activated for different milling times

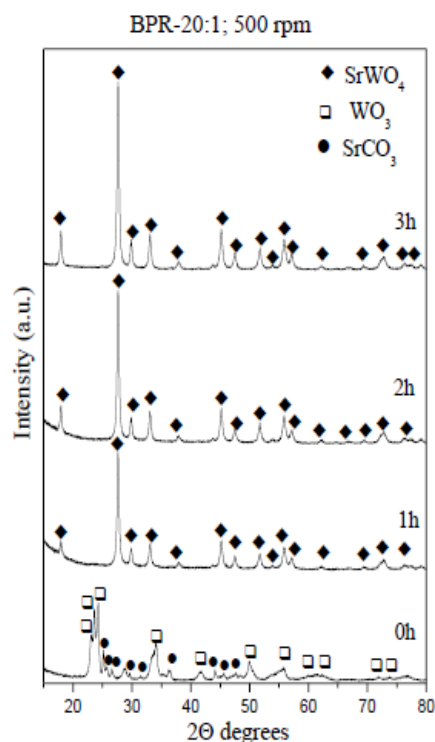


Fig. 2. XRD patterns of sample B mechanically activated for different milling times

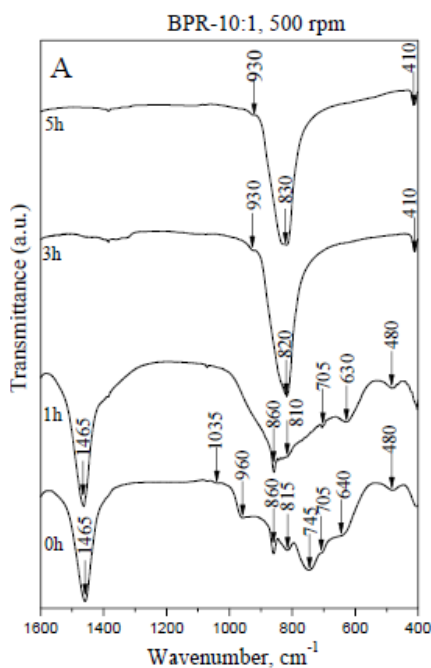


Fig. 3A. IR spectra of sample A mechanically activated for different milling times

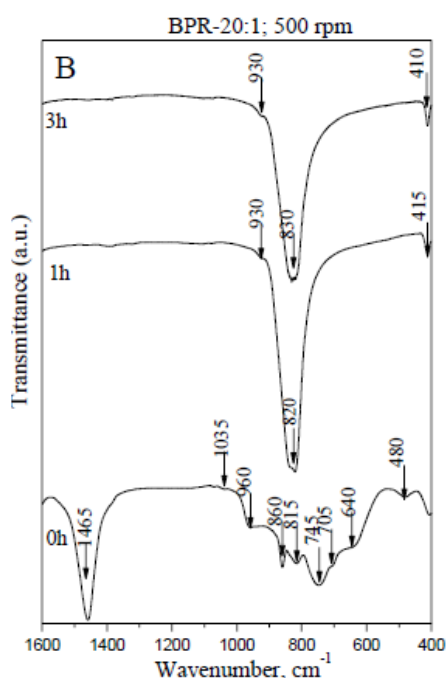


Fig. 3B. IR spectra of sample B mechanically activated for different milling times

After 1 h of milling time at a speed of 500 rpm using the lower BPR (10:1) they were broadened and their intensity had strongly decreased. This is a result of a reduction in particle sizes, destruction of the long-range order and accumulation of defects. During this milling process the initial reagents become amorphous. Increasing the milling time up to 3 h led to the appearance of new diffraction lines typical of the tetragonal type structure SrWO₄ (PDF-01-083-6135). The very low intensity peak at 23.70

° characteristic for WO₃ was also detected. The additional mechanochemical activation up to 4 h yielded a single phase of SrWO₄. Between 4 and 5 h of milling no change of XRD pattern was visible (Fig. 1).

The crystallite size of as-obtained SrWO₄ (after 5 h milling time) was calculated using Scherrer's equation for diffraction peak at $2\Theta = 33.10^\circ$ as 26 nm. With increasing BPR up to 20:1 at a milling speed of 500 rpm, the reaction between the reagents was performed after 1 h milling time (Fig. 2). Additional mechanical treatment up to 3 h did not lead to any changes in the XRD patterns of the sample. This is an indication for the structural stability of SrWO₄. The crystallite size of as-obtained SrWO₄ (after 1 h milling time) at the diffraction peak of $2\Theta = 33.10^\circ$ was 22 nm. The phase formation of SrWO₄ with increasing BPR (20:1) is due to the more effective solid-state diffusion between reagents in the course of ball-materials collisions.

The phase formation of SrWO₄ during the mechanochemical treatment was confirmed by IR spectroscopy. The IR spectrum of the non-activated mixture exhibits absorption bands typical of structural units of WO₃ (bands at 960, 815 and 745 cm⁻¹) and of SrCO₃ (bands at 1465, 860, 705 640 and 480 cm⁻¹) [28-30] (Figs. 3A and 3B). The IR spectra of the sample A activated at lower BPR (10:1) are presented in Fig. 3A. The bands at 1035, 960 and 745 cm⁻¹ disappeared after the early stages of the ball milling (1 h). Noticeable changes in the IR spectrum were observed after 3 h of milling time which confirmed the phase formation of SrWO₄. The new absorption bands are in good agreement with literature data [2, 11, 13, 14, 31]. The shoulder at 925 cm⁻¹ was assigned to anti-symmetry stretching vibrations (ν_1) in [WO₄] tetrahedral units. The strong band at 830 cm⁻¹ was attributed to the symmetry stretching vibration ν_3 of the same groups. The weak band at 410 cm⁻¹ is due to bending mode of the WO₄ entity [31]. For the material obtained using higher BPR (20:1) these bands appeared after 1 h of milling time indicating a faster chemical reaction (Fig. 3B).

The morphology and particle size distribution of SrWO₄ nanoparticles were analyzed by transmission electron microscopy. The TEM image at a lower magnification of the sample A shows that SrWO₄ nanocrystallites are aggregates consisting of many particles with nearly spherical form (Fig. 4A). The TEM images indicated that the particles exhibited homogeneity in shape (Figs. 4A and 4B). The particle size distribution histogram of sample A shown in Fig. 4C indicates that the grain sizes are between 10-60 nm and the average size is 21 nm.

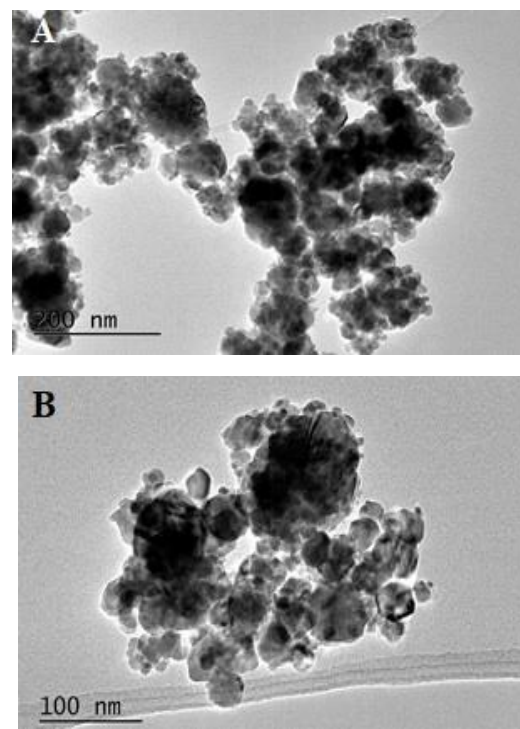
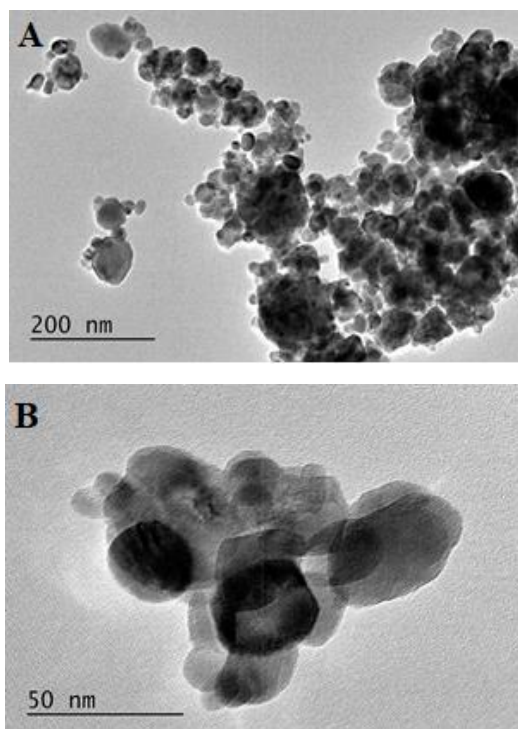


Fig. 4. TEM images (A and B) of the mechanochemically obtained SrWO₄ (sample A) after 5 h milling at BPR 10:1 and histogram of the particle size distribution (C).

The TEM studies of samples B (BPR 20:1) are presented in Fig. 5. No morphological differences were detected in SrWO₄ with the increase in BPR (Figs. 5A and 5B). In this case the crystallites exhibit more spherical form and their size is below 50 nm. With increasing BPR grain sizes between 1-40 nm were observed, the average size being 16 nm. The comparison of the particle size distribution of samples A and B shows that the particle size tends to decrease with the increase in BPR. The particle size distribution changed from narrow to wide from sample A to sample B.

Fig. 5. TEM images (A and B) of the mechanochemically obtained SrWO₄ (sample B) after 5 h milling at BPR 20:1 and histogram of the particle size distribution (C).

The optical properties of the mechanochemically obtained SrWO₄ powders were studied by UV-Vis diffuse reflectance spectroscopy. The UV-Vis reflectance spectra of SrWO₄ (samples A and B) exhibited a strong band at 210 nm which is typical for wide-band gap compounds (Fig. 6).

The peak at 210 nm is characteristic of O (2p) → W (5d) charge transfer in WO₄ tetrahedra [16]. The experimental optical band gap energy of nanocrystalline SrWO₄ was found by extrapolating the linear portion in an (F/R)^{1/2} vs. hv plot, as shown in Fig. 7.

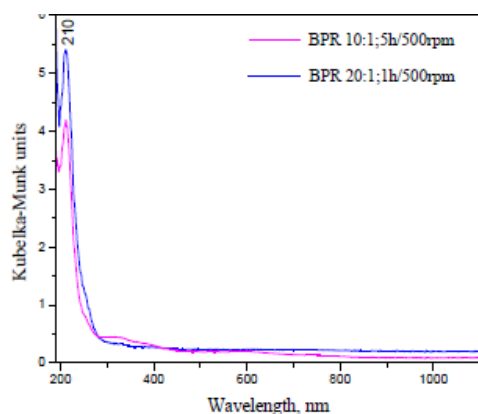


Fig. 6. Diffuse reflectance UV-Vis spectra of mechanochemically synthesized SrWO₄ powders at different BPR.

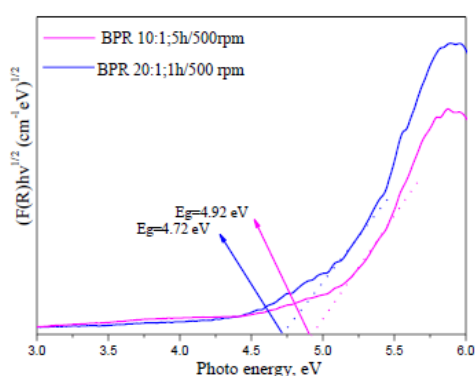


Fig. 7. Tauc plot of mechanochemically synthesized SrWO₄ powders at different BPR.

The band gap of the mechanochemically obtained SrWO₄ (sample A) was estimated to be 4.92 and decreased to 4.72 eV for SrWO₄ (sample B) using the higher ball-to-powder weight ratio 20:1. The value of the optical band gap is higher than those reported in the literature [3, 9, 16]. Table 2 gives the data of the average crystallite size and optical band gap value of both samples. The decrease in optical band gap value can be attributed to decreasing of the crystallite size.

Table 2. Mechanochemical synthesis of SrWO₄ and physico-chemical characteristics.

SrWO ₄	Milling time	D _{nm} -XRD	D _{nm} -TEM	E _g , eV
A	5 h BPR -10:1	27	22	4.92
B	1 h BPR -20:1	22	16	4.72

CONCLUSIONS

In this research, the effect of the ball-to-powder weight ratio (BPR) on the formation of SrWO₄ powder was studied. The mechanochemical treatment at lower BPR (10:1) and milling speed of 500 rpm induces amorphization of the reagents up to

2 h milling time. The phase formation of tetragonal SrWO₄ occurred at 5 h milling time. A faster synthesis of SrWO₄ was realized on applying a higher BPR (20:1) after 1 h of milling time with a milling speed of 500 rpm. The particle morphology of the as-obtained products mainly consists of special shapes. The average particle size determined by TEM analysis well matches that calculated from XRD data. UV-Vis spectroscopy indicated that SrWO₄ particles had strong visible light absorption and band gaps in the range of 4.72-4.92 eV.

Acknowledgements: The authors kindly acknowledge the financial support of project № BG05M2OP001-1.002-0014 „Centre of Competence HITMOBIL - Technologies and systems for generation, storage and consumption of clean energy”, funded by Operational Programme “Science and Education for Smart Growth” 2014-2020, co-funded by the EU from European Regional Development Fund.

REFERENCES

1. L. L. Chang, M. G. Scroger, B. Phillips, *J. Amer. Ceram. Soc.*, **49**, 385 (1966).
2. A. Priya, E. Sinha, S. K. Raou, *Solid State Science*, **20**, 40 (2013).
3. P. Jena, S. K. Gupta, K. Sudarshan, N. Pathak, A. K. Singh, *J. Mater. Sci.: Mater. Electron.*, **16** (2018)
4. L. Zhang, Q. Bai, L. Wang, A. Zhang, Y. Zhang, Y. Xing, *Func. Nat. Letters*, **7**, 1450010 (2014).
5. M. Kowalkinska, P. Gluchowski, T. Swebosci, T. Ossowski, A. Ossowski, W. Bednarski, J. Karcewski, A. Zielinska-Jurek, *J. Phys. Chem. C*, **125**, 25497 (2021).
6. M. Arunpandian, D. Sivaganesh, M. S. Revathy, K. Selvakumar, S. Arunachalam, D. Geetha, *Intern. J. Envir. Anal. Chem.*, (2020) doi: 10.1080/03067319.2020.1803847.
7. F. Jiandong, Z. Huaijin, W. Zhengping, G. Wenwei, W. Jiyang, *Front. Chem. China*, **3**, 264 (2006).
8. A. Afif, J. Zaini, S. M. H. Rahman, S. Eriksson, M. Aminul Islam, A. K. Azad, *Science Report*, **9**, 9173 (2019).
9. D. W. Kim, I. Cho, S. S. Shin, S. Lee, T. H. Noh, D. H. Kim, H. S. Jung, K. S. Hong, *J. Solid State Chem.*, **184**, 2103 (2011).
10. H. Pan, M. Hojamberdiev, G. Zhu, *J. Mater. Sci.*, **47**, 746 (2012).
11. T. Thongtem, A. Phuruangrat, S. Thongtem, *Appl. Surface Science*, **254**, 7581 (2008)
12. M. Muralidharan, V. Anbarasu, A. Elaya Perumal, K. Sivakumar, *J. Mater. Sci.: Mater. Electron.*, (2015).
13. C. S. Lim, *Asian J. Chem.*, **24**, 2843 (2021).
14. T. Thongtem, A. Phuruangrat, S. Thongtem, *J. Nanopart. Res.*, **12**, 2287 (2010).
15. E. K. Papyonov, O. O. Shichalin, I. Yu. Buravlev, A. A. Belov, A. S. Portnyagin, A. N. Fedorets, Yu. A.

- Azarova, I. G. Tananaev, V. I. Sergienko, *Vacuum*, **180**, 109628 (2020).
16. X. Li, Z. Song, B. Qu, *Ceram. Intern.*, **40**, 1205 (2014).
17. L. Cheng, P. Liu, S. X. Qu, H. W. Zhang, *J. Alloys Comp.*, **581**, 553 (2013).
18. A. P. Amrute, B. Zibrowius, F. Schüth, *Chem. Mater.*, **32**, 4699 (2020).
19. M. Mancheva, R. Iordanova, Y. Dimitriev, *J. Alloys Compd.*, **509**, 15 (2011).
20. M. Gancheva, T. Rojac, R. Iordanova, I. Piroeva, P. Ivanov, *Ceram. Intern.*, **48**, 17149 (2022).
21. F. Palazon, Y. El Ajjouri, P. Sebastia-Luna, S. Lauciello, L. Manna, H. J. Bolink, *J. Mater. Chem. C*, **7**, 11406 (2019).
22. C. Suryanarayana, *Intermetallics*, **3**, 153 (1995).
23. S. Hwang, S. Grätz, L. Borchardt, *Chem. Commun.*, **58**, 1661 (2022).
24. V. V. Boldyrev, *Russ. Chem. Rev.*, **75**, 203 (2006).
25. M. Zakeria, M. Ramezani, A. Nazari, *Materials Research*, **15**, 891 (2012).
26. M. Gancheva, R. Iordanova, Y. Dimitriev, D. Nihtianova, P. Stefanov, A. Naydenov, *J. Alloys Comp.*, **570**, 34 (2013).
27. J. Tauc, *Mater. Res. Bull.*, **5**, 721 (1970).
28. M. F. Daniel, B. Desbat, J. C. Lassegues, B. Gerand, M. Figlarz, *J. Solid State Chem.*, **67**, 235 (1987).
29. C. L. Veenas, L. R. Asitha, V. C. Bose, A. S. A. Raj, G. Madhu, V. Biju, *Mater. Sci. Eng.*, **73**, 012119 (2015).
30. P. Lu, X. Hu, Y. Li, M. Zhang, X. Liu, Y. He, F. Dong, M. Fub, Z. Zhan, *RSC Adv.*, **8**, 6315 (2018).
31. G. M. Clark, W. P. Doyle, *Spectrochim. Acta*, **22**, 1441 (1966).

Influence of the applied external voltage on anaerobic digestion with integrated microbial electrolysis cell

P. G. Velichkova*, S. G. Bratkova, A. T. Angelov

Department of Engineering Geoecology, University of Mining and Geology "St. Ivan Rilski", Sofia 1700, Bulgaria

Received: July 26, 2022; Revised: November 16, 2022

An external microbial electrolysis cell (MEC) was integrated into the ethanol stillage anaerobic digestion reactor (AD). The AD-MEC system is a promising technology for enhancing biogas production. It accelerated methane production and stabilized the process. A change in applied external voltage could change microbial metabolism and affect substrate degradation rate, volatile fatty acid (VFA) generation and biogas production. The effect of applied external voltage on biodegradability, VFA and methane content in produced biogas was studied. Four values of external voltage were selected - 0.6, 0.8, 1.0 and 1.2 V. The kinetics of biogas production for 15 days was monitored. Methane yields increased to 84, 88 and 82 % ("vol.") at 0.6, 0.8 and 1.0 V voltages of the microbial electrolysis cell, respectively. Higher voltage (1.2 V) did not increase the methane content vs AD-only process (75 %, vol.). The best biodegradability was achieved at low voltages (0.6 and 0.8 V) - reduction of chemical oxygen demand by 88-89 % and purification of ethanol stillage from sulfates. Acetic acid decreased by 96 % at 0.6 V, 95 % at 0.8 V, 74 % at 1.0 V and 65 % at 1.2 V.

Keywords: Anaerobic digestion, microbial electrolysis cell, ethanol stillage, VFA, COD

INTRODUCTION

The microbial electrolysis cell (MEC) is the commonest bioelectrochemical system with anaerobic digestion (AD) being studied. The integration of MEC into an AD reactor (AD-MEC) improves the process by alleviating volatile fatty acids (VFA) accumulation, shortening solid retention time, enhancing hydrolysis/acidogenesis rates, and enriching exoelectrogen/methanogen activities, so improving the AD performance [1]. Moreno *et al.* found that MEC could enhance biomethane production rate, resulting from the alleviation effects of reduced VFA accumulation [2]. In recent research was reported that methane yield even exceeds 90 % from an AD-MEC system [3-5]. The advantages of AD-MEC include less energy (voltage < 1.0 V) which was required for hydrogen production compared to water electrolysis (voltage > 1.2 V) process and higher hydrogen yield compared to conventional fermentation-based processes [1].

The biomethane productivity responds to voltage application are highly substrate-dependent. In addition, the change in VFAs content or decrease in chemical oxygen demand (COD) also varies for different substrates. For example, in terms of methane productivity, there existed an optimum applied voltage for palm oil mill effluent, while voltage application shows insignificant impact on swine manure [1]. The applied voltage affects both the methane enhancement and productivity. Results

showed that AD-MEC operated at 0.4–0.8 V have better biomethane productivity, suggesting the existence of an optimal applied voltage for microbial growth and associated electrochemical bioreaction rates. High voltage (>1.0 V) can be harmful to microorganisms, while the applied voltage should exceed a threshold value to overcome the thermodynamic barrier for the desired electrochemical bioreactions [1, 6]. The VFAs are generated by AD but could not be converted mainly to methane. An extra energy input is needed to convert VFAs to biogas [7]. They can be converted into hydrogen by applying voltage.

In the present study, the influence of the applied external voltage on the reduction of VFAs (lactic, acetic, propionic and butyric acids) and organic matter was studied. Analyzes were performed in four operating modes of AD-MEC - with 0.6, 0.8, 1.0 and 1.2 V external voltage. The process was monitored for 15 days by sampling the inlet and outlet of the reactor at different voltages. The samples were analyzed for COD and VFAs.

EXPERIMENTAL

Microbial electrolysis cell configuration

The scheme of the laboratory installation is shown on Fig. 1a and the picture – on Fig. 1b. The anaerobic reactor has a working volume of 5 dm³. Two graphite plates measuring 100 × 100 × 6 mm were used as electrodes.

* To whom all correspondence should be sent:
E-mail: polina.velichkova@mgu.bg

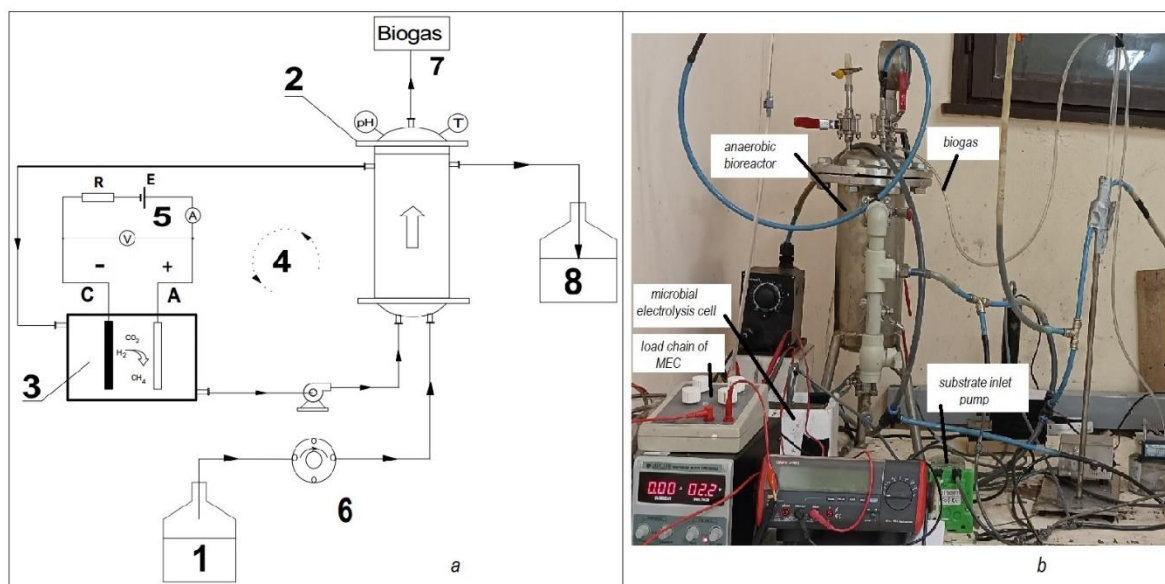


Fig. 1. Scheme (a) and picture (b) of an integrated AD-MEC system. Legend: 1- substrate input, 2- anaerobic bioreactor (UASB), 3- microbial electrolysis cell (MEC), 4- recirculation flow, 5- load chain of MEC, 6- substrate inlet pump, 7-biogas, 8- reactor outlet.

Spacing between the anode and cathode placed on opposite sides measured 20 mm. Recirculation pumps moved the flow.

The microbial electrolysis cell is integrated outside the volume of the anaerobic reactor. The cathode and anode electrodes were connected to the power supply, with an external resistance of 10 Ω . The reactor system was filled with ethanol stillage and 10 % of volume of substrate inoculum from a mixed methanogenic consortium (activated sludge). 273 ml/day of stillage is pumped to the reactor.

Stillage and activated sludge

Stillage was obtained after the separation of ethanol obtained by acid hydrolysis of starch-containing plants from “Kehlibar” Winery Ltd, Svetovrachene, Bulgaria. The stillage was stored in a refrigerator. Before use, it was neutralized to pH 7.5 with NaOH. Activated sludge was taken from “Almagest” AD, Verinsko, Bulgaria.

Analytical methods

Chemical oxygen demand was measured with COD Ultra-High Range Reagent Vials, EPA method (Hanna Instruments). The sulfate concentration was determined using a spectrophotometric method at λ 420 nm using BaCl₂ as a reagent. The contents of CO₂, CH₄, H₂S and H₂ in the produced biogas were measured using a portable gas analyzer "Draeger X-am 7000". The acid composition in the ethanol stillage at the inlet and outlet of the installation was determined by HPLC at the Institute of Chemical Engineering - BAS. Scanning electron microscopy (SEM) was

used for scanning the biofilm on electrodes. Prior to SEM, the samples were fixed with 2 % glutaraldehyde in 0.1 M phosphate buffer overnight in the fridge (4 °C) and then were dried with ethanol. After that, the samples were kept in a desiccator for 48 hours and then were coated with a thin layer of graphite.

RESULTS AND DISCUSSION

Change in the composition of volatile fatty acids

Samples were taken on the 14th day from the beginning of the decomposition of the ethanol stillage in AD-MEC for each of the applied external voltages at the inlet and outlet of the reactor- 0.6, 0.8, 1.0, 1.2 V. The obtained results for lactic, acetic, butyric and propionic acids are given in Table 1.

The lactic, acetic, butyric and propionic acids were consumed as a food source for the microbial communities. The best degradability was achieved at 0.8 V, followed by 0.6, 1.2 and 1.0 V, respectively. The acetic acid is considered as the key intermediate product for methane production. The decrease in acetic acid concentration indicated that exoelectrogens on the anodes might actively consume acetic acid for the current generation, which was used for the reduction at the cathodes for the methane production. Such results are reached by Arvin *et al.* [7], where the acetic acid content decreases from 317 mg/L in the first phase to 278.3 mg/L in the second, 79.7 mg/L in the third, and 70.6 mg/L in the fourth phase in AD-MEC with external voltage 1.0 V.

Table 1. Content of VFAs in the ethanol stillage before and after methanation in AD-MEC at different external voltage

VFA	Sample							
	AD-MEC 0.6V		AD-MEC 0.8V		AD-MEC 1.0V		AD-MEC 1.2V	
	input	output	input	output	input	output	input	output
Lactic acid, g/L	0.67	<0.01	2.5	<0.01	1.98	0.15	<0.01	<0.01
Acetic acid, g/L	5.20	0.19	2.8	0.15	4.39	1.14	4.03	1.42
Propionic acid, g/L	5.93	0.12	3.54	<0.01	5.44	0.75	5.01	0.67
Butyric acid, g/L	1.15	<0.01	0.15	<0.01	0.52	0.08	1.20	<0.01

Table 2. COD and sulfates value input and output of reactor at different external voltage

Parameter	AD, control experiment	AD-MEC with applied voltage			
		0.6V	0.8V	1.0V	1.2V
COD _{input} , g O ₂ /L	99.44	58.48	87.36	104.12	69.44
COD _{output} , g O ₂ /L	34.08	5.68	9.76	15.4	47.48
SO ₄ ²⁻ _{input} , mg/L	847.45	860.23	562.16	978.38	875.67
SO ₄ ²⁻ _{output} , mg/L	450	<1	<1	153.75	<1

The results in Table 1 show that acetic acid decreased from 5.2 to 0.19 g/L (by 96 %) at 0.6 V, from 2.8 to 0.15 g/L (by 95 %) at 0.8 V, from 4.39 to 1.14 g/L (by 74 %) at 1.0 V and from 4.03 to 1.42 g/L (by 65 %) at 1.2 V. At the end of biogas production, 0.12, 0.75 and 0.67 g/L propionic acid were detected at 0.6, 1.0 and 1.2 V, respectively, while at 0.8 V it was consumed by the methanogens. The lactic acid was also completely degraded at 0.6 and 0.8 V, while at 1.0 V 0.15 g/L were detected. At 1.2V, it was not detected either at the inlet or outlet of the installation, which may be due to a chemical change that occurred during storage of the substrate. The butyric acid was consumed in 3 of the cases - at 0.6, 0.8 and 1.2 V. At 1.0 V a minimum quantity was detected - 0.08 g/L butyric acid. This improves the microbial activities and does not interfere with the process of methanogenesis.

Venkata and Lenin proved that a change in applied voltage could change microbial metabolism and consequently affect substrate degradation rate, volatile fatty acid generation and biohydrogen production. The activity of dehydrogenase enzyme and biohydrogen production had a maximum value at applied voltage of 0.6 and 1.0 V, respectively [8].

Change in chemical oxygen demand and sulfates

Table 2 shows the values of the two most important parameters related to the results of wastewater treatment - COD and sulfates. As can be seen from the data in Table 2, the degradability of organic matter at 0.6, 0.8, 1.0 and 1.2 V external voltage is 89.72 %, 88.83 %, 85.21 % and 31.62 %, respectively. Sulfates from the ethanol stillage are reduced to hydrogen sulfide and sulfides by anaerobic bacteria. In the presence of an electric field, sulfides are oxidized to elemental sulfur on

the surface of the anode. Sulfates are not detected in the output stream of the AD-MEC system at 0.6, 0.8 and 1.2 V (<1 mg/L), while at 1.0 V minimal amounts are observed (153.75 mg/L), which points to 84 % degradability. The organic removal rate was successfully increased by AD-MEC with 0.6, 0.8 and 1.0 V external voltage, which was 66 % with the cell off. At 1.2 V, no improvement was observed - even the biodegradability decreased to 31.62 %. Sulfate removal was also improved with integrated MEC compared to AD-only process, where it was only 46.90 %. Therefore, it can be concluded that in terms of biodegradability there is not significant difference between the applied low voltages- 0.6 and 0.8 V, while at higher - 1.0 and 1.2 V, there is either a residue of sulfates and insufficient purification of stillage (at 1.0 V) or incomplete removal of organic matter (at 1.2 V). These results again prove the conclusions of Venkata and Lenin that the metabolism of bacteria is strongly influenced by the applied external voltage - at high voltages (in the case of 1.2 V), the microbial metabolism is inhibited and the degree of organic decomposition decreases [8].

Biogas production from ethanol stillage

Figure 2 shows a comparative graph of the kinetics of a process of biogas production in AD-MEC at different external voltages- 0.6, 0.8, 1.0 and 1.2 V. The graph shows that 27, 31, 29 and 35 liters of biogas were produced in 15 days in the AD-MEC system at 0.6, 0.8, 1.0 and 1.2 V, respectively. Although the highest yield is at 1.2 V, the fastest process is at 0.8 V- until the 10th day. Then 24 liters of biogas are produced in both and the predominance is for 1.2 V. The produced biogas for 0.6 and 1.0 V is 16 and 18 liters, respectively, on the 10th day.

Table 3. Gas composition in produced biogas by different external voltage

Gas composition	CH ₄ , vol. %	CO ₂ , vol. %	H ₂ S, ppm	H ₂ , vol. %
AD-MEC with 0.6 V	84	14	0	1
AD-MEC with 0.8 V	88	8	120	3
AD-MEC with 1.0 V	82	15	287.5	3
AD-MEC with 1.2 V	75	16	2000	7

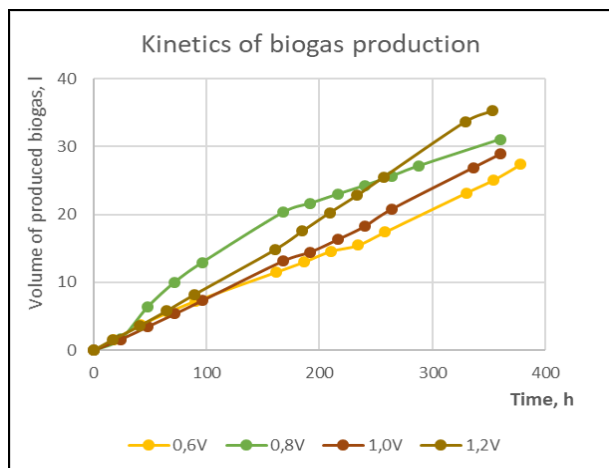


Fig. 2. Comparative graph of the kinetics of a process of biogas production at different external voltages in the AD-MEC system.

Table 3 shows the gas composition in the produced biogas at different external voltages. As can be seen, methane yields are highest at 0.8 V (88 vol. %), followed by 0.6 (84 vol. %), 1.0 (82 vol. %) and 1.2 V (75 vol. %). Generation of hydrogen (7 vol. %) and methane (75 vol. %) was observed at 1.2 V, with carbon dioxide and hydrogen not being converted into additional amounts of methane. Most likely, this is due to ongoing electrolysis of water or inhibition of the metabolism of microorganisms. Choi *et al.* found that methane production increased when an external voltage of 0.5-1.0 V was applied and decreased at 1.5 V [6]. Linji *et al.* found too that 0.8 V is the optimal external voltage for energy recovery from waste activated sludge [9]. From the obtained results, which correspond to literature data from other authors, it can be concluded that the optimal external voltage applied to AD-MEC is 0.6-0.8 V.

Stillage (substrate) was not treated for H₂S by 1.2 V - there is 2000 ppm in the produced biogas. In other cases, the concentration of hydrogen sulfide in the biogas was below 300 ppm or even 0 (at 0.6 V). The contents of carbon dioxide and hydrogen decrease and the methane content increases at 0.8 V. In the cases of 0.6 and 1.0 V the carbon dioxide content is 14-15 vol. %.

Current density

A relatively constant voltage was recorded over the duration of the assay. From MEC surface area and current, the current density for 0.6 and 1.2 V external voltage was calculated. The graph with the data is shown on Fig. 3 for 15 days of operation of AD-MEC at the respective external voltage. At 0.6 V the change in voltage and current is relatively small during the process (15 days). The maximum current was 0.043 A (achieved in the first 24 h) and the minimum was 0.030 A (on the 15th day). The current density varies from 2.15 to 1.5 A/m². At 1.2 V, a drastic change in current density is observed - from 4.45 to 2.95 A/m² (current from 0.890 A on the first day to 0.590 A on the 15th day). These results confirmed the conclusions made so far about the advantages of applying lower over higher external voltage.

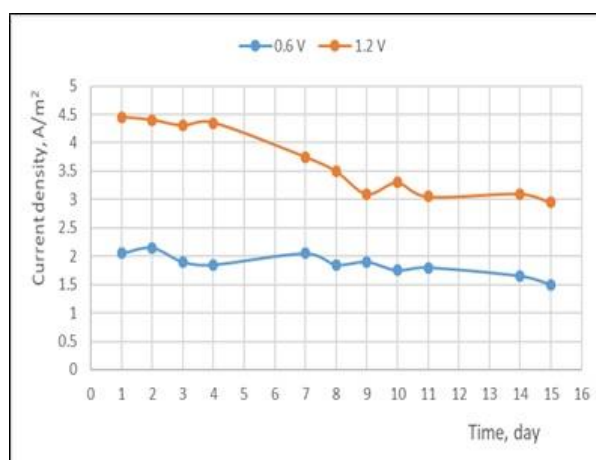


Fig. 3. Comparative graph between current density by 0.6 and 1.2V applied voltage in AD-MEC

Bacterial attachment on MEC electrodes

The SEM images on the anode surface showed more bacterial cells colonization vs cathode (Fig. 4). Electrodes were covered with attached biofilm after 15 days of biomethanation in the AD-MEC system. The formed biofilm of the electrodes was analyzed at a supply of 0.8 V external voltage, as it showed the best decomposition of organic matter and the highest yield of biomethane. Hassanein *et al.* (2020) found that the adhesion of cells to the graphite electrode was better than that on stainless steel [10]. They also proved the presence of

exoelectrogenes, electricigens and anodophilic bacteria at the anode after 11 days of the MEC inclusion to AD. Hydrogenotrophic methanogens such as *Methanobacterium*, *Methanospirillum*, *Methanobrevibacter*, *Methanosarcina*, *Methanoculleus* and *Methanocorpusculum* have been reported to grow on the anode [11]. Similar to their

results, SEM analysis showed a very well formed biofilm on the anode. Rod-shaped and coccoid bacteria dominated on the anode surface. These cells were likely exoelectrogenes and hydrogenotrophic methanogens, such as *Methanobacterium*, *Methanosarcina*, *Methanobrevibacter* and *Methanosphaera*.

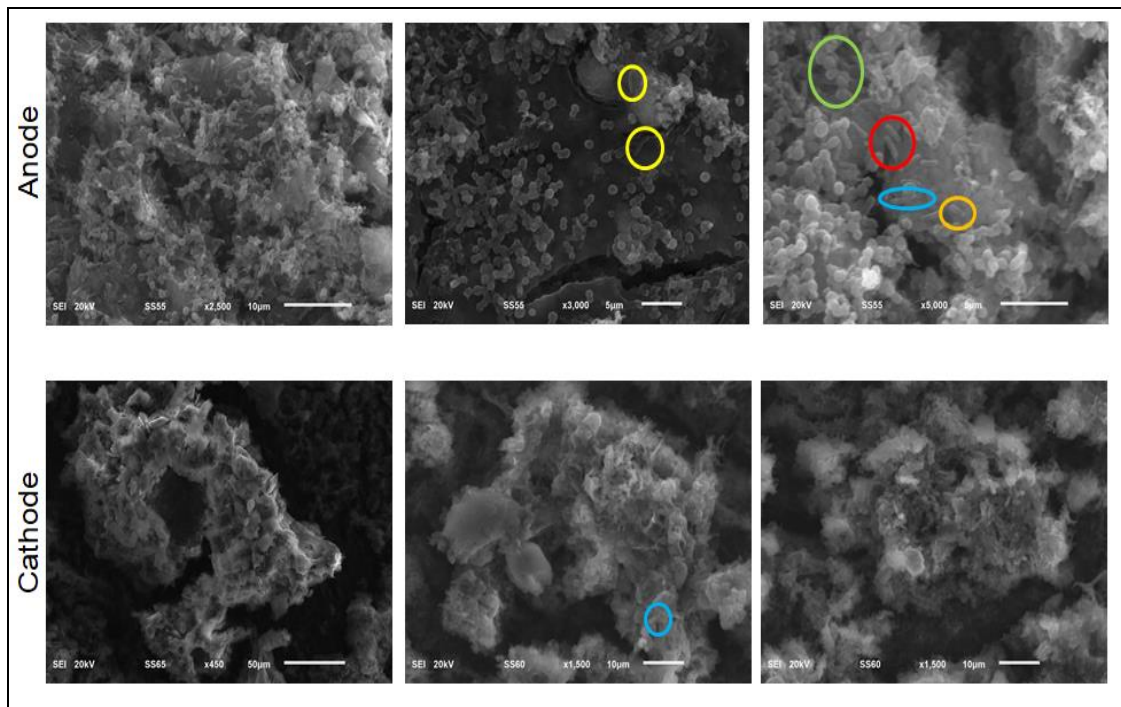


Fig. 4. Morphological characteristics of anode and cathode by SEM - coccoid bacteria with green circle, 1-1.5 μm rod-shaped bacteria with orange circle, 1.5-2.0 μm rod-shaped bacteria with blue and red circle, curved rod-shaped bacteria around 1.5 μm with yellow circle.

Less rod-shaped bacteria and no coccoid bacteria were present on the cathode, maybe because the biofilm was wrinkled a lot.

CONCLUSION

From the obtained results it could be concluded that when purifying an ethanol stillage in an AD-MEC system it is best to apply 0.8 V external voltage. Under these conditions, wastewater is purified from sulfates and organic matter (89 % biodegradability), VFAs are degraded and do not inhibit the process of methanogenesis. Also, the produced biogas has a high methane content of 88 vol. % and a low CO_2 content of 8 vol. %, which is an advantage and a prospect for eliminating the next step in the purification of biogas, and direct application. Good results for biodegradability and reduction of VFAs, as well as high methane yield

were obtained at 0.6 and 1.0 V external voltage. At higher voltages (such as 1.2 V) there was poor biodegradability (32 %), partial reduction of VFAs, which are inhibitors of methanogenesis at high values in the bioreactor, and low methane yield (75 vol. %). The current density was 2.15-1.5 A/m^2 at 0.6 V and 4.45-2.95 A/m^2 at 1.2 V. Rod-shaped and coccoid bacteria dominated in the biofilm on the anode but not on the cathode. In addition, SEM analysis distinguished bacteria that may be methanogens - rod-shaped bacteria such as *Methanobacterium*, *Methanobrevibacter* and coccoid bacteria such as *Methanosarcina*, *Methanosphaera*.

Acknowledgement: This research was supported by the Bulgarian National Science Fund, Grant № KP-06-M47/3 from 26.11.2020.

REFERENCES

1. W. Wang, J.-S. Chang, D.-J. Lee, *Bioresource Technology*, **345**, 126519 (2022).
2. R. Moreno, E. Martínez, A. Escapa, O. Martínez, R. Díez-Antolínez, X. Gomez, *Fermentation*, **4**(1), 2 (2018).
3. T. Y. Gao, H. M. Zhang, X. T. Xu, J. H. Teng, *Water Res.*, **190**, 116679 (2021).
4. C. Q. Liu, D. Z. Sun, Z. Q. Zhao, Y. Dang, D. E. Holmes, *Bioresour. Technol.*, **291**, 121877 (2019).
5. H. H. Zhou, D. F. Xing, M. Y. Xu, Y. Y. Su, Y. F. Zhang, *Appl. Energy*, **269**, 115101 (2020). DOI: 10.1016/j.apenergy.2020.115101.
6. K.-S. Choi, S. Kondaveeti, B. Min, *Bioresour. Technol.* **245**, 826 (2017).
7. A. Arvin, M. Hosseini, M. M. Amin, G. N. Darzi, Y. Ghasemi, *Biochemical Engineering Journal*, **144**, 157 (2019).
8. M. S. Venkata, B. M. Lenin, *Bioresour. Technol.*, **102**, 8457 (2011).
9. X. Linji, L. Wenzong, W. Yining, W. Aijie, L. Shuai, J. Wei, *Int. J. Hydrogen Energy*, **38** (35), 15801 (2013).
10. A. Hassanein, F. Witarsa, S. Lansing, L. Qiu, Y. Liang, *Sustainability*, **12**, 8491 (2020).
11. A. A. Pawar, A. Karthic, S. Lee, S. Pandit, S. P. Jung, *Environ. Eng. Res.*, **27**(1), 200484 (2022). <https://doi.org/10.4491/eer.2020.484>.

Comparison of the model axial graphene strain distributions in graphene/epoxy/polymethyl methacrylate (PMMA) nanocomposite under mechanical and thermomechanical loading

R. K. Vladova*, T. S. Petrova, E. G. Kirilova, A.G. Apostolov, B. Ch. Boyadjiev

*Institute of Chemical Engineering, Bulgarian Academy of Sciences,
Acad. G. Bonchev Str., Bl.103, 1113 Sofia, Bulgaria*

Received: November 07, 2022; Revised: November 25, 2022

The current report presents a theoretical study of the application of a two-dimensional stress-function method to analytically describe and compare the strains in graphene/epoxy/polymethyl methacrylate (PMMA) nanocomposite structure under three types of loading - mechanical, thermal and thermo-mechanical. Respectively, three model case solutions for all 2D strains in the nanocomposite layers at different cases of loading are developed, considered and compared with each other to illustrate the temperature influence on the strains. All results for the behavior of the axial, peel and shear strains for all three layers of the structure are illustrated in figures and discussed.

The model axial strain in the graphene layer at two different mechanical external strains - 0.3% and 0.8%, was compared and validated with experimental data at mechanical loading. The obtained results could be used for fast prediction of strain distributions in similar nanocomposite devices as sensors, nano- and optical electronic devices, energy devices, etc., at different types of external loadings.

Keywords: 2D stress-function method, strain, comparison, analytical solutions, graphene-epoxy-PMMA nanocomposite

INTRODUCTION

Research publications on the graphene-polymer nanocomposites, especially experimental ones, continuously increased exponentially both immediately - about 3000 [1] after the discovery of graphene and ten years later - about 10000 [2]. It is encouraging that in the recent years, the number of analytical and numerical approaches which have been employed to study the effect of graphene as reinforcement on the performance of polymer nanocomposites also continuously raised. Many methods and theories have been tried and approved such as molecular dynamics, continuum mechanics, atomistic simulation [3-5], multiscale modeling [6-8], etc.

In [9] the authors have reviewed the modelling of polymer nanocomposites reinforced with spherical nanoparticles or statistically isotropic aggregates. In [10] a 3D computational model of graphene-reinforced polymer composites has been developed and applied for the analysis of damage and fracture mechanisms in the composites. In [11] the interfacial stress transfer between a monolayer graphene and a commonly used PMMA matrix is studied under pristine vdW and modified H-bonding interactions by a proposed nonlinear shear-lag model. The latter considered friction beyond linear bonding, to understand evolution of interfacial stresses and further identify key interfacial parameters. In

contrast to most finite element models [12-14] considering the matrix damage or the interfacial debonding in graphene-reinforced polymer nanocomposites and requiring high computational effort, the analytical models based on shear-lag analysis are much more efficient.

Such analytical models [15, 17, 18] are very suitable for the preliminary design of bonded structures and provide reasonable results very quickly, reduce test costs and analysis time. Up to now, most of published works [19, 24-29] attended with graphene-reinforced polymer nanocomposites, are mainly experimental.

Applying the shear-lag theory, it is reported [18], that if the polymer substrate is subjected to a relatively small strain, the classical shear-lag model is valid with a linear shear stress-sliding displacement relationship and the structure is perfectly bonded. Also, in [19] on the basis of the shear-lag analysis, it is shown that an efficient reinforcement can be realized only if the size of the graphene flake is large enough (more than 30 μm). When the structure is subjected to a larger strain, a nonlinear shear-lag model has to be applied [20-23].

Despite the large number of theoretical studies on graphene-PMMA nanocomposites, there are very few works related to the behavior of the same on thermal treating. So far, the following works were found where the influence of temperature was also investigated [5, 24-28, 30, 31].

* To whom all correspondence should be sent:
E-mail: r.vladova@iche.bas.bg

No work was found about how and why temperature affects stresses or strains in a structure. Our own contribution to the subject up to date is [32], in which the foundations were laid with a derived analytical solution for the stresses in the monolayer graphene/SU-8/PMMA layers in the presence of temperature and moisture, but the results were not validated due to lack of data. Therefore, in the present work, in addition to comparison and analysis of the different solutions with and without temperature effect for the deformations, a partial validation of the model results with data from [16] was done. The data used concerned the distribution of deformations in the graphene layer at external mechanical loads of 0.3% and 0.8%, without temperature influence. Unfortunately, available data are only for elastic loading; it is known that the critical value for the external strain applied for graphene monolayer without debonding is 0.53 % [17].

Here, the theoretical study of the application of a two-dimensional stress-function method is proposed, to analytically describe and compare the strains in a graphene/epoxy/polymethyl methacrylate nanocomposite structure under three types of loading - mechanical, thermal and thermo-mechanical. Respectively, three model case solutions for all 2D strains in the nanocomposite layers at different cases of loading were developed, considered and compared with each other to illustrate the temperature influence on the strains. The model axial strain in the graphene layer at two different mechanical external strains - 0.3% and 0.8%, was compared and validated with experimental data at mechanical loading.

Model and developed analytical solutions for stresses and strains in the nanocomposite structure

Usually, the graphene flake is embedded in the polymer matrix, in this way increasing the strength and toughness of the respective nanocomposite.

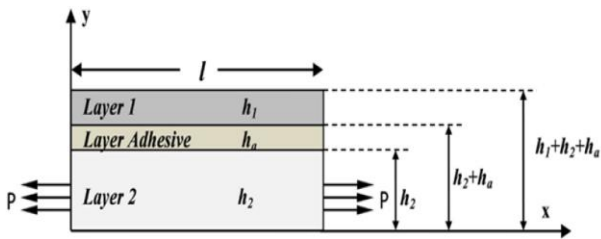


Fig. 1. Representative volume element (RVE) of graphene-(adhesive)-polymer nanocomposite structure

A representative volume element (RVE) is presented on Fig. 1. of the graphene-(adhesive)-polymer nanocomposite structure, where l - the length of the overlap zone, h_i , $(i) = 1, 2$, a are the

thicknesses of graphene, polymer and adhesive layers, P - the static tensile force.

The axial stresses in the layers are assumed to be functions of axial coordinate x only. In the adhesive interface layer, the axial stress is neglected, or $\sigma_{xx}^{(\alpha)} = 0$. All stresses in the layers (axial, normal (peel) and shear stresses) are determined under the assumption of the plane-stress formulation (standard constitutive strain-stress equations from 2D elasticity theory). The 2D stresses in the layers (axial, shear and normal) are obtained through integrating by y the differential equations of equilibrium and satisfying the boundary and contact conditions.

They are expressed in terms of a single stress potential function (axial stress of the graphene layer σ_1 and its first and second derivatives, as follows:

Layer 1:

$$\begin{aligned} \sigma_x^{(1)} &= \sigma_1, & \sigma_1' &= \frac{d\sigma_1}{dx}, & \sigma_1'' &= \frac{d^2\sigma_1}{dx^2}, \\ \sigma_y^{(1)} &= \frac{1}{2}(y - (h_1 + h_2 + h_a))^2 \sigma_1'', \\ \sigma_{xy}^{(1)} &= ((h_1 + h_2 + h_a) - y)\sigma_1' \end{aligned} \quad (1)$$

Layer adhesive:

$$\begin{aligned} \sigma_x^{(\alpha)} &\equiv 0, & \sigma_{xy}^{(\alpha)} &= h_1 \sigma_1' \\ \sigma_y^{(\alpha)} &= \left[\frac{h_1^2}{2} + h_1(h_2 + h_a - y) \right] \sigma_1'' \end{aligned} \quad (2)$$

Layer 2:

$$\begin{aligned} \sigma_x^{(2)} &= \sigma_0 - \rho \sigma_1, & \rho &= \frac{h_1}{h_2}, \\ \sigma_y^{(2)} &= \frac{-h_1}{2h_2} [y^2 - y(h_1 + h_2 + 2h_a)] \sigma_1'', \\ \sigma_{xy}^{(2)} &= \frac{h_1}{h_2} y \sigma_1' \end{aligned} \quad (3)$$

The complementary W_i and total W strain energy are obtained through integrating by y for each layer:

$$W_i = \frac{1}{2} \int_0^l \int_y \left[(\sigma_x^{(i)} \cdot \varepsilon_x^{(i)} + \sigma_y^{(i)} \cdot \varepsilon_y^{(i)} + 2\sigma_{xy}^{(i)} \cdot \varepsilon_{xy}^{(i)}) \right] dy dx \quad (4)$$

$$W = \sum_{i=1,2,\alpha} W_i \frac{1}{2} \int_0^l [D_1(\sigma_1)^2 + D_2(\sigma_1'')^2 + D_3(\sigma_1 \sigma_1'') + D_4(\sigma_1')^2 + D_5(\sigma_1) + D_6(\sigma_1') + D_7] dx = \dots = \frac{1}{2} \int_0^l \Phi(x, \sigma_1, \sigma_1', \sigma_1'') dx \quad (5)$$

The minimum of complementary strain energy functional can be found according to Euler-Lagrange equation of the variational calculus. This equation leads to the following ODE of 4th order with constant coefficients D_i :

$$2D_2 \sigma_1^{IV} + (2D_3 - 2D_4) \sigma_1'' + 2D_1 \sigma_1 + D_5 = 0 \quad (6)$$

The discriminant of the respective characteristic equation of Eq. (6) can be positive or negative, so the roots can be real or complex numbers or mixed. Additional conditions to obtain four real or complex or mixed roots for bi-quadratic characteristic equation of (6) has to be fulfilled for its coefficients (details could be found in [34]). Here, the sign of discriminant depends on coefficients D_i - Eq.(6a) or, on the thicknesses and material properties of the structure layers:

$$D_1 = \frac{h_1}{E^{(1)}} + \frac{h_2 \rho^2}{E^{(2)}} \quad (6a)$$

$$D_2 = \frac{h_1^5}{20E^{(1)}} + \frac{h_1^2 h_2}{120E^{(2)}} \left[6h_2^2 - 15h_2(y_t + h_\alpha) + 10(y_t + h_\alpha)^2 \right] + \frac{h_1^2 h_\alpha}{12E^{(2)}} [3h_1^2 + 6h_1 h_\alpha + 4h_\alpha^2]$$

$$D_3 = -\frac{\nu^{(1)} h_1^3}{3E^{(1)}} - \frac{\rho \nu^{(2)} h_1 h_2 [2h_2 - 3(y_t + h_\alpha)]}{6E^{(2)}}$$

$$D_4 = \frac{2(1+\nu^{(1)})h_1^3}{3E^{(1)}} + \frac{2(1+\nu^{(2)})h_1^2 h_2}{3E^{(2)}} + \frac{2(1+\nu^{(\alpha)})h_1^2 h_\alpha}{E^{(2)}}$$

$$D_5 = (\alpha^{(1)} - \alpha^{(2)}) \Delta T \cdot h_1 - \frac{2h_2 \rho \sigma_0}{E^{(2)}}$$

In Eq. (6a) $\alpha^{(i)}$, $i = 1, \alpha, 2$ are the coefficients of thermal expansion of the layers, ΔT is the temperature difference, and $y_t = h_1 + h_2 + h_\alpha$. The temperature T is supposed to be uniformly distributed in the layers.

The general solutions for σ_1 for real λ_i and complex roots $\pm(\alpha \pm i\beta)$ are, respectively:

$$\sigma_1 = C_1 \exp(\lambda_1 x) + C_2 \exp(\lambda_2 x) + C_3 \exp(\lambda_3 x) + C_4 \exp(\lambda_4 x) - A \quad (7)$$

$$\sigma_1 = \exp(-\alpha x) (M_1 \cos(\beta x) + M_2 \sin(\beta x)) + \exp(\alpha x) (M_3 \cos(\beta x) + M_4 \sin(\beta x)) - A \quad (8)$$

Constant $A = D_5 / 2D_1$ in the solutions depends on the value of external static load σ_0 and ΔT ; practically, it is a partial solution of the non-homogeneous Eq. (6). The coefficients M_i, C_i are integration constants in the model solution, determined from the boundary conditions. After obtaining the solution for σ_1 , all stresses in the layers (axial, normal (peel) and shear stresses) are determined as functions of σ_1 and its derivatives (see Eqs. (1) ÷ (3)).

Finally, the 2D strains in the structure layers can be obtained as:

$$\begin{aligned} \varepsilon_{xx}^{(i)} &= \frac{1}{E^{(i)}} \sigma_{xx}^{(i)} - \frac{\nu^{(i)}}{E^{(i)}} \sigma_{yy}^{(i)} + \varepsilon_{Txx}^{(i)}, \\ \varepsilon_{yy}^{(i)} &= -\frac{\nu^{(i)}}{E^{(i)}} \sigma_{xx}^{(i)} + \frac{1}{E^{(i)}} \sigma_{yy}^{(i)} + \varepsilon_{Tyy}^{(i)}, \\ \varepsilon_{xy}^{(i)} &= \frac{1 + \nu^{(i)}}{E^{(i)}} \sigma_{xy}^{(i)}, \\ \varepsilon_{Txx}^{(i)} &= \alpha_x^{(i)} \Delta T, \quad \varepsilon_{Tyy}^{(i)} = \alpha_y^{(i)} \Delta T \end{aligned} \quad (9)$$

RESULTS AND DISCUSSION

Numerical example

The structure's material and geometric properties in the numerical example are according to the data in [16] and are given in Table 1. The structure length is $l = 20 \mu\text{m}$, $\Delta T = T - T_0 = 50 \text{ K}$, starting from room temperature T_0 (RT). The applied load is 15 MPa, if not stated otherwise.

Table 1. Structure material and geometrical properties.

Geometry and physical properties	Layer 1, Graphene	Layer 2, PMMA	Layer Adhesive, SU-8
Thickness of the layer h_i , m	1.002e-09	1.5e-06 for (7)/ 30e-06 for (8)	300e-09
Young's modulus E , Pa	1e+12	3.5e+09	2e+09
Poisson's ratio ν , -	0.13	0.25	0.22
Coefficient of thermal expansion α_i (CTE), 1/K	-8e-06	74e-06	52e-06

For the model strains calculation and figures plot preparation, Mathcad Prime v.6.0 and Sigma Plot, v.13.0 were used, respectively.

From Figs. 2÷4, it can be concluded that applying a thermal loading ($\Delta T > 0$) to a mechanical one, the resultant thermomechanical strains $\varepsilon_{xx}^{(i)}, \varepsilon_{xy}^{(i)}, \varepsilon_{yy}^{(i)}$, ($i = 1, \alpha, 2$) have the same behavior like the mechanical

ones, with increasing magnitude in the same range as that of mechanical ones (cases (a±c) in Figs. 2-4).

For the axial $\varepsilon_{xx}^{(i)}$ and peel $\varepsilon_{yy}^{(i)}$ thermomechanical strains this rise in the amplitude is better visible than for the respective thermomechanical shear strains. The obtained results for the influence of temperature on the axial and peel strains are fully in agreement with recently published FEM results of Banarouei [31] for graphene/PMMA nanocomposites under temperature influence.

It should be noted that, to the best of the authors' knowledge, this [31] is the first appearance of data (experimental or model results), related to the distribution of stresses and strains in graphene as a function of temperature change.

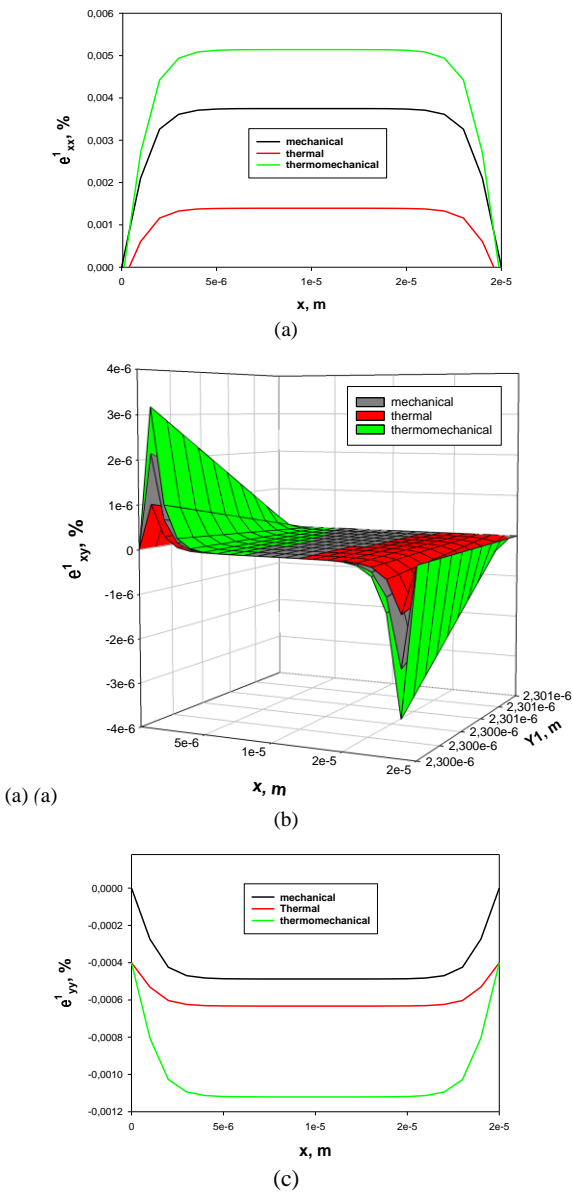


Fig. 2. Comparison of the axial strains (a), shear strains (b) and peel strains (c) in the graphene layer of the nanocomposite structure at different type of loading.

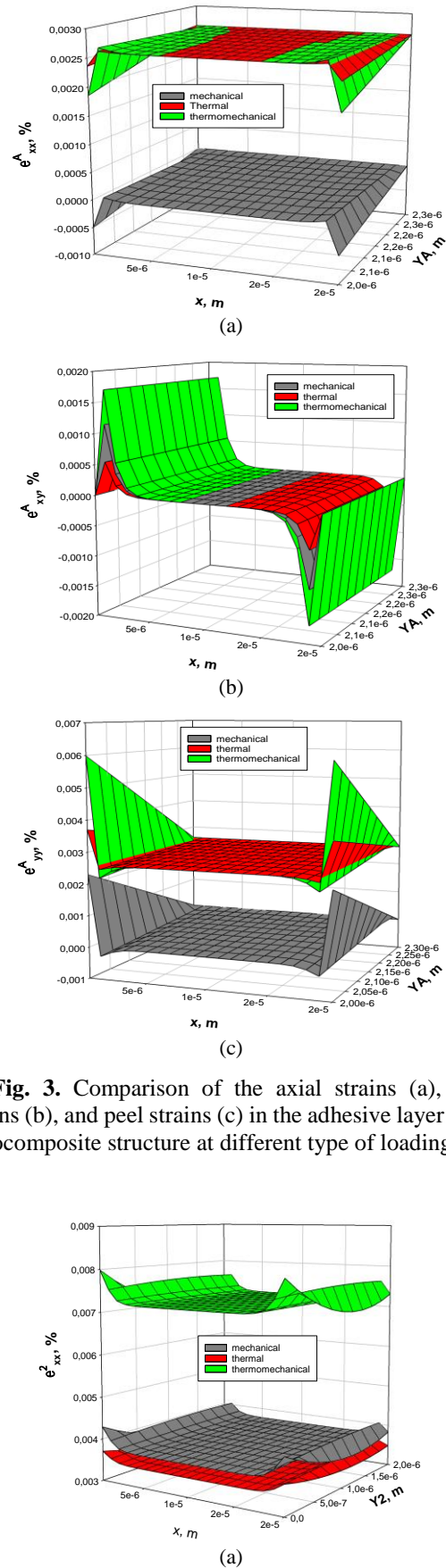


Fig. 3. Comparison of the axial strains (a), shear strains (b), and peel strains (c) in the adhesive layer of the nanocomposite structure at different type of loading.

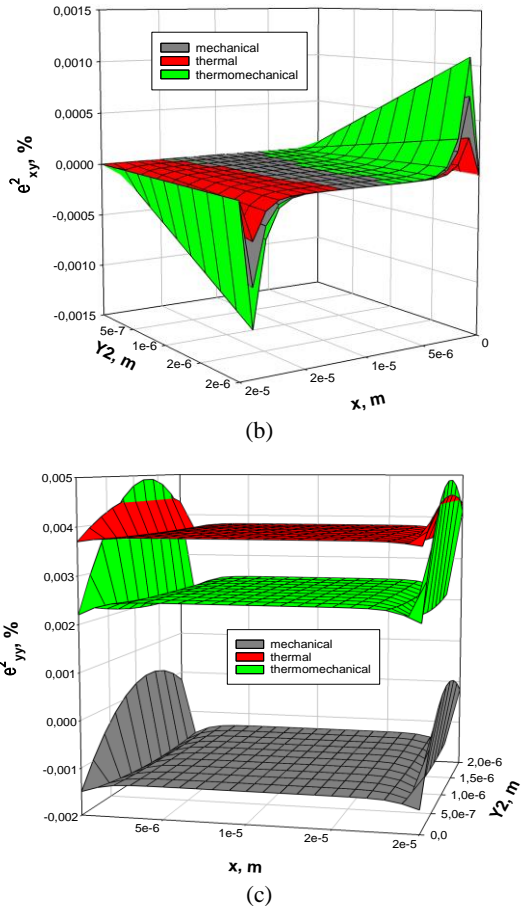


Fig. 4. Comparison of the axial strains (a), shear strains (b) and peel strains (c) in the PMMA layer of the nanocomposite.

On Figs. 5 and 6 the model axial strain in the graphene layer at two different mechanical external strains - 0.3% and 0.8%, was compared and validated with experimental data at mechanical loading from Androulidakis *et al.* [16].

The corresponding applied mechanical loads in our model for these two external strains 0.3 and 0.8 %, are 15 MPa and 1 GPa, respectively. As can be seen, our results fit well the experimental data, especially in the central part of the strain distribution along the flake length for both external strains. The mean relative errors (%) between our predictions and experimental data are 18 and 24 %, respectively, for Figs. 5 and 6; the largest deviations are due to the experimental data behavior near the flake edges, which are well visible on both figures. The proposed here model solution for strain in graphene suggests that at the ends of the flake the strain should be 0, while from experimental data distribution the opposite follows. In [33] this behavior near the graphene edges was investigated and explained as "...the distribution of axial stress (strain) along the flake deviates somewhat from the classical shear-lag prediction for a region of 1–2 μm from the edge". It

was established [33], that this behavior is mainly attributed to the presence of residual stresses, unintentional doping, and/or edge effects.

Nevertheless, the maximum values of the strain's plateau were predicted with very good accuracy as is well visible in Figs. 5 and 6. This, as well as the agreement of our predictions with the results in [31], confirm our model validity and usage for future prognosis of stresses and strains distributions in similar nanocomposite structures subjected to thermomechanical loading.

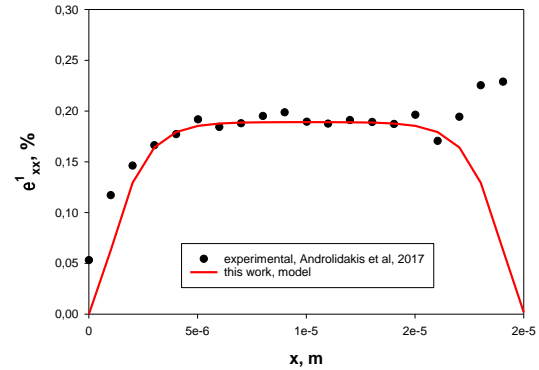


Fig. 5. Comparison of the model axial strains in the graphene layer of the nanocomposite structure at mechanical external strain 0.3% with experimental data of Androulidakis *et al.*, 2017 [16].

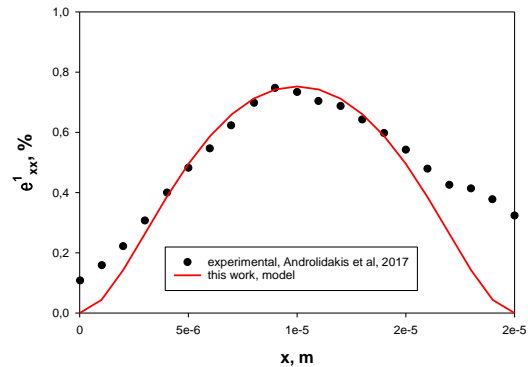


Fig. 6. Comparison of the model axial strains in the 1st layer of the nanocomposite structure at mechanical external strain 0.8 % with experimental data of Androulidakis *et al.*, 2017 [16].

CONCLUSIONS

In this study, the applicability of a two-dimensional stress-function method for describing strains in nanocomposite layered structures in the elastic region of applied loads is shown. Applying a thermal loading (heating, $\Delta T > 0$) or mixed (thermomechanical) loading, all resultant strains in the structure layers show the same behavior like mechanical ones, with slight increase in amplitude. This is better visible for axial and peel strains, as in [31]. Comparison of the model axial strains in the 1st layer of the nanocomposite structure at mechanical

external strain of 0.3% and 0.8% with the experimental data of Androulidakis *et al.* [16] shows that our results fit well most of the experimental data distribution. The experimental deviations near the flake ends may be due to the presence of residual stresses, unintentional doping, and/or edge effects [33].

Acknowledgements: The authors gratefully acknowledge the Bulgarian National Science Fund for its financial support via the contract for project KII-06-H57/3/15.11.2021.

REFERENCES

1. H. Kim, A. A. Abdala, C. W. Macosko, *Macromolecules*, **43**, 6515 (2010).
2. X. Sun, C. Huang, L. Wang, L. Liang, Y. Cheng, W. Fei, Y. Li, *Adv. Mater.*, Article 2001105 (2020).
3. K. Rege, N. R. Raravikar, D.-Y. Kim, L. S. Schadler, P. M. Ajayan, J. S. Dordick, *Nano Lett.*, **3** (6), 829 (2003).
4. R. Atif, F. Inam, *Graphene*, **5** (2), 96 (2016).
5. F. Lin, Y. Xiang, H.-S. Shen, *Composites Part B*, **111**, Article 261e269 (2017).
6. B. Mortazavi, T. Rabczuk, *Carbon*, **85**, 1 (2015).
7. P. Popova-Krumova, Chr. Boyadjiev, in: Modeling and Simulation in Chemical Engineering, Project Reports on Process Simulation, Chr. Boyadjiev (ed.), Springer Nature, Switzerland, 2022, p. 199, ISBN:978-3-030-87659-3. <https://doi.org/10.1007/978-3-030-87660-9>
8. Chr. Boyadjiev, P. Popova-Krumova, in: Progress in Chemical Science Research, O. J. R. Baena (ed.), vol. 2, BP International, Hooghly, West Bengal, India, 2022, p. 1. <https://doi.org/10.9734/bpi/pcsr/v2/1920A>
9. G. Allegra, G. Raos, M. Vacatello, *Progress in Polymer Science*, **33** (7), 683 (2008).
10. G. Dai, L. Mishnaevsky, *Computational Materials Science*, **95**, 684 (2014).
11. Z. Dai, G. Wang, L. Liu, Y. Hou, Y. Wei, Z. Zhang, *Composites Science and Technology*, **136**, 1 (2016).
12. Y. Y. Jia, Z. R. Chen, W. Y. Yan, *Composites Science and Technology*, **91**, 38 (2014).
13. F. Toth, F. G. Rammerstorfer, M. J. Cordill, F. D. Fischer, *Acta Mater.*, **61**(7), 2425 (2013).
14. A. P. Sgouros, C. Androulidakis, G. Tsoukleri, G. Kalosakas, N. Delikoukos, S. Signetti, N. M. Pugno, J. Parthenios, C. Galiotis, K. Papagelis, *ACS Appl. Mater. Interfaces*, **13**, 4473 (2021).
15. Ch. Androulidakis, E. N. Koukaras, M. G. P. Carbone, M. Hadjinicolaou, C. Galiotis, *Nanoscale*, **9**, Article 18180 (2017a).
16. Ch. Androulidakis, E.N. Koukaras, J. Rahova, K. Sampathkumar, J. Parthenios, K. Papagelis, O. Frank, C. Galiotis, *Nanoscale*, **9**, Article 26593 (2017b).
17. H. Kumar, L. Dong, V. B. Shenoy, *Scientific Reports*, **6**, Article 21516 (2016).
18. L. Gong, I. A. Kinloch, R. J. Young, I. Riaz, R. Jalil, K. S. Novoselov, *Adv. Mater.*, **22**(24), 2694 (2010).
19. R. J. Young, I. A. Kinloch, L. Gong, K. S. Novoselov, *Composites Science and Technology*, **72** (12), 1459 (2012).
20. T. Jiang, R. Huang, Y. Zhu, *Adv. Funct. Mater.*, **24**(3), 396 (2014).
21. S. Wang, Y. Chen, Y. Ma, Z. Wang, J. Zhang, *Journal of Applied Physics*, **122**, Article 074301 (2017).
22. T. Petrova, E. Kirilova, W. Becker, J. Ivanova, *IOP Conference Series: Materials Science and Engineering*, **461**(1), Article 012067 (2018).
23. E. Kirilova, T. Petrova, W. Becker, J. Ivanova, *IOP Conference Series: Materials Science and Engineering*, **461**(1), Article 012029 (2018).
24. H. Zhao, N. R. Aluru, *J. Appl. Phys.*, **108**, Article 064321 (2010).
25. M. A. N. Dewapriya, A. S. Phani, R. K. N. D. Rajapakse, *Modelling Simul. Mater. Sci. Eng.*, **21**, Article 065017 (2013).
26. M. Takamura, H. Hibino, H. Yamamoto, *Journal of Physics D: Applied Physics*, **49**, Article 285303 (2016).
27. H.-S. Shen, Y. Xiang, F. Lin, D. Hui, *Composites Part B*, **119**, Article 67e78 (2017).
28. Y. Pan, B. Yang, N. Jia, Y. Yu, X. Xu, Y. Wang, B. Wu, J. Qian, R. Xia, C. Wang, A. Sun, Y. Shi, *Polymer Testing*, **101**, Article 107237 (2021).
29. Y. Yu, J. Wang, *Ultrasonics Sonochemistry*, **73**, Article 105487 (2021).
30. K. S. Kwok, Master thesis, Johns Hopkins University, Baltimore, Maryland, USA (2017).
31. S. A. Banarouei, Master thesis, York University, Toronto, Ontario, Canada (2021).
32. T. S. Petrova, E. G. Kirilova, W. Becker, J. A. Ivanova, *ZAMM*, Article e202200266 (2022). <https://doi.org/10.1002/zamm.202200266>
33. G. Anagnostopoulos, C. Androulidakis, E. N. Koukaras, G. Tsoukleri, I. Polyzos, J. Parthenios, K. Papagelis, C. Galiotis, *ACS Appl. Mater. Interfaces*, **7**, 4216 (2015).
34. A. D. Polyenin, V. F. Zaitsev, Handbook of exact solutions for ordinary differential equations, 2nd edn., 2002, Chapman & Hall/CRC, ISBN 9781584882978, Chapter 4. <https://doi.org/10.1201/9781420035339>

AUTHOR INDEX

- Abarov P., See Abarova et al. 121
- Abarova S., Antonova B., Stoichkova K., Nakova N., Abarov P., Zasheva A., Koynova R., Tenchov B., Spectroscopic and thermodynamic characterization of the chemotherapy drug Epirubicin interaction with human serum albumin 121
- Abubakar A. L., See Umar et al. 277
- Aggelidou A., See Marovska et al. 81
- Ahmed K., See Iqbal et al. 14
- Aladjadjian A., See Slavov et al. 102
- Aliyev A. M., Safarov A. R., Ali-zadeh G. A., Aliyev F. V., Study of the kinetics and mechanism of the oxidative conversion of ethyl alcohol to acetic acid over the modified natural zeolite catalyst clinoptilolite 164
- Aliyev F. V., See Aliyev et al. 164
- Aliyu M. R., See Umar et al. 277
- Ali-zadeh G. A., See Aliyev et al. 164
- Angelov A. T., See Velichkova et al. 152, 343
- Antonova B., See Abarova et al. 121
- Apostolov A. G., See Vladova et al. 349
- Argon M., See Cakir et al. 268
- Arunodhaya N., See Umayambika et al. 126
- Aşina N., See Kavaz et al. 247
- Bchiti M., Igouzal M., El-Ghizel S., El Midaoui A., Modeling pore blocking of nanofiltration and reverse osmosis membranes during NaCl removal 199
- Beschkov V., See Ganey et al. 205
- Bogdanov J., See Sherovski et al. 303
- Boyadjiev B. Ch., See Vladova et al. 349
- Bratkova S. G., See Velichkova et al. 343
- Bryaskova R., See Philipova et al. 332
- Çakır B., Şakar D., Karahan M., Stability investigation of PAA-BSA bioconjugate and PAA-Cu²⁺-BSA ternary biocomplex at different pHs 271
- Cakir C., Orak H. H., Argon M., Caliskan H., Sabudak T., Ozturk M., Guler N., Antioxidant and antidiabetic activities of hexane extract of *Genista januensis* var. *Lydia* 268
- Caliskan H., See Cakir et al. 268
- Chalova V. I., See Georgieva et al. 74
- Dencheva-Zarkova M. J., Yankov D., Genova J. L., Tsibranska I., Flux and separation efficiency in nanofiltration with mixed solvents 141
- Denkova Z. R., Denkova-Kostova R. S., Vasileva I. N., Slavov A. M., Antimicrobial activity of plant extracts of rose by-products from the essential oil industry against saprophytic and pathogenic microorganisms 95
- Denkova Z., See Latifova et al. 49
- Denkova-Kostova R. S., See Denkova et al. 95
- Denkova-Kostova R., See Latifova et al. 49
- Dimitrov K., See Langat et al. 7
- Dincheva I. N., See Dobreva et al. 43
- Djordjevic D. M., Krstic R. P., Kodric M. G., Djordjevic S. P., Modeling of polyester fabric dyeing after proteolytic enzyme pre-treatment 115
- Djordjevic S. P., See Djordjevic et al. 115
- Dobreva A. M., Dincheva I. N., Nenov N. S., Trendafilova A. B., Chemical characterization of *Artemisia annua* L. subcritical extract 43
- Dodevska T. M., Hadzhiev D. T., Slavov A. M., Biosynthesis and potential application of silver and gold nanoparticles to the electroanalysis of hydrogen peroxide and nitrite 87
- Dogan H., See Senkal et al. 57
- Dolas H., Characterization of activated carbon produced from pistachio shell at different temperatures 219
- Drossinakis Ch., See Mehandjiev et al. 211
- El Midaoui A., See Bchiti et al. 199
- El-Ghizel S., See Bchiti et al. 199
- Eren B., Gurkan Y. Y., Possible reaction pathways of selected organophosphorus and carbamate pesticides according to the DFT calculation method 224
- Faryadi M., See Milani et al. 295
- Fidan H. N., See Senkal et al. 57
- Ganchev D., See Philipova et al. 332
- Gancheva M., Iordanova R., Mihailov L., Direct mechanochemical synthesis and characterization of SrWO₄ nanoparticles 337
- Ganey E., Beschkov V., Optimal synthesis and management of supply chains for production and utilization of biogas 205
- Geçer A., Relation of the grain size, petrophysical parameters, and Fourier transform infrared analysis of Kusuri sandstones in the Zonguldak subbasin of the West Black Sea, Turkey 235
- Genova J. L., See Dencheva-Zarkova et al. 141
- Georgieva P. I., Vasileva I. N., Parzhanova A. B., Chalova V. I., Ivanova S. D., Slavov A. M., Factors affecting the amount of biologically active substances in extracts of Bulgarian medical plants typical of Western Rhodopes 74
- Gitmiş M., See Gündoğan et al. 324
- Gluhchev G., See Mehandjiev et al. 211
- Gochev V., See Popova et al. 62
- Goranov B., See Latifova et al. 49
- Guler N., See Cakir et al. 268
- Gündoğan K., Gitmiş M., Experimental investigation of the effect of nanomaterial reinforcement on the mechanical properties of rubber structures used in crank pulleys 324
- Gurkan Y. Y., See Eren et al. 224
- Gurkan Y. Y., See Kurumoglu et al. 258
- Gurkan Y. Y., See Pandir et al. 263
- Hadzhiev D. T., See Dodevska et al. 87
- Hasanoğlu A., See Kahraman et al. 242
- Hassan S. R. B., See Wei et al. 189
- Herzog M., See Langat et al. 7
- Huether F., See Mehandjiev et al. 211
- Ibrahim M. B., Rufa'i S. A., Yaqub H. U., Suleiman U. B., Efficient palladium *n*-heterocyclic carbene catalytic system for the synthesis of cinnamic acid and derivatives in water stillage 172
- Ignatov I., See Mehandjiev et al. 211
- Igouzal M., See Bchiti et al. 199

In memoriam Prof. Dr. Natasha Vaklieva-Bancheva	5
In memoriam Prof. DSc. Christo Boyanov Boyadjiev	i
Iordanova R., See Gancheva et al.	337
Iqbal M., Panhwar A., Ahmed K., Kandhro A., Sultana R., Naz S., Mughal J., Solangi Z., Textile dyeing of cotton and wool textile material with natural dyes extracted from bluish purple grapes	14
Ivanova S. D., See Georgieva et al.	74
Jayapriya J., See Sangavi et al.	158
Kahraman Ö. Ş., Phoo M. T., Küçük İ., Hasanoğlu A., Preparation of modified polyethersulfone membranes for hemodialysis.....	242
Kandhro A., See Iqbal et al.	14
Kaneva M., See Latifova et al.	49
Karahan M., See Çakır et al.	271
Kavaz D., Aşina N., CMC/PEG blended hydrogels for tissue engineering and regenerativemedicine.....	247
Kavaz D., See Umar et al.	277
Keraita J. K., See Langat et al.	7
Khan R. A., Rashid M., Naveed M., Cantharidin: A chemical precursor for the development of novel bioinsecticides	19
Kirilova A., See Olipova et al.	253
Kirilova E. G., See Vladova et al.	349
Kirilova E., See Olipova et al.	253
Kodric M. G., See Djordjevic et al.	115
Kolev I. N., See Vasileva et al.	147
Koleva P. N., See Tsanova-Savova et al.	318
Korunoska B., See Serafimovska et al.	191
Kostov G., See Latifova et al.	49
Koynova R., See Abarova et al.	121
Krstic R. P., See Djordjevic et al.	115
Küçük İ., See Kahraman et al.	242
Kumar P. B., Srinivas S., MHD Eyring-Powell nanofluid flow in a channel with oscillatory pressure gradient: A note.....	134
Kurumoglu S., Gurkan Y. Y., Computational examination of degradation reactions ofBuprofezin.....	258
Lalov I., See Philipova et al.	332
Langat H. K. , Keraita J. K., Herzog M., Dimitrov K., Mwema F. M., Effects of weight ratio of novel <i>Calotropis Procera</i> seed fiber on PLA polymer composite	7
Latifova G., Nedyalkov P., Denkova-Kostova R., Teneva D., Goranov B., Denkova Z., Kostov G., Shopska V., Kaneva M., Lactic acid beverage based on wort and mint (<i>Menta piperita L.</i>).....	49
Maleckis A., See Olipova et al.	253
Marovska G. I., See Slavov et al.	102
Marovska G. I., Vasileva I. N., Aggelidou A., Yantcheva N. S., Slavov A. M., Physico-chemical characteristics of polysaccharides isolated from lavender by-products.....	81
Mehandjiev D., Ignatov I., Neshev N., Huether F., Gluhchev G., Drossinakis Ch., Formationof clusters in water and their distribution according to the number of water molecules	211
Mihailov L., See Gancheva et al.	337
Milani S. A., Zahakifar F., Faryadi M., Reaction stoichiometry and mechanism of tetravalent cerium liquid-liquid extraction in the Ce(IV)-H ₂ SO ₄ -Cyanex 302-kerosene system.....	295
Milanov G., See Serafimovska et al.	191
Mughal J., See Iqbal et al.	14
Mwema F. M., See Langat et al.	7
Nakova N., See Abarova et al.	121
Nandhini Devi G., See Sangavi et al.	158
Naveed M., See Khan et al.	19
Naz S., See Iqbal et al.	14
Nedelkovski D., See Serafimovska et al.	191
Nedyalkov P., See Latifova et al.	49
Nenov N. S., See Dobreva et al.	43
Neshev N., See Mehandjiev et al.	211
Olipova M., Maleckis A., Puckins A., Kirilova A., Romanovska E., Kirilova E., Spectroscopicinvestigation of new benzanthrone luminescent dyes.....	253
Orak H. H., See Cakir et al.	268
Oyegoke T., Green fuels: concepts, benefits, and studies in Nigeria.....	29
Ozturk M., See Cakir et al.	268
Pandir B., Gurkan Y. Y., Degradation reactions of Covid-19 active ingredients by molecularmodeling method	263
Paneva S. S., See Tsanova-Savova et al.	318
Panhwar A., See Iqbal et al.	14
Parzhanova A. B., See Georgieva et al.	74
Petrova T. S., See Vladova et al.	349
Philipova N., Ganchev D., Lalov I., Bryaskova R., Design, preparation and antibacterial activity of light-activated polymer coatings.....	332
Phoo M. T., See Kahraman et al.	242
Popova M. R., See Velichkova et al.	152
Popova V., Gochev V., Stoyanova A., Bulgarian contribution to the investigation of natural aromatic products: a brief retrospective review.....	62
Puckins A., See Olipova et al.	253
Rashid M., See Khan et al.	19
Renganathan S., See Umayyambika et al.	126
Ristovska N., See Sherovski et al.	303
Rizaner N., See Umar et al.	277
Romanovska E., See Olipova et al.	253
Rufa'i S. A., See Ibrahim et al.	172
Sabudak T., See Cakir et al.	268
Safarov A. R., See Aliyev et al.	164
Şakar D., See Çakır et al.	271
Sangavi G., Jayapriya J., Nandhini Devi G., A kinetic study on the effect of short-term frying cycles on the properties of cold pressed peanut oil	158
Senkal B. C., Uskutoglu T., Fidan H. N., Stankov S. S., Dogan H., Stoyanova A. S., Essential oil composition and mineral element content of <i>Salvia Aethiopsis L.</i> from Turkey.....	57
Serafimovska A., Korunoska B., Milanov G., Taseska-Gjorgjijevski M., Nedelkovski D., Polyphenol composition of wine from the variety Cabernet Sauvignon.....	191

Sherovski P., Ristovska N., Bogdanov J., Stafilov T., Optimisation and validation of a method for determination of selenium in human plasma and blood by ETAAS and its clinical application.....	303	Umar H., Kavaz D., Abubakar A. L., Aliyu M. R., Rizaner N., Synthesis of zinc oxidenanoparticles using <i>Ficus thonningii</i> aqueous extract and evaluation of its anti-oxidant and anti-microbial activities.....	277
Shopska V., See Latifova et al.	49	Uskutoglu T., See Senkal et al.	57
Slavov A. M., Aladjadjian A., Marovska G. I., Synthesis of 2,5-furandicarboxylic acid using biosynthesized silver and gold nanoparticles as catalysts.....	102	Vasileva I. N., See Denkova et al.	95
Slavov A. M., See Denkova et al.	95	Vasileva I. N., See Georgieva et al.	74
Slavov A. M., See Dodevska et al.	87	Vasileva I. N., See Marovska et al.	81
Slavov A. M., See Georgieva et al.	74	Vasileva I. V., Kolev I. N., A sulfur-based qualitative test for determining the presence of the secondary alcohol functional group of (-)-quinine and (+)-quinidine.....	147
Slavov A. M., See Marovska et al.	81	Velichkova P. G., Bratkova S. G., Angelov A. T., Influence of the applied external voltage on anaerobic digestion with integrated microbial electrolysis cell	343
Sohpal, V. K., Minimization of free energy in dye removal from an aqueous solution by a biosorbent <i>Ricinus communis</i> using response surface technology.....	310	Velichkova P.G., Popova M. R., Angelov A. T., Optimization of the operating parameters of microbial electrolysis cell assisted anaerobic digester for generating bioenergy from an ethanol.....	152
Solangi Z., See Iqbal et al.	14	Vizeva M. L., See Tsanova-Savova et al.	318
Srinivas S., See Kumar et al.	134	Vladova R. K., Petrova T. S., Kirilova E. G., Apostolov A. G., Boyadjiev B. Ch., Comparison of the model axial graphene strain distributions in graphene/epoxy/polymethyl methacrylate (PMMA) nanocomposite under mechanical and thermomechanical loading.....	349
Stafilov T., See Sherovski et al.	303	Wei N.L., Hassan S. R. B., Application of response surface methodology for the optimization of copper (II) adsorption in aqueous solution using rambutan peel powder biosorbent.....	189
Stankov S. S., See Senkal et al.	57	Yankov D., See Dencheva-Zarkova et al.	141
Stoichkova K., See Abarova et al.	121	Yantcheva N. S., See Marovska et al.	81
Stoyanova A. S., See Senkal et al.	57	Yaqub H. U., See Ibrahim et al.	172
Stoyanova A., See Popova et al.	62	Zahakifar F., See Milani et al.	295
Suleiman U. B., See Ibrahim et al.	172	Zasheva A., See Abarova et al.	121
Sultana R., See Iqbal et al.	14		
Taseska-Gjorgjijevski M., See Serafimovska et al. ...	191		
Tenchov B., See Abarova et al.	121		
Teneva D., See Latifova et al.	49		
Trendafilova A. B., See Dobreva et al.	43		
Tsanova-Savova S. P., Paneva S. S., Koleva P. N., Vizeva M. L., Polyphenols in Bulgarian medicinal fruits	318		
Tsibranska I., See Dencheva-Zarkova et al.	141		
Umairambika N., Arunodhaya N., Renganathan S., Extraction of underexploited <i>Vernonia cinerea</i> oil with comparative pretreatment techniques for conversion into biodiesel.....	126		

SUBJECT INDEX

2,5-furandicarboxylic acid	102	DPPH	74
2D stress-function method	349	drug binding	121
acetic acid	164	DSC	7
activated carbon	219	dyeing	14
adsorption	189	dyeing	115
agricultural waste	219	economic	205
anaerobic digester	152	electrochemical sensor	87
anaerobic digestion	343	electrothermal atomic absorption spectrometry	303
analytical solutions	349	emulsifiable concentrate	19
anthocyanins	291	energy	211
antibacterial activity	332	environmental criteria	205
antimicrobial	277	Epirubicin	121
antimicrobial activity	95	essential oil	57
antioxidant	277	ethanol separation	141
antioxidant activity	74, 268	ethanol stillage	152, 343
antioxidant capacity	49	ethyl alcohol	164
aromatic plants	62	extraction	14, 43, 126
<i>Artemisia annua</i> L.	43	Eyring-Powell nanofluid	134
artemisinin	43	fatty acid profiling	158
ATR-FTIR	235	<i>Ficus thonningii</i>	277
ball-to-powder weight ratio	337	flavonoids	74
Benzanthrone derivatives	253	flavonoids, total	318
biocompatible membranes	242	fluorescence spectroscopy	121, 253
biodiesel	126	fouling	199
bioenergy	152	FRAP	74
biofuels	29	fruit decoctions	318
biological activity	62	Gaussian 09	258
biomass wastes	29	Gaussian 09W	263
biorefinery	29	Gaussian distribution	211
biosorbent	189	GC-MS	158
bio-synthesis	102	<i>Genista januensis</i>	268
blood	303	Gibbs free energy and minimization	310
bluish purple grapes	14	gold nanoparticles	102
Bulgaria	62	grain size	235
Buprofezin	258	graphene-epoxy-PMMA nanocomposite	349
by-products	81	Grashof number	134
Cabernet Sauvignon	291	green chemistry	172
<i>Calotropis Procera</i>	7	green fuels	29
cantharidin	19	green synthesis	87
carbamate pesticides	224	greenhouse gases emissions	205
carbonization	219	Hartmann number	134
cerium (IV)	295	heavy metal	57
characterization	189, 277	hemodialysis	242
chemicals	43	high energy milling	337
clusters	211	human serum albumin	121
CMC	247	hydrocarbon	235
CO ₂ extraction	81	hydrogel	247
COD	343	hydrogen bonds	211
cold-pressed peanut oil	158	hydrogen peroxide	87
comparison	349	imidazolium salts	172
composites	7	insecticide	19
copper (II)	189	integrated biogas supply chain	205
cotton textile material	14	isotherms	115
Covid-19	263	kinetic model	164
Cyanex 302	295	kinetic modelling	158
DFT	224, 258, 263	kinetic studies	126, 189
differential scanning calorimetry	121	lactic acid fermentation	49
disperse dye	115	lavender	81

life cycle analysis.....	205	pretreatment.....	126
light-activated coatings.....	332	protein serine/threonine phosphatase.....	19
liquid-liquid extraction.....	295	pulsating flow.....	134
Luminescent dyes.....	253	quenching.....	121
mechanical properties.....	7	quinidine.....	147
mechanism.....	164, 295	quinine.....	147
medicinal plants.....	62, 318	reaction mechanism.....	172
metal nanoparticles.....	87	regenerative medicine.....	247
microbial electrolysis cell.....	152, 343	renewable fuels.....	29
micropore volume.....	219	reservoir sandstone.....	235
microstructure.....	7	response surface methodology.....	310
mint.....	49	reverse osmosis.....	199
mixed solvents.....	141	<i>Ricinus communis</i>	310
Mizoroki-Heck.....	172	rose species.....	95
modeling.....	115	rubber.....	324
mordant system.....	14	<i>Salvia aethiopsis</i>	57
mucic acid.....	102	secondary hydroxyl group.....	147
nanoalumina.....	324	selenium.....	303
nanofiltration.....	141, 199	silver nanoparticles.....	102
nanozeolite.....	324	social criteria.....	205
natural aromatic products.....	62	solid waste use.....	205
natural dyes.....	14	solvatochromism.....	253
nitrite.....	87	stability.....	271
noise.....	324	stoichiometry.....	295
OH radical.....	263	strain.....	349
optimal design.....	205	structural relationship activity.....	19
optimization.....	310	sulfur, elemental.....	147
organometallics.....	172	surface area.....	219
organophosphorus pesticides.....	224	synthesis.....	253
PAA-BSA bioconjugate.....	271	TEM.....	337
PAA-Cu ²⁺ -BSA ternary biocomplex.....	271	temperature.....	310
papain enzyme.....	115	tissue engineering.....	247
parameters.....	152	torsional vibration damper.....	324
PEGDMA.....	247	ultrasonication.....	126
permeate flux.....	199	UV-Vis.....	337
pesticide.....	258	valorization.....	81
petrophysical parameter.....	235	<i>Vernonia cinerea</i>	126
pharmaceutical analysis.....	147	VFA.....	343
phenolic content.....	49	vibration.....	324
phenols.....	74	vineyards.....	291
phenols, total.....	318	waste valorization.....	95
photosensitizers.....	332	water.....	211
PLA.....	7	well logs.....	235
plant-mediated synthesis.....	87	wine.....	291
plasma.....	303	wool textile material.....	14
polyester.....	115	wort.....	49
polyether sulfone.....	242	XRD.....	337
polyethylene glycol.....	242	zeolites.....	164
polyphenols.....	291, 318	zeta potential.....	271
polysaccharides.....	81	zinc oxide nanoparticles.....	277
polyvinylpyrrolidone.....	242	α -amylase.....	268
pore blocking model.....	199	α -glucosidase.....	268

Instructions about Preparation of Manuscripts

General remarks: Manuscripts are submitted in English by e-mail. The text must be typed on A4 format paper using Times New Roman font size 11, normal character spacing. The manuscript should not exceed 15 pages (about 3500 words), including photographs, tables, drawings, formulae, etc. Authors are requested to use margins of 2 cm on all sides.

Manuscripts should be subdivided into labelled sections, e.g. **Introduction, Experimental, Results and Discussion, etc.** The **title page** comprises headline, author's names and affiliations, abstract and key words. Attention is drawn to the following:

a) **The title** of the manuscript should reflect concisely the purpose and findings of the work. Abbreviations, symbols, chemical formulas, references and footnotes should be avoided. If indispensable, abbreviations and formulas should be given in parentheses immediately after the respective full form.

b) **The author's** first and middle name initials and family name in full should be given, followed by the address (or addresses) of the contributing laboratory (laboratories). **The affiliation** of the author(s) should be listed in detail by numbers (no abbreviations!). The author to whom correspondence and/or inquiries should be sent should be indicated by asterisk (*) with e-mail address.

The abstract should be self-explanatory and intelligible without any references to the text and containing not more than 250 words. It should be followed by key words (not more than six).

References should be numbered sequentially in the order, in which they are cited in the text. The numbers in the text should be enclosed in brackets [2], [5, 6], [9–12], etc., set on the text line. References are to be listed in numerical order on a separate sheet. All references are to be given in Latin letters. The names of the authors are given without inversion. Titles of journals must be abbreviated according to Chemical Abstracts and given in italics, the volume is typed in bold, the initial page is given and the year in parentheses. Attention is drawn to the following conventions: a) The names of all authors of a certain publication should be given. The use of "et al." in the list of references is not acceptable. b) Only the initials of the first and middle names should be given. In the manuscripts, the reference to author(s) of cited works should be made without giving initials, e.g. "Bush and Smith [7] pioneered...". If the reference carries the names of three or more authors it should be quoted as "Bush et al. [7]", if Bush is the first author, or as "Bush and co-workers [7]", if Bush is the senior author.

Footnotes should be reduced to a minimum. Each footnote should be typed double-spaced at the bottom of the page, on which its subject is first mentioned. **Tables** are numbered with Arabic numerals on the left-hand top. Each table should be referred to in the text. Column headings should be as short as possible but they must define units unambiguously. The units are to be separated from the preceding symbols by a comma or brackets. Note: The following format should be used when figures, equations, etc. are referred to the text (followed by the respective numbers): Fig., Eqns., Table, Scheme.

Schemes and figures. Each manuscript should contain or be accompanied by the respective illustrative material as well as by the respective figure captions in a separate file (sheet). As far as presentation of units is concerned, SI units are to be used. However, some non-SI units are also acceptable, such as °C, ml, l, etc. The author(s) name(s), the title of the manuscript, the number of drawings, photographs, diagrams, etc., should be written in black pencil on the back of the illustrative material (hard copies) in accordance with the list enclosed. Avoid using more than 6 (12 for reviews, respectively) figures in the manuscript. Since most of the illustrative materials are to be presented as 8-cm wide pictures, attention should be paid that all axis titles, numerals, legend(s) and texts are legible.

The authors are required to submit the text with a list of three individuals and their e-mail addresses that can be considered by the Editors as potential reviewers. Please, note that the reviewers should be outside the authors' own institution or organization. The Editorial Board of the journal is not obliged to accept these proposals.

The authors are asked to submit **the final text** (after the manuscript has been accepted for publication) in electronic form by e-mail. The main text, list of references, tables and figure captions should be saved in separate files (as *.rtf or *.doc) with clearly identifiable file names. It is essential that the name and version of the word-processing program and the format of the text files is clearly indicated. It is recommended that the pictures are presented in *.tif, *.jpg, *.cdr or *.bmp format.

The equations are written using “Equation Editor” and chemical reaction schemes are written using ISIS Draw or ChemDraw programme.

EXAMPLES FOR PRESENTATION OF REFERENCES

REFERENCES

1. D. S. Newsome, *Catal. Rev.–Sci. Eng.*, **21**, 275 (1980).
2. C.-H. Lin, C.-Y. Hsu, *J. Chem. Soc. Chem. Commun.*, 1479 (1992).
3. R. G. Parr, W. Yang, *Density Functional Theory of Atoms and Molecules*, Oxford Univ. Press, New York, 1989.
4. V. Ponec, G. C. Bond, *Catalysis by Metals and Alloys (Stud. Surf. Sci. Catal., vol. 95)*, Elsevier, Amsterdam, 1995.
5. G. Kadinov, S. Todorova, A. Palazov, in: *New Frontiers in Catalysis (Proc. 10th Int. Congr. Catal., Budapest, (1992), L. Gucci, F. Solymosi, P. Tetenyi (eds.), Akademiai Kiado, Budapest, 1993, Part C, p. 2817.*
6. G. L. C. Maire, F. Garin, in: *Catalysis. Science and Technology*, J. R. Anderson, M. Boudart (eds), vol. 6, SpringerVerlag, Berlin, 1984, p. 161.
7. D. Pocknell, *GB Patent 2 207 355* (1949).
8. G. Angelov, PhD Thesis, UCTM, Sofia, 2001, pp. 121-126.
- 9 JCPDS International Center for Diffraction Data, Power Diffraction File, Swarthmore, PA, 1991.
10. CA **127**, 184 762q (1998).
11. P. Hou, H. Wise, *J. Catal.*, in press.
12. M. Sinev, private communication.
13. <http://www.chemweb.com/alchem/articles/1051611477211.html>.

Texts with references which do not match these requirements will not be considered for publication!!!

CONTENTS

A. Serafimovska, B. Korunoska, G. Milanov, M. Taseska-Gjorgjievski, D. Nedelkovski, Polyphenol composition of wine from the variety Cabernet Sauvignon.....	291
S. A. Milani, F. Zahakifar, M. Faryadi, Reaction stoichiometry and mechanism of tetravalent cerium liquid-liquid extraction in the Ce(IV)-H ₂ SO ₄ -Cyanex 302 kerosene system	295
P. Sherovski, N. Ristovska, J. Bogdanov, T. Stafilov, Optimisation and validation of a method for determination of selenium in human plasma and blood by ETAAS and its clinical application.....	303
V. K. Sohpal, Minimization of free energy in dye removal from an aqueous <i>solution</i> by a biosorbent <i>Ricinus communis</i> using response surface technology.....	310
S. P. Tsanova-Savova, S. S. Paneva, P. N. Koleva, M. L. Vizeva, Polyphenols in Bulgarian medicinal fruits.....	318
K. Gündoğan, M. Gitmiş, Experimental investigation of the effect of nanomaterial reinforcement on the mechanical properties of rubber structures used in crank pulleys.....	324
N. Philipova 1, D. Ganchev 2, I. Lalov3, R. Bryaskova, Design, preparation and antibacterial activity of light-activated polymer coatings.....	332
M. Gancheva, R. Iordanova, L. Mihailov, Direct mechanochemical synthesis and characterization of SrWO ₄ nanoparticles.....	337
P. G. Velichkova, S. G. Bratkova, A. T. Angelov, Influence of the applied external voltage on anaerobic digestion with integrated microbial electrolysis cell.....	343
R. K. Vladova, T. S. Petrova, E. G. Kirilova, A. G. Apostolov, B. Ch. Boyadjiev, Comparison of the model axial graphene strain distributions in graphene/epoxy/polymethyl methacrylate (PMMA) nanocomposite under mechanical and thermomechanical loading..	349
Authors index.....	355
Subject index.....	358
INSTRUCTIONS TO AUTHORS.....	360